Universidad Complutense de Madrid
Facultad de Ciencias Físicas
Dpto. de Física Atómica, Molecular y Nuclear

SIMULATION AND IMAGE RECONSTRUCTION OF CLINICAL TOF-PET SCANNERS

PhD THESIS

By

KHALED M. A. ABUSHAB

Supervisors:

Dr. José Manuel Udías Moinelo
Dr. Joaquín López Herraiz

Madrid 2012

Give a man a fish and you feed him for a day.
Teach a man to fish and you feed him for a lifetime.

Chinese Proverb

Acknowledgement

Finally!

It is hard to believe, but you are holding my PhD thesis in your hands. The writing was a difficult mission, certainly in combination with a big family with three kids. However, as long as there are enough people around you who support you, it is possible.

Writing a thesis is perhaps a lonely occupation but a PhD is not something you do on your own. That is why I would like to express a special word of gratitude to the following people for their support and friendship I encountered during my PhD.

Firstly, I want to thank Jose Manuel Udías for accepting me as PhD student within the Nuclear Physics Group (GFN) and be my advisor. It has been a unique experience to work under his guidance. His desire to share his knowledge in both academic and other fields has been very inspiring for me. I consider myself extremely lucky to have worked with him. I am even more grateful to Joaquín López Herraiz my co-supervisor. Thanks a lot for both of you for your never ending patience, fruitful discussions and the proof-reading of this thesis. I highly appreciate your way of working; the autonomy and responsibility you gave me.

A big thankyou is also in order to Luis Mario Fraile for his helpful advises during the administrative procedures needed to submit this thesis in time. I also wish to thank all members of the GFN. It was very pleasant to work with you: Jacobo, Esther, Samuel, Esteban, Elena, Pablo, Paula, Ricardo, Armando, Vicky, Martin, Bruno, Paloma, César, Cristina, José María and Elvira.

I would like to thank my parents for their prayers and brothers, relatives and friends. Thank you for your encouragements.

Last but not least, my wife Hanaa, no words can express my gratitude. Your support and encouragements were in the end what made this PhD possible, you brought me all I needed, give me the time and love which were indispensable. Together with Loeai, Yara and Tala (Tota) you give me a lot of happiness during these challenging years. I am also happy we can finally live a normal life, all together and continue with the building of our life.

Thanks God!

Thanks to all of you!

Table of Contents

1. INTRODUCTION 1

1.1. OVERVIEW 1
1.2. GOALS OF THIS THESIS 5
1.3. THESIS OUTLINE 6

2. BACKGROUND 9

2.1. MEDICAL IMAGING 9
2.2. PRINCIPLES OF PET I (PHYSICS) 9
  2.2.1. Introduction 9
  2.2.2. Beta decay 10
  2.2.3. PET radionuclides 14
  2.2.4. Interaction of gamma rays with matter 14
2.3. PRINCIPLE OF PET II (DETECTORS) 15
  2.3.1. Scintillators 15
  2.3.2. Photomultiplier tube (PMT) 17
  2.3.3. Electronics 17
  2.3.4. Classification of detected events in PET 18
2.4. DATA ACQUISITION 21
  2.4.1. 2D and 3D mode data acquisition 22
  2.4.2. Sinogram and projection 22
  2.4.3. List mode 23
  2.4.4. The Michelogram 24
2.5. CORRECTIONS 26
  2.5.1. Attenuation 26
  2.5.2. Random Coincidences 27
  2.5.3. Normalization 28
  2.5.4. Scatter correction 28
  2.5.5. Dead time 31
2.6. PERFORMANCE EVALUATION 32
  2.6.1. Energy resolution 32
  2.6.2. Spatial resolution 32
  2.6.3. Sensitivity 33
  2.6.4. Scatter fraction (SF) 33
  2.6.5. Count rate performance (NEC) 34
2.7. MONTE CARLO SIMULATIONS 34
  2.7.1. Random numbers 36
  2.7.2. Monte Carlo packages for nuclear medicine 36
2.8. IMAGE RECONSTRUCTION ALGORITHMS IN PET 36
  2.8.1. Rebinning 37
  2.8.2. Analytical methods 39
  2.8.3. Iterative methods 41
  2.8.4. EM – ML 42
  2.8.5. Time-of-flight (TOF) 44

3. PENELOPET SIMULATIONS OF CLINICAL SCANNERS 47

3.1. MONTE CARLO SIMULATION: PENELOPET 48
  3.1.1. PeneloPET features 48
    3.1.1.1. Source code 49
    3.1.1.2. Description of input files 50
  3.1.2. PENELOPE 52
3.2. MATERIALS AND METHODS 54
  3.2.1. Geometry of the BIOGRAPH family of PET/CT scanners 54
  3.2.2. Performance evaluation of the B-TPTV PET scanner 56
  3.2.3. Sensitivity 58
  3.2.4. Scatter Fraction (SF) and Noise Equivalent Count (NEC) Rate 59

3.2.5. Spatial resolution 60
3.2.6. Time-of-flight (TOF) 61
3.2.7. Impact of Scintillator Crystal size and Energy resolution and Coincidence Time Window on Scanner performance 61
3.2.8. Impact of the Number of Detector Rings on the Scanner Performance 62
3.2.9. Uncertainty estimates 62
3.3. RESULTS AND DISCUSSION 64
3.3.1. Sensitivity 64
3.3.2. Scatter Fraction (SF) and Noise Equivalent Count (NEC) Rate 65
3.3.3. Spatial resolution 68
3.3.4. Time-of-Flight (TOF) 69
3.3.5. Impact of the characteristics of the scintillator crystal energy window and coincidence time window on the scanner performance 69
3.3.6. Simulation speed 73
3.4. SUMMARY AND CONCLUSION 74

4. IMAGE RECONSTRUCTION 77

4.1. INTRODUCTION 77
4.2. GFIRST: GPU-BASED FAST ITERATIVE RECONSTRUCTION OF FULLY 3-D PET SINOGRAMS 79
4.3. METHODS AND MATERIALS 81
4.3.1. Image quality phantom 81
4.3.2. Organization of the TOF 3D PET data 82
4.3.3. Sinograms 82
4.3.4. FBP reconstruction 84
4.3.5. Normalization 84
4.3.6. Gap filling 85
4.3.7. Attenuation correction 87
4.3.8. Resolution recovery with a PSF 89
4.3.9. Regularization with a median filter 91
4.3.10. Incorporation of TOF information in GFIRST 92
4.4. ASSESSMENT OF THE IMPACT OF TOF ON IMAGE QUALITY 93
4.5. RESULTS AND DISCUSSION 95
4.5.1. Comparison of TOF and non-TOF results 101
4.6. CONCLUSION 102

5. SUMMARY AND CONCLUSIONS 105

5.1. FINAL CONCLUSIONS 106

LIST OF FIGURES 109

LIST OF TABLES 111

APPENDICES 112

BIBLIOGRAPHY 115

RESUMEN EN CASTELLANO R1

1. Introduction

1.1. Overview

Positron Emission Tomography (PET) (Ollinger and Fessler, 1997) is a functional medical imaging technique that can be used to image biochemical or physiological processes within the body. Such images can be acquired by imaging the decay of radio-isotopes bound to molecules with known biological properties. Since it relies on isotopes undergoing positron decay, it belongs to the field of Nuclear Medicine.

Similar to many other imaging techniques, it is rapidly moving forward on many aspects: radiochemistry, instrumentation, image reconstruction, image processing and visualization, in addition to taking part in the ever more thrilling field of image coregistration such as PET/CT. The research work on which the present thesis is based is devoted to two of the developing fields referred above: instrumentation improvement and image reconstruction.

In nuclear medicine examinations, a radiopharmaceutical is administered to the patient. This radiopharmaceutical is marked with a radionuclide emitting, in the ideal case, one single photon with energy in the range 100 - 200 *keV* in SPECT, and a pure positron emitting radionuclide in PET. Positron emitting radionuclides, such as ^{11}C, ^{13}N, and ^{15}O, have been used in medicine for decades, with ^{18}F being the most used nowadays. Within these radionuclides, an ever growing number of tracer compounds are labeled so as to enable measurement of regional biology and biochemistry. The emission of a positron results in two annihilation photons of 511 *keV*. With the advent of tomographic reconstruction methods and the development of detector technologies, images generated from the detection of the two 511 *keV* photons have become commonplace. Such images allow us to follow the dynamics of the tracers in the body with high sensitivity, producing quantitative images of tracer concentration (Zanzonico, 2004; Zanzonico and Heller, 2007).

Nowadays 2-Deoxy-(^{18}F) fluoro-D-glucose (FDG) is the most common radiotracer used in PET to stage cancer and locate metastasis in many regions of the body. FDG is analogous to glucose and is taken up by living cells through the normal glucose pathway. Tumor imaging with FDG relies on the fact that malignant cells show higher metabolic rates than normal tissue and therefore take up greater amounts of FDG (Kubota, 2001; Couturier et al., 2004; Larson and Schwartz, 2006; Guhlke et al., 2007).

Because nuclear medicine imaging deals with the emission of radiation energy through photons and particles alongside with the detection of these quanta and particles in different materials, Monte Carlo (MC) simulations of radiation emission and detection are an important tool in nuclear medicine research.

PET clinical data and image processing methods are also fields of intense interest and development. In order to evaluate the performance of new reconstruction methods or quantification algorithms, it is often relied on the use of simulated data and images, since these offer control of the ground truth. Monte Carlo simulations are widely used for PET simulation since they can take into account all the processes involved in PET imaging, from the emission of the positron to the detection of the photons by the detectors. Simulation techniques have become an important and indispensable complement to a wide range of problems that could not be addressed by experimental or analytical approaches (Rogers, 2006).

Monte Carlo methods are numerical methods based on random variable sampling. This approach has been used to solve mathematical problems since 1770 and has been named “Monte Carlo” by Von Neumann (Assié et al., 2004) because of the similarity of statistical simulations to games of chance, represented by the most well known center for gambling: the Monte Carlo district in the Monaco principality. The general idea of Monte Carlo analysis is to create a model, which is as similar as practically possible to the real physical system of interest, and to create interactions within that system based on known probabilities of occurrence using, whenever suitable, random sampling of Probability Density Functions (PDFs). As the number of individual events (often called histories) increases, the statistical uncertainty in the simulation results decreases. Virtually, any complex system can in principle be modeled, if the distribution of events that occur in a system is known from experience or other means, and thus a PDF can be generated and sampled to simulate the real system.

MC simulations have been proven to be a useful tool to study imaging characteristics and parameters that cannot be measured experimentally. The design of new PET scanners is one area that benefits from extensive simulations (Heinrichs et al., 2003; Braem et al., 2004), as well as improved data analysis and image reconstruction algorithms assessment (Herraiz et al., 2006) and correction techniques (Levin, 1995), among other applications (Zaidi, 2000; Ay and Zaidi, 2006; Ortuño et al., 2006; Torres-

Espallardo et al., 2008). Simulations also help to identify bottlenecks regarding count rate, and critical factors affecting resolution, sensitivity, etc. Indeed, MC methods make it possible to estimate properties of new scanners which cannot be easily determined experimentally, as well as to assess the change in performance of PET scanners induced by modifications in scanner characteristics (Zaidi, 1999). Furthermore, they facilitate the systematic study of factors influencing image quality, and the validation of correction methodologies for effects such as scatter, attenuation and partial volume, for improved image quantification, as well as the development and testing of new image reconstruction algorithms.

Recently, the availability of powerful computers facilitated widespread use of PET simulation codes (Thompson et al., 1992; Briesmeister, 1993; Harrison et al., 1993; Baro et al., 1995; Kawrakow and Bielajew, 1998; Agostinelli et al., 2003). Based in GEANT4, GATE is widely used (Jan et al., 2004). SimSET and EIDOLON are other examples of MC codes (Zaidi et al., 1999).

PeneloPET (España et al., 2009) is a MC simulator based on PENELOPE (Salvat et al., 2008). PENELOPE is a Monte Carlo code for the simulation of the transport in matter of electrons, positrons and photons with energies from a few hundred eV to 1 GeV. It is then less generally aimed as GEANT4, but it suits well PET needs. It is fast and robust, and it is extensively used for other medical physics applications, particularly for dosimetry and radiotherapy (Sempau and Andreo, 2006; Vilches et al., 2006; Panettieri et al., 2007).

PeneloPET has been developed in the Nuclear Physics Group of UCM (España, 2009) and validated as a powerful tool for preclinical PET simulation (España et al., 2009). PeneloPET simulates PET systems based on crystal array blocks coupled to photo detectors. The user can easily define radioactive sources, detectors, shielding and other parts of the scanner. All these components are configured by means of a few plain text input files. PeneloPET simulations are ready to run in a cluster of computers. While PeneloPET has been validated and employed to simulate preclinical scanners (España et al., 2009), here we report detailed comparisons of PeneloPET simulations to real data for clinical scanners (Abushab et al., 2011, 2012).

Current clinical PET scanners include time-of-flight (TOF) capability. TOF information reduces noise and unwanted counts in the reconstructed images (Lewellen, 1998; Moses, 2003; Conti, 2011). In order to achieve a spatial resolution better than 1 *cm*, a TOF resolution of 66 *ps* would be required. While many commercial scanners still in use have a TOF resolution of the order of 1 *ns* (Moses, 2003), more modern PET/CT scanners have obtained TOF resolutions of the order of 500 *ps* (Surti et al., 2007; Jakoby et al., 2008; Bettinardi et al., 2011; Conti et al., 2011; Defrise et al., 2011; Mollet et al., 2011), and scanners under design or just introduced can lower the TOF figure down to 300 ps (Zaidi et al., 2011), which offer the opportunity of using TOF information to improve the quality of the reconstructed images (Conti et al., 2005). Indeed, employing TOF information, image background can be reduced. The capability of PeneloPET to include TOF properties of clinical scanners were also assessed (Abushab et al., 2011, 2012).

Another developing area which is within the scope of this thesis is image reconstruction. PET images map the origins of photons emitted from the patient. If the PET scanner detects these two photons within a particular interval of time, called the *coincidence window*, it will record a line of response (LOR) that connects the points where the two photons were detected. The collection of LOR data is referred to as the projection data.

There are two basic approaches to PET data reconstruction. One approach is analytic in nature and utilizes the mathematics of computed tomography that relates line integral measurements to the activity distribution in the object. These algorithms have a variety of names, including Fourier reconstruction and filtered back-projection (FBP). The second approach is to use iterative methods (i.e. Ordered Subsets Expectation Maximization (OSEM)) that model the data collection process in a PET scanner and attempt, in a series of successive iterations, to find the image that is most consistent with the measured data. FBP images are standard and require a moderate computational effort, whereas OSEM reconstructions create smoother images (Lartizien et al., 2003). The quantitative accuracy of OSEM is similar to that of FBP when the lesion is in a region of low background (Boellaard et al., 2001). In addition the 3D OSEM approach has btter resolution, which allows to resolve structures smaller than those obtained with FBP (Herranz, 2010).

However, OSEM algorithms require many iterations through all individual LORs and voxels and, therefore, involve much higher computational cost than FBP. Programmable graphics processing units (GPUs) were proposed many years ago as potential accelerators in complex scientific problems, such as accelerating the compute-intensive parts of the reconstruction: forward and backward projection (Herraiz et al., 2011). The GPU can handle large data sets in parallel, working in single instruction multiple data

(SIMD) mode. In order to optimize the quantitative use of PET in clinical practice, data and image processing methods are also a field of interest and development. The evaluation of such methods often relies as we do in this thesis on the use of simulated data and images since these offer control of the ground truth.

In the second part of this thesis, we used a 3D iterative OSEM code running on a GPU (GFIRST), developed at the Nuclear Physics Group of UCM (Herraiz et al., 2011). The main goal was to obtain a significant acceleration of the algorithm without compromising the quality of the reconstructed images. We adopted GFIRST and extended it for clinical PET reconstructions, and implemented further developments such as point spread function (PSF) based system response matrix (SRM), median filter, and TOF information. We used GFIRST and simulations to investigate the gain in image quality that can be achieved by including TOF information. Such investigations included comparison of signal noise ration (SNR), contrast, and noise.

This thesis is embedded in one of the research lines carried out at the Nuclear Physics Group of the University Complutense de Madrid, whose objectives are to design, develop and evaluate new data acquisition systems, data processing, and reconstruction algorithms for PET imaging. This thesis will make heavy use of tools developed in the Nuclear Physics Group, such as PeneloPET simulations. This thesis contains also contributions in image reconstruction of clinical PET data. We extended GFIRST, to include PSF, median filter, and TOF. We investigated the gain in image quality that can be achieved using these extensions. The investigation focused on SNR and contrast in hot lesions (spheres of less than 15 *mm* in diameter), as well as background noise in reconstructed images, both with and without TOF.

1.2. Goals of this thesis

The main objective of this thesis is to extend the capabilities of the tools developed in the Nuclear Physics Group for PET imaging, so far intended for the preclinical arena, to clinical settings, and to validate these tools against clinical measurements. More specifically, the main ingredient that has been considered in this thesis is the time of flight (TOF) capability, which has been included in the simulations, and introduced in the reconstructions. The improvement in image quality derived from the use of TOF information is assessed. For this goal the role of simulations is paramount as one can easily understand. Indeed, for the previous preclinical developments performed at GFN, abundant information from prototypes, phantom data, details of the electronics, test acquisitions were available. Nothing of this is readily accessible for clinical scanners. Thus, the quality of the reconstruction and data correction algorithms has to be assessed mostly with simulations. And to validate simulations for clinical scanners the first part of this thesis is devoted. During that work, we were lucky getting in touch and starting a collaboration with Bjoern Jakoby, scientist in charge at Siemens of the performance tests of the Biograph family of PET scanners. This is the main reason that our work was focused on Siemens Biograph PET/CT scanners.

This thesis should pave the way for the translation of the wealth of experience in PET reconstruction and data handling gained by GFN, to the clinical arena. Indeed, the main objective of this thesis should be to obtain confidence on the validity in clinical settings of the PET tools for simulation and reconstruction developed at GFN, which should allow the GFN to contribute significantly to research on clinical PET. Actually we can say that this has happened. Thanks to a large extent to the work carried out in this thesis, GFN is collaborating with the Massachusetts Medical Hospital (Boston) in a project on clinical PET imaging for respiratory diseases, it is beginning to collaborate, together with the Laboratory of Medical Imaging (LIM) of Gregrorio Marañón Hospital (Madrid), in a project to improve PET images for lung cancer evaluation at Hospital Clínico (also in Madrid). GFN is also participating in an M+VISION project together with several M+VISION fellows based at MIT (Boston) to improve data acquisition on preclinical and clinical PET scanners. Thus we are anticipating that the main goal of this thesis has been accomplished.

1.3. Thesis outline

The thesis is organized as follows:

Chapter 1 this chapter is an overview of PET and MC simulation, in addition to image reconstruction as well as the goals and outlines of the thesis.

Chapter 2 reviews the basic physical principles of PET. The physics of the PET detector is described in some detail as well as data collection and data handling. An overview of the main characteristics of the Monte Carlo method are reviewed next, followed by a short description of image reconstruction methods and Fourier rebinning concepts, and a review of time-of-flight (TOF) PET.

Chapter 3 provides a detailed overview of PeneloPET and its features and capabilities, in addition to a description of the computer resources used for this work. Moreover, the geometry of the scanners is reviewed, the procedure to evaluate the performance of the scanners (i.e. sensitivity, NEC, SF, spatial resolution and TOF), and factors influencing it are stated. Results and discussion of the validation of PeneloPET against measurements for Biograph scanners, as well as conclusion are also included in the chapter.

Chapter 4 contains a description of GFIRST as well as the implementation of PSF, median filter and TOF information into the algorithm. A description regarding the image quality NEMA phantom, normalization, gap filling and attenuation correction is included. Furthermore, it contains an assessment of methods, results, and discussion of SNR, contrast and noise.

Chapter 5 summarizes and describes the conclusions drawn from the research.

2. Background

2.1. Medical imaging

The past few years have seen the transition of PET from research domain into mainstream clinical application, particularly for oncology (Meyer et al., 2006; von Schulthess et al., 2006). The emergence of PET as a functional imaging modality for diagnosis, staging, therapy monitoring and assessment of recurrence in cancer has led to increasing demand of this imaging technology (Townsend, 2006). It is important to recognize that functional imaging modalities such as PET, in some instances, may provide earlier diagnosis and more accurate staging than conventional anatomical imaging with computed tomography (CT).

The combination of PET imaging with CT (PET/CT) allows for easy and fast co-registration of these two established modalities offering way more than the sum of the parts. PET/CT scanners provide accurate spatial localization of functional abnormalities and, conversely, functional assessment of abnormalities identified on anatomical scans.

2.2. Principles of PET I (Physics)

2.2.1. Introduction

PET (Cherry et al., 2003) is a technique used to create images that shows physiological function of certain organs. A very small amount of a labeled compound (called radiopharmaceutical or radiotracer) is introduced into the patient usually by intravenous injection and after an appropriate uptake period, the concentration of tracer in tissue is measured by the scanner. During its decay process, the radionuclide emits a positron which, after travelling a short distance (*the positron range*) (Cal-González et al., 2009), encounters an electron from the surrounding environment. The two particles "annihilate" each other resulting in the emission in opposite directions of two gamma rays of 511 *keV*. These two photons may be detected in coincidence and their line of response (LOR) can be identified (Figure 2.1). The gamma rays are registered by a detector to produce an image of the radiotracer distribution that correlates with the functional metabolism of the organ under study.

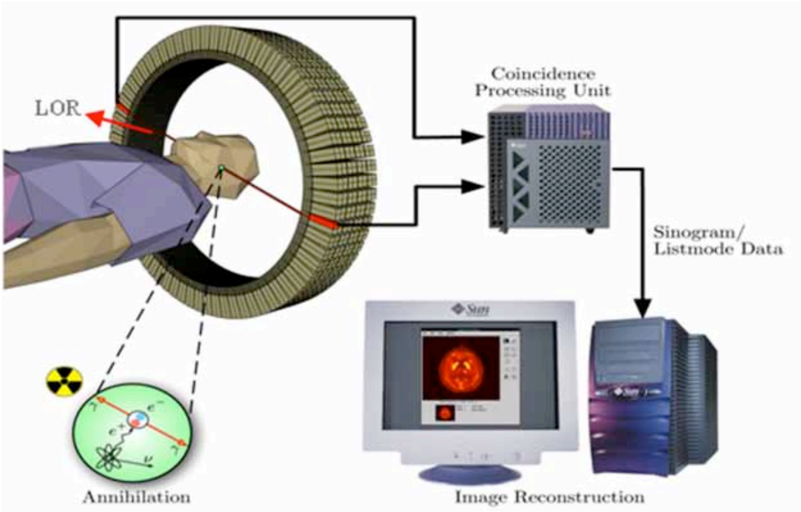

Figure 2.1. Basic principle of PET scanner and data processing (Steinbach, 2011)

2.2.2. Beta decay

One common method by which nuclei with an excess of protons may decay is through positron emission (also known as β^+ decay). Beta particles are fast electrons or positrons produced in the weak interaction decay of neutrons or protons in neutron or proton rich nuclei (Cherry et al., 2003). In a neutron-rich nucleus, a neutron can transform into a proton via the process

$$n \text{ Æ } p^+ + e^- + \bar{n}_e \tag{2.1}$$

where an electron and an antineutrino are emitted. The daughter nucleus now contains one extra proton so that its atomic number Z is increased by one. This can be written as

$$(Z + A) \text{ Æ } (Z + 1, A) + e^- + \bar{n} \tag{2.2}$$

whereas in proton-rich nuclei, a positron and neutrino are emitted in the process

$$p \text{ Æ } n + e^+ + n \tag{2.3}$$

The corresponding decay is written as

$$(Z + A) \text{ Æ } (Z - 1, A) + e^- + \bar{n} \tag{2.4}$$

The daughter nucleus now contains one proton less; therefore the atomic number is decreased by one. There is also a third process called electron capture (Krane, 1987). In this process an atomic electron close to the nucleus is captured by the nucleus

$$p + e^- \text{ Æ } n + \bar{n} \tag{2.5}$$

One of the characteristic of the b^- decay is the continous energy spectrum of the

b particles, due to energy sharing between b particles and the neutrino. Typical energy spectra are shown in Figure 2.2.

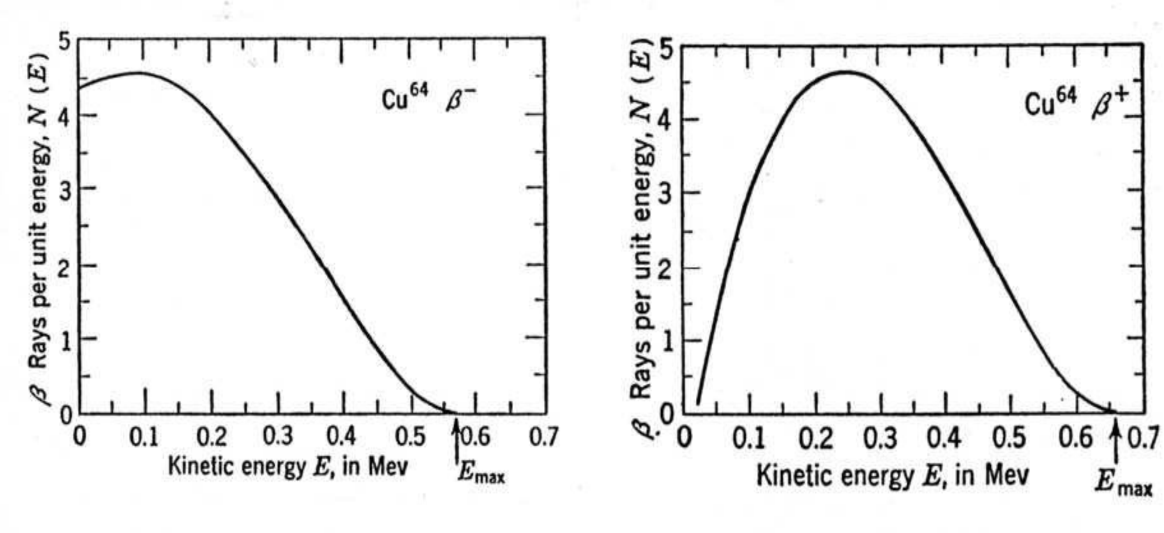

Figure 2.2. Experimental b^- spectra obtained from decaying ^{64}Cu. b^- particles are affected by the electric field of the positively charged nuclei and thus the energy spectrum is shifted towards lower energies. b^+ particles, on the other hand, are repelled by the nuclei so the energy spectrum it is shifted towards higher energies (Krane, 1987).

The positron that is ejected following b^+ decay has a very short lifetime in electron rich material such as biological tissue. It rapidly loses its kinetic energy in inelastic interactions with atomic electrons in the tissue, and once most of its energy is dissipated, it will combine with an electron. The combined mass of the two particles is almost instantly converted into energy, owing to energy-momentum conservation, in the form of two oppositely moving photons of 511 KeV of energy. This is referred to as an *annihilation reaction*.

The annihilation process forms the basis for PET imaging. A PET scanner is designed to detect and locate simultaneous annihilation photons that are emitted following decay of a radionuclide by positron emission.

The detectors are designed to see as many annihilation photons as possible and to locate the interaction point within the detector with certain spatial precission. Each detector is in electronic coincidence with other detectors so lines of response (LORs) across the object can be drawn at many different angles. Typically, 10^6 to 10^9 events (detections of annihilation photon pairs) are needed in a PET scan to reconstruct a statistically meaningful image of the distribution of radioactivity in the body (Bailey, 2005a; Townsend, 2006). A conceptualized diagram of this process is shown in Figure 2.3. There are several effects in PET imaging systems that lead to errors in determining the line along which a positron emitting radionuclide is to be found. These effects place some finite limits on the spatial resolution in PET and manifest themselves as a blurring of the reconstructed images.

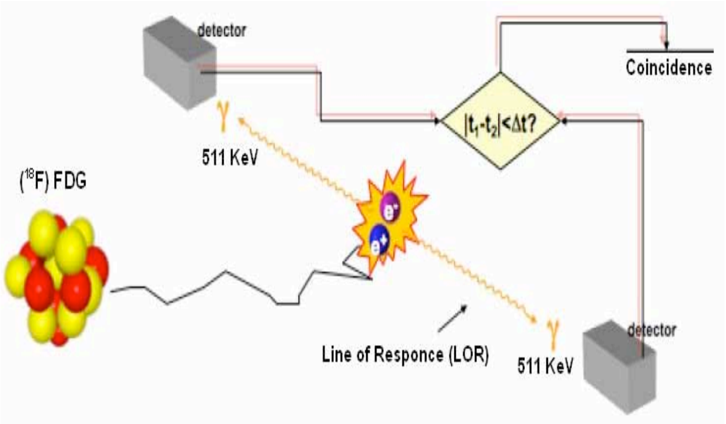

Figure 2.3. In PET, each detector generates a timed pulse when it registers an incident photon. These pulses are sent to a coincidence circuitry, and if they fall within a short time-window, they are deemed to be coincident. A coincidence event is assigned to a LOR joining the two relevant detectors

The first of these effects is *positron range*. As shown in Figure 2.4a, positron range is the distance from the site of positron emission to the site of its annihilation. This is one of the main limiting factors to the spatial resolution of PET (Levin and Hoffman, 1999). Positron range depends on both the energy of the emitted positrons and on the surrounding material. The distance in the normal direction to the location of the decaying atom to the line defined by the annihilation photons is the effective positron range or *positron range blurring*, relevant for PET projection data (see Figure 2.4a). Because positrons are emitted with a range of energy and follow a tortuous path in tissue, the positron range is a non-Gaussian distribution as described by Derenzo (Derenzo, 1979) and Levin and Hoffman (Levin and Hoffman, 1999). Recently several works study the issue of positron range (Cal-González, 2010; Cal-González et al., 2012; Larson and Schwartz, 2006; Levin and Hoffman, 1999; Palmer et al., 2005; Sánchez-Crespo and Larsson, 2006). Derenzo (Derenzo, 1986) proposed an effective method to introduce positron blurring in both forward and backward projections in FBP reconstruction. Recently, new methods to remove positron range have been developed (Cal-González et al., 2011; Fu and Qi, 2008).

The second effect comes from the fact that positron and electron are not completely at rest when they annihilate. The small net momentum of these particles means that the annihilation photons will not be at exactly 180º and will, in fact, be emitted with a distribution of angles around 180º. This is known as *non-colinearity*, and is illustrated in Figure 2.4b.

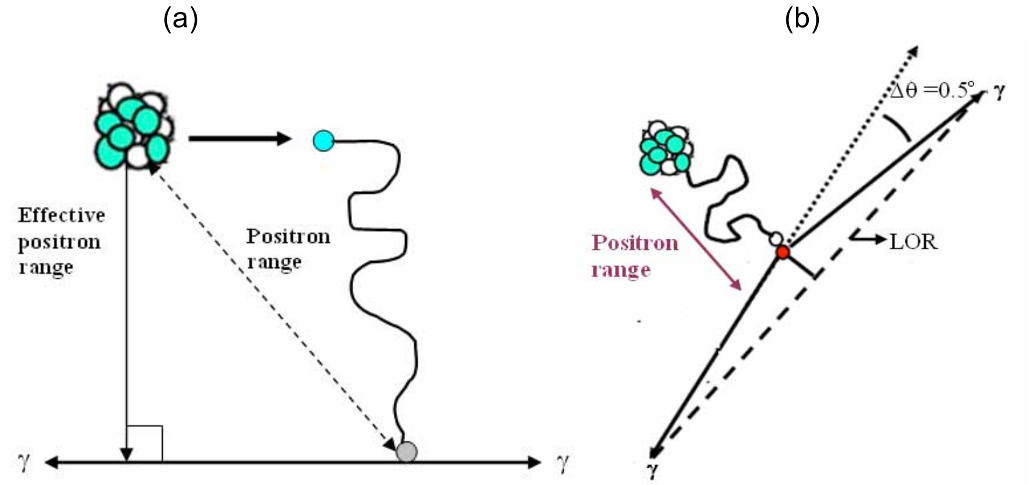

Figure 2.4. Scheme representing the definition of positron range. From its emission, the positron follows an erratic path until the annihilation process (a). Non-colinearity is independent of radionuclide, and the error introduced depends on the separation of the detectors. This is due to the fact that the annihilation does not take place exactly at rest, as the electrons are at room temperature and thus have some momentum. Thus the two annihilation photons are not emitted exactly at 180º, but with a slight deviation. Two detectors detect these photons and assign the event to a straight line, which is not the original annihilation line (b).

The exact amount of non-colinearity for annihilation γ photons traveling in water or in soft tissues is however not well established. Zanzonico (Zanzonico, 2004), refer to Berko (Berko and Hereford, 1956) and say that the deviation $\mathrm{D}q$ in Figure 2.4b, can go up to 0.5º. More recent studies exist for different metals, but not for water or most other materials relevant to PET (Damiano, 2011). Ollinger and Fessler (Ollinger and Fessler, 1997) assumed that the magnitude of the deviation is one degree or less. Humm (Humm et al., 2003) made an approximated calculation by considering just thermal motion of the particles and the Fermi moment, this would give 180º ± 0.25º. In view of the lack of solid experimental or theoretical onstrains on the non-colinearity, most PET studies assume a distribution of emitted angles roughly Gaussian in shape, with a FWHM of 0.5 (Cherry et al., 2003; Humm et al., 2003; Wernick and Aarsvold, 2004; Zanzonico, 2004) and this also done in Pene loPET.

Assuming an exact back-to-back emission the annihilation photons results in an error in locating the LOR. This error increases linearly as the diameter of the PET scanner increases (Bailey, 2005b). A study of the influence of such non-colinearity on PET image spatial resolution can be found in (Sánchez-Crespo and Larsson, 2006).

2.2.3. PET radionuclides

Some radionuclides employed in PET, ^{13}N, ^{11}C, and ^{15}O, are commonly occurring biologically relevant elements, which enable the radio-labeling of a wide variety of organic molecules. These radio-labeled molecules are chemically equivalent to their stable counter parts, and follow the same metabolic path providing valuable information about biological processes. The short half-life (1 to 20 *min*) of these radionuclides, however, requires a medical cyclotron on site.

Another approach in PET is to use analogs, modifying the original compound and to certain extent its biological role. For example, replacing one of the hydroxyl (OH) groups on the molecule of glucose with ^{18}F yields a glucose analog, fluorodeoxy-glucose (FDG), which only undergoes the first step in the metabolic pathway of glucose, becoming trapped and accumulated in the cell in proportion to glucose metabolism (Cherry et al., 2003).

2.2.4. Interaction of gamma rays with matter

The interaction of gamma rays with matter takes place mainly via the following effects:

Photoelectric absorption

The incident photon is completely absorbed by an atom and its energy ($E\gamma$) is transferred, usually to an inner shell electron (Knoll, 2000) ejecting it from the atom with energy equal to the energy of the incident gamma ray diminished by the binding energy (E_{bound}) of the electron:

$$E_{\bar{e}} = E_g - E_{bound} \tag{2.6}$$

An outer-shell electron then fills the inner-shell vacancy and the excess energy is emitted as an X-ray.

Compton scattering

In Compton scattering the incident photon transfers part of its energy to a lightly bound, outer shell electron or to a free electron, ejecting it from the atom. Upon ejection this electron is called a Compton electron. The photon is not fully absorbed but it is scattered at an angle (θ) that depends on the amount of energy transferred from the photon to the electron. The scattering angle can range from nearly 0° to 180°. Imposing conservation of momentum and energy leads to a simple relationship between the energy of the original photon ($E\gamma$), the energy of the scattered photon (E_{sc}), and the angle through which it is scattered, (θ) (Knoll, 2000).

$$E_{\mathrm{sc}} = \frac{E_\gamma}{1 - \frac{E_\gamma}{m_e c^2}(1 - \cos\theta)} \tag{2.7}$$

In this equation, m_e is the mass of the electron and c is the speed of light. Using units of electron volts for energy, the term $m_e c^2$ is equal to 511 *keV*. When the scatter angle θ 180°, maximum energy transferred occurred as:

$$E_{\bar{e},\max} = E_\gamma \left[\frac{2E_\gamma / m_e c^2}{1 + 2E_\gamma / m_e c^2} \right] \tag{2.8}$$

This gives rise to the Compton edge in the energy spectrum of mono-energetic gamma rays for finite detector size (Knoll, 2000).

Pair production

In the pair production interaction, the γ ray is converted to an electron-positron pair.

$$\gamma \rightarrow e^- + e^+ \tag{2.9}$$

This pair-production is not possible in vacuum due to momentum and energy conservation, but it is possible in matter. Energy carried by the γ photon (above 1.02 MeV) goes to kinetic energy shared by the positron and electron. The positron and electron produced will undergo interactions with material, and radiation will come from the positron when it annihilates.

2.3. Principle of PET II (Detectors)

Detection of gamma radiation is a common procedure in experimental nuclear physics. The great majority of commercial PET scanners available nowadays use scintillation crystals optically coupled to photomultiplier tubes for converting γ photons into an electrical signal. As radiation crosses the scintillator (see next section), the crystal becomes excited, causing the emission of visible light. This light is transmitted to the photomultiplier where it is converted into a current (Melcher, 2000; Wernick and Aarsvold, 2004). Such electrical signal then drives a pre-amplifier and subsequent shaping circuitry and finally enters the digital processing stages.

2.3.1. Scintillators

Scintillation detectors are widely used for gamma ray detection for most current clinical

PET scanners. These detectors consist of a dense crystalline scintillator material that serves as an interacting medium for γ rays and which emits visible light when energy is deposited in it.

In general, a scintillator should be fast, dense, have high light output and high atomic number so that a large fraction of photons undergo photoelectric absorption and, further, it must be inexpensive to produce. Some important properties of various scintillation materials are summarized in Table 2.1. Here the density of the scintillator is directly related to the stopping power of high energy photons, and therefore it is an important factor determining the necessary crystal thickness which affects the intrinsic spatial resolution of PET scanners.

Table 2.1. Properties of some scintillators used in PET detectors. Note that some of these specifications are subject to change as developers change dopants and trace elements in the scintillator growth. For example, the light output, peak wavelength, decay time and density for LYSO vary some what for different versions of the basic scintillator. Adapted from (Lewellen, 2008)

	NaI(Tl)	LSO	LYSO	GSO	BGO	$LaBr_3$
Effective atomic number (Z)	53	66	60	59	74	47
Density (g/cm3)	3.67	7.4	7.1	6.7	7.1	5.3
Attenuation coefficient (cm-1)	0.34	0.87	0.86	0.62	0.92	0.47
Refractive index	1.85	1.82	1.81	1.85	2.15	1.88
Light yield (% NaI(Tl))	100	75	80	41	2.15	160
Peak wavelength (nm)	410	420	420	430	480	370
Decay constant (ns)	230	40	41	56	300	25
Hygroscopic	Yes	No	No	No	No	No

To obtain better spatial resolution most systems use segmented scintillators that try to minimize the uncertainty in the location of the interaction. Current high resolution PET scanners employ arrays of pixilated scintillator crystals (Casey and Nutt, 1986). Scanners with blocks made of continuous crystal are less frequently used for high resolution scanners (Joung et al., 2004). Taking this into account, a high light output of the scintillator is then very desirable as it improves energy resolution and thus the identificacion of the crystals based on center of energy algorithms. For example, with BGO, block detectors with up to 16 crystals per Photomultiplier tube (PMT) can be used, but with LSO, more than 144 crystals can be coupled to a PMT (Melcher, 2000).

2.3.2. Photomultiplier tube (PMT)

A PMT is a device that produces a pulse of electrical current when stimulated by very weak light signal, such as those produced by a scintillation crystal. The PMT is made of a vacuum glass tube, which houses a photocathode, anode, and several dynodes (Knoll, 2000). Light from the scintillator is transmitted through the glass entrance window of the PMT and excites the photocathode.

The photocathode is made from a thin layer of material that can easily liberate electrons as energy is deposited in it. Each light photon from the scintillator has roughly a 15% to 25% chance (depending on wavelength and photocathode material) to liberate an electron. This probability is called the *quantum efficiency* of the PMT.

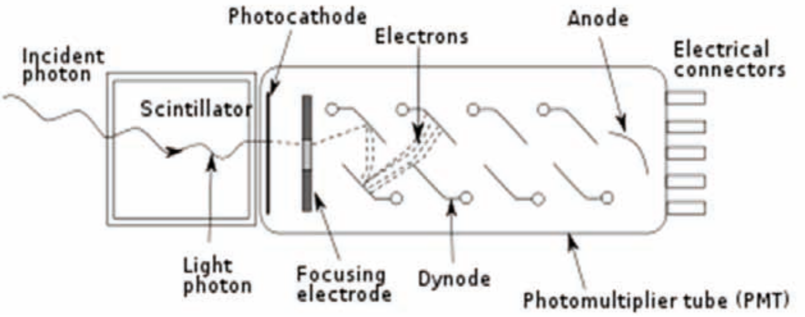

Figure 2.5. basic elements of a PMT. Adapted from (Powsner and Powsner, 2008)

A high potential difference accelerates the electron from the photocathode and directs it to strike a positively charged electrode called the first dynode. This dynode is also coated with an emissive material that readily releases electrons, and each impinging electron has acquired sufficient energy to release on the order of 3 to 4 secondary electrons from the dynode. These electrons are in turn accelerated to the second dynode and so forth, ultimately creating an avalanche of photoelectrons. After 10 stages of amplification, each initial electron has created on the order of 10^6 electrons, which, occurring over a period of a few nanoseconds, lead to an easily detectable current. Figure 2.5 skeches a PMT (Knoll, 2000). Other photodetectors are becoming common in PET, such as avalanche photodiodes and Silicon Photomultipliers (España et al., 2010; Schaart et al., 2009)

2.3.3. Electronics

Pulse processing

When a scintillation detector detects a photon, the electrical pulse generated by the PMT is used to generate a timing signal and energy/position information. Timing information is obtained, in the more classical designs, by passing the pulse through a constant fraction discriminator (CFD), which generates a digital pulse when the signal reaches a constant fraction of the peak pulse height. This pulse is then used in the coincidence circuitry (Knoll, 2000).

Usually there is a lower energy-level discriminator (LLD), and an upper energy-level discriminator (ULD) which may be used to reject pulses below or above particular values. Optimization of the LLD value is discussed in detail by (Badawi et al., 1996). The LLD can be used to discriminate against scatter, as scattered annihilation photons have lower energy than those which are not scattered.

Not all scatter can be removed this way, as many scattered photons have energy quite close to 511 *keV* and the energy resolution of typical detector systems is insufficient to distinguish them from unscattered photons. The ULD may be used to reject some events where more than one photon is incident on the block-detector at the same time. According to (Grootoonk et al., 1996; Shao et al., 1994) LLDs and ULDs have been used to divide the acquired data into different energy-windows for analysis.

The events triggered in a detector are fed into coincidence units that test whether each event is close enough in time to other events from other detectors, so that they can be considered as coincidence events (see next section). The time of flight taken by gamma photons from the positron annihilation point to the detectors is of the order of hundreds of picoseconds for clinical scanners. Scanners with time-of-flight (TOF) capability have been developed since the 80^{ts} (Allemand et al., 1980; Moszynski et al., 2006; Mullani et al., 1981).

2.3.4. Classification of detected events in PET

The detected events in PET can be grouped into five categories: true, random, scattered, single and multiple events (Figure 2.6). Among them, true, random, and scattered events are known as prompts, i.e., coincidence events.

From an ideal PET perspective, only true event are not spurious. The remaining result from undesirable physical processes. Thus, for a correct image reconstruction it is necessary to identify the true events and adopt a strategy to handle the other events, either by performing some sort of correction or simply by discarding them. In this section the origin of these events is described, while in the next section the strategies for handling them will be presented.

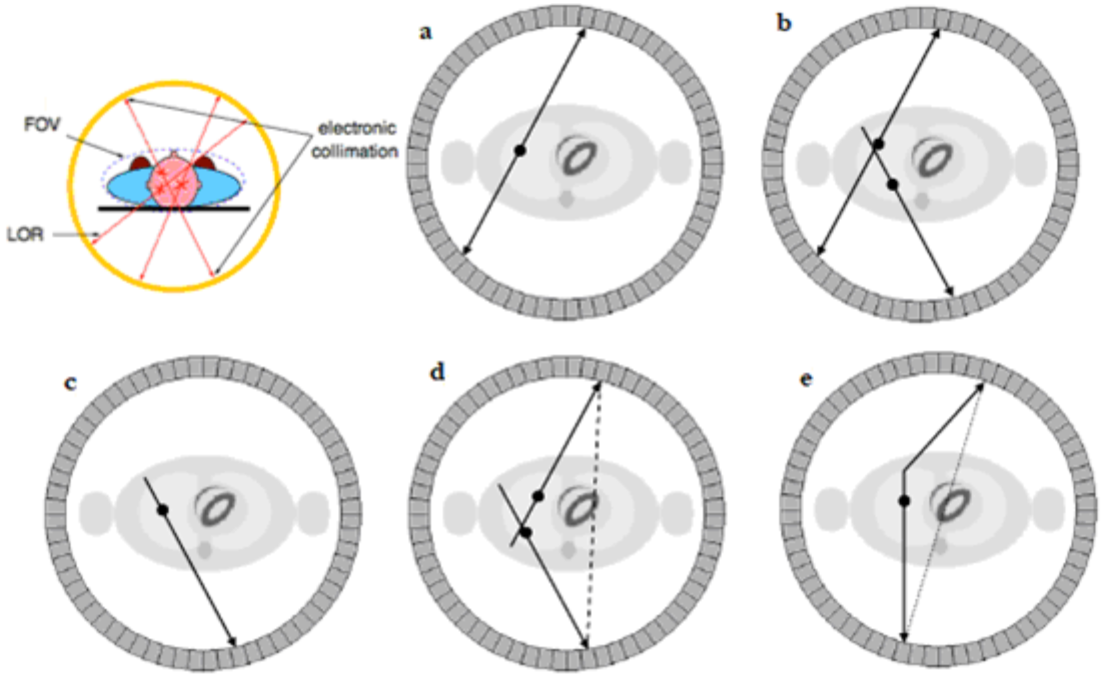

Figure. 2.6. Different types of detected events in PET: (a) true, (b) multiple, (c) single, (d) random and (e) scattered (adapted from (Cherry et al., 2003)).

A *true event* occurs when a single positron annihilates and both of the gamma rays are detected without neither of them scattering in the object being scanned. However, due to limitations of the detectors used in PET and the possible interaction of the 511 *keV* photons in the body before they reach the detector, the coincidences measured are contaminated with undesirable events which includes scattered, random (Figure 2.6a), and multiple coincidences .

Multiple events result from the detection, within the same coincidence window, of three or more gamma photons (Figure 2.6b). Since there is an ambiguity in deciding which photons make a valid pair, these events are usually discarded by the system (Bailey, 2005a).

Single event; corresponds to the detection of a single photon which is unpaired within its coincidence window (Figure 2.6c).

A *random* coincidence is the result of two positron annihilations taking place within the same coincidence window (Figure 2.6d). If the two events occur close enough in time, then the coincidence electron will register the event as a coincidence (or prompt).

Random events can be reduced either by choosing the scanner geometry so that the field of view (FOV) for single events is reduced (Badawi et al., 2000), or by reducing the time coincidence window of the scanner, up to the limit that the time resolution of the system allows, without losing good counts. Indeed the random event count rate is a function of the number of decays per second. The random count rate between two detectors, i and j, R_{ij}, is given by (Bailey, 2005a; Cooke et al., 1984; Hoffman et al., 1981):

$$R_{ij} = 2t r_i r_j \tag{2.10}$$

where r_i and r_j are the single event rates for detectors i and j, respectively, (Oliver and Rafecas, 2008) and $2t$ is the width of the coincidence timing window (Knoll, 2000). Since $r_i \approx r_j = r$ then the random event rate increases approximately proportionally to r^2. When the dead time is small, this means that the random event rate is roughly proportional to the square of the activity concentration. It is also important to note that, unlike the trues, random coincidences can arise from activity outside the FOV (Spinks et al., 1998). Thus, random coincidence count rate depends in a complicated way on both source and detector geometry (Cherry et al., 2003), and, according to Badawi (Badawi et al., 2000) is strongly dependent on both axial FOV and detector ring diameter. From Equation (2.10) it is possible to verify the following:

- The greater the total amount of activity used in a study, the higher the ratio of random-to-true coincidence rates, due to the quadratic dependence of the random coincidences.
- The random rate decreases in proportion to the width of the coincidence window.

In actual PET scanners, the random-to-true ratio ranges from about 0.1 - 0.2 for brain imaging, to more than 1 for applications where large amounts of activity exist outside the FOV (Cherry et al., 2003). One must also notice that in previous expression it is assumed that the singles to coincidences rate is much larger than one, so that the singles rate is almost mostly due to single events with no significant contribution of singles from coincidences. Otherwise, more compelx expressions have been derived (Oliver and Rafecas, 2010, 2008).

A *scattered event* occurs when one or both annihilation photons detected in coincidence have undergone a Compton interaction (Figure 2.6e). Due to the relatively poor energy resolution of most PET detectors (see section 2.6.1), there are scattered photons whose energy fits within the energy window operated by the scanner. Thus, when both photons (scattered and unscattered) are detected in coincidence, they will be treated as a prompt. If a photon suffers Compton scattering, it will be deflected from its original trajectory and will be no longer back-to-back with the other photon produced in the same annihilation. This may significantly degrade both image quality and quantitative accuracy (Wirth, 1989).

Scattered photons are so more relevant as they can be coming from outside the FOV (Ferreira et al., 1998; Sossi et al., 1995) or even due to scatter by physical parts of the scanner, such as the gantry or others. External end-shielding (Hasegawa et al., 2000) and septa between planes (Thompson, 1988) were suggested in order to screening the radiation outside the FOV and reducing the likelihood of accepting photons scattered inside the FOV.

In 3D mode the number of scattered photons is much higher than in 2D mode; the scatter fraction, the ratio of scattered events to the total recorded coincident events (Thompson, 1988) is about 10% in the latter case and 30% - 40% in 3D mode (Cherry et al., 2003). The scatter-to-true rate does not depend on the amount of activity administered, because both the scatter and the true coincidence rates increase linearly with this parameter. It also does not depend, in practice, on the width of the coincidence time window (Cherry et al., 2003). In clinical studies, the scatter-to-true coincidence ratio ranges from 0.2 to 0.5 for brain imaging and from 0.4 to 2 for abdominal imaging (Cherry et al., 2003). The scatter fraction (SF) (see section 2.6.4) was found to be strongly dependent on the detector ring diameter, but only weakly dependent on the axial FOV (Badawi et al., 2000).

2.4. Data acquisition

The end goal in PET studies is to produce an image, from which diagnostic or quantitative information can be derived. This information can be as simple as quantitative comparison of activity concentration in different tissue regions or more complex biologic parameters such as metabolic rate of gene expression. The information that is to be extracted from the image will dictate how PET data are collected (Wernick and Aarsvold, 2004).

In this section we will discuss the process of collecting data and several possibilities for performing such collection, such as 2D mode and 3D mode and list mode. We will also discuss strategies for data storage, such as sinograms and projections, and

Michelograms.

2.4.1. 2D and 3D mode data acquisition

Septal rings can be used to prevent photons coming out of the detector ring plane from reaching the detectors. This improves resolution by reducing the amount of scatter from photons originating outside the plane of one ring of crystals. The sensitivity of the scanner is reduced, however, because a significant fraction of true coincidence events are rejected. Removal of the septa will increase sensitivity and may decrease resolution if effective scatter corrections are not used. Scans obtained with the septa in place are called *two-dimensional* (2D) scans. Scan without septa is called *three-dimensional* (3D). The 3D configuration permits coincident registration of cross-plane events, those in which the two 511 *keV* photons are detected in different rings. Septa reduces also the number of random events.

An important concept behind the distinction between the 2D and 3D acquisition modes is the *transaxial plane*. A transaxial plane is a plane perpendicular to the scanner axis. So, neglecting the finite thickness of a ring, a transaxial plane can also be identified as the plane within which lies a detector ring. This means that along the direction of its axis, the scanner can be viewed as a stack of transaxial planes, each one corresponding to a detector ring.

According to the concept introduced in the former paragraph, the difference between 2D and 3D acquisitions can be stated as follows: in 2D acquisitions data are collected for LORs that are within the same transaxial plane (each ring can be treated separately). In 3D acquisition mode, in addition to transaxial planes, data are also acquired for LORs connecting detector elements in different rings: within oblique LORs, corresponding to polar angles different from zero. Thus, 3D mode contains all the information of a 2D acquisition, plus the information coming from the oblique LORs. (Bailey, 2005a; Fahey, 2002). Nowdays 2D acquisitions are sldom used in clinical PET scanners. One of the problems of 3D acquestiones is the huge size of the data collected, hence methods of reduction of the size of data collected in 3D mode are employed. These are explained in section 2.4.4.

2.4.2. Sinogram and projection

Sinograms and projections are alternate methods for storing and viewing raw PET data. Projection presents sets of parallel LORs at a specific angle ϕ (Bailey, 2005a; Defrise et al., 2005).

$$P(s,\phi) = \int_{-\infty}^{\infty} f(x,y)dy_r \tag{2.11}$$

Where $f(x,y)$ is a two-dimensional representation of the activity distribution, s is the radial coordinate, and y_r is the transversal direction coordinate.

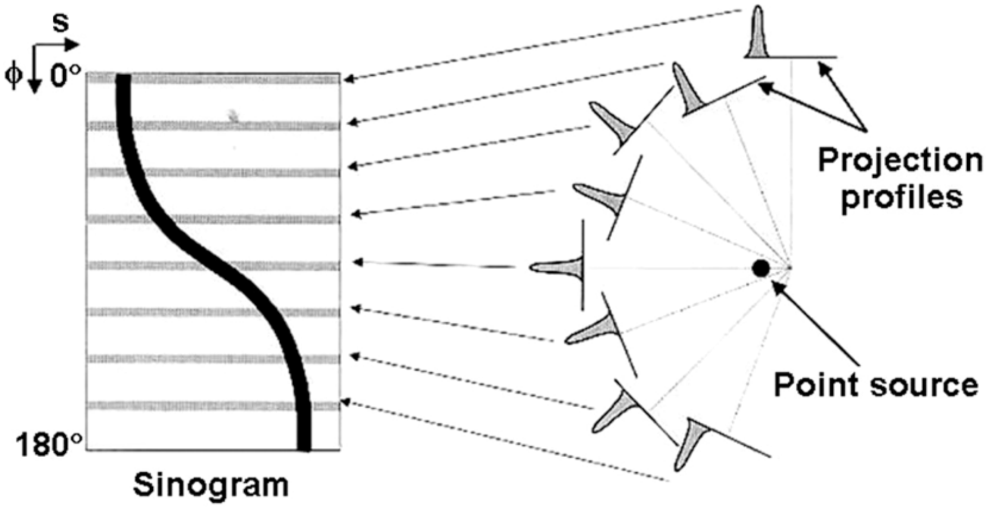

Figure 2.7. The projections of a point source at different angles (left) are represented with a sine curve in a sinogram representation of the data acquired (Bailey, 2005).

The projections from all angles can be arranged in a matrix. Because a point source will be represented by a sine curve in this matrix representation (see Figure 2.7), it is called a sinogram (Bendriem and Townsend, 1998; Defrise et al., 2005). Sinograms are the basis of many image reconstruction schemes (Bendriem and Townsend, 1998).

2.4.3. List mode

Storing information from the prompt events in order of occurrence in the acquisition system is one way to store the measured coincidences for further processing. In list mode format, each coincidence event is stored sequentially in a file containing the detection position in each detector, as well as the energy and timing information of the two photons (Bal et al., 2006). In addition, gantry information such as count rate and time information, as well as external data (e.g. gating and patient motion information) can be inserted into the list mode stream in the form of tag words (Byrne, 2001; Parra and Barrett, 1998).

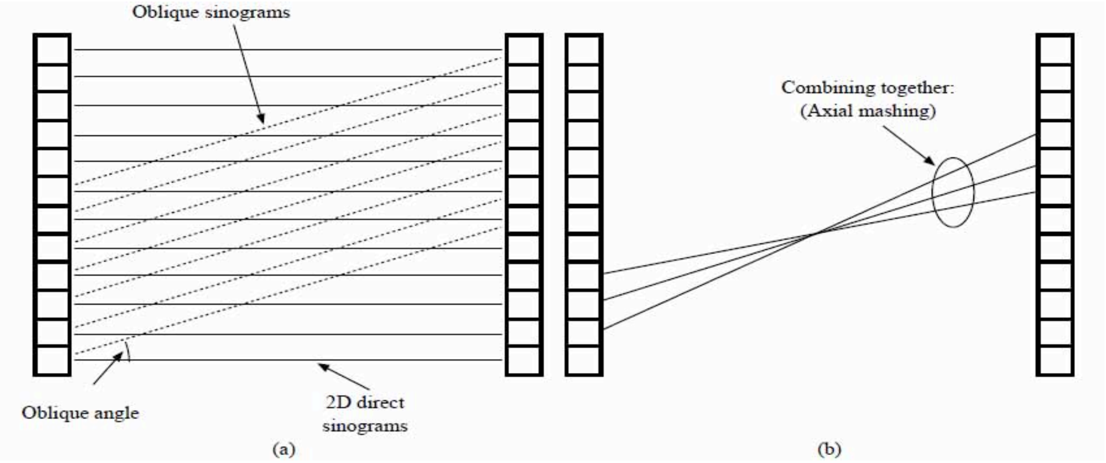

Figure 2.8. A 3D PET sinogram contains the 2D direct sinograms and all oblique sinograms (a). Axial mashing may be performed to reduce the 3D PET data size (b). The "span" parameter determines the number LORs which will be combined.

Stored event packets are processed afterwards, and transformed into sinogram datasets or LOR histograms (Kadrmas, 2004), while the timing information can be analyzed, and the data set can be split into different time frames. Figure 2.8a shows the 3D PET sinogram as a combination of 2D direct and oblique sinograms. If the scanner has n rings, information will be available for n^2 different planes and, thus, there are n^2 sinograms in the Michelogram (see next section). Therefore, 3D PET data size increases rapidly with the number of rings. To reduce the size of 3D PET data, lines of response are adjacent often combined in the axial direction as shown in Figure 2.8b.

2.4.4. The Michelogram

The Michelogram is a way of dealing with the axial sampling of PET data, devised by C. Michel (Bendriem and Townsend, 1998). The Michelogram is used to illustrate the amount of axial data combined. A Michelogram is a grid combined with two axes, each one with a number of unitary marks equal to the number of rings in the scanner (see Figure 2.9). Each point in the grid of the Michelogram corresponds to one sinogram between two rings. The first ring in one of the extremities of the scanner is ring zero, and the other rings are sequentially numbered. After michelogramming of the data, it is possible to reduce the size of the 3D mode data as mentioned above, combining several LOR adjacent in the axial direction (axial mashing) as shown in Figure 2.8b.

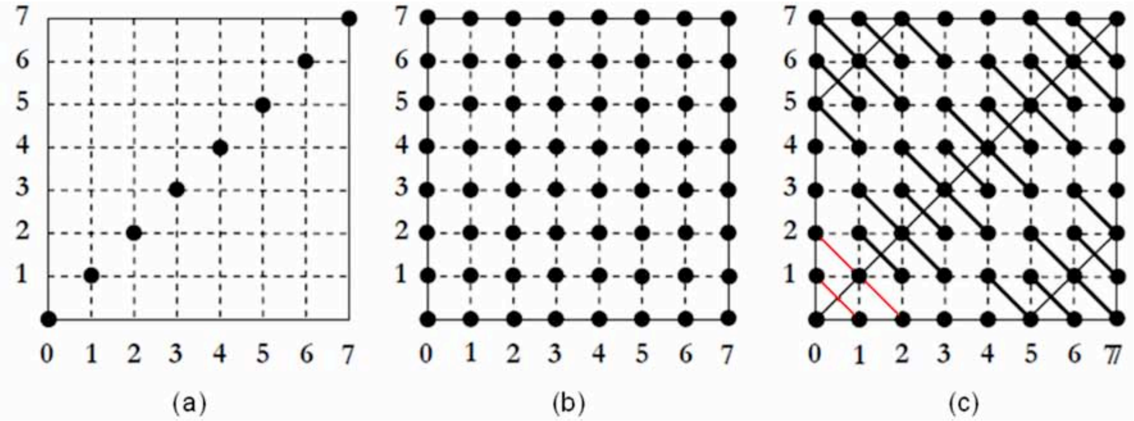

Figure 2.9. Three examples of Michelograms for a 8-ring scanner corresponding to three different acquisitions: 2D acquisition (a), 3D acquisition without mashing (b), and 3D acquisition with "mash" (c), where the span is 5 (2 + 3) and maximum ring difference (MRD) is 7 (8-1). Axial location is along the bottom left to top right diagonal direction (Defrise et al., 2005)

Figure 2.9 shows three different Michelograms corresponding to three different types of acquisitions. The Michelogram in Figure 2.9a represents a 2D acquisition; coincidences are allowed just for LORs inside each transaxial plane (each ring is exclusively in coincidence with itself), so points are along the diagonal. Figure 2.9b is for a 3D acquisition with no restrictions, i.e., any ring can be in coincidence with any other.

The acquisition represented by the Michelogram in Figure 2.9c corresponds to a 3D acquisition with *mash*, a group of planes with the same axial position and neighbouring values of ring differences mashed upon one single plane. Thick lines connecting points in the sinogram describe the mashing data that are reassigned to the points in the thin lines. Indeed, this strategy leads to bands, or *segments*, in the sinogram. The intersection of the diagonal line at the center of the segment with each of the *mashing lines* indicates the axial position of the corresponding plane upon which data have been added. If such a point of intersection is not over a grid point, the scanner axis crosses the plane not within a real ring, but in a point halfway between two adjacent rings. Whenever the mashing strategy is adopted, there is also another keyword: *span*.

The span determines the number of axial LORs which will be combined together as illustrated in Figure 2.8b. Here, the span is the sum of the numbers of combined LORs in odd and even planes, that is, 5 (2+3) in this example (points connected by red lines in Figure 2.9c). The maximum ring difference (MRD) is used in this context, which defines the maximum allowed ring difference. Data acquired between two rings, where their ring difference exceeds the MRD are discarded (Defrise et al., 2005; Fahey, 2002).

2.5. Corrections

The projection data acquired are affected by a number of factors, namely variations in detector efficiencies, photon attenuation, random coincidences, scattered coincidences, dead time, and parallax error. A large number of methodologies to correct these sources of error, their relative merits and impact on the quantitative accuracy of PET images, can be found in (Cherry et al., 2006, 2003; Wernick and Aarsvold, 2004). Among the corrections mentioned above, one of the most important ones is attenuation, which can affect both the visual quality and the quantitative accuracy of PET data (Kinahan et al., 2003). This section is devoted to the description of some corrections applied to data before image reconstruction.

2.5.1. Attenuation

Attenuation has the largest effect on the central regions of the patient. Thus, attenuation correction makes easier to find lesions that are more central in the patient. The 511 *keV* annihilation photons originating from different locations in the body are attenuated by tissue, as they traverse different thicknesses to reach the detector pair in coincidence, thus reducing the number of photons detected in each LOR. Attenuation of the signal from a given LOR can be corrected either by a direct measurement or using a mathematical model, or a combination of the two, if the material properties of the object are known (Huang et al., 1979).

In medical imaging, the attenuation coefficient reflects, essentially, the sum of the probabilities associated with the photon interacting by photoelectric absorption and Compton scattering. Since PET imaging occurs at 511 *KeV*, photon attenuation is mostly determined by Compton scattering (Kinahan et al., 2003).

The attenuation probability depends exponentially on the attenuation coefficient (μ) of the crossed material and the length travelled inside it. As both annihilation photons travel along the same line, the total length is always the same. Thus, if the length travelled by one photon is *x* and the total length is *D*, the number I of non attenuated coincidences is given by (Bailey, 2005a):

$$I = I_0 e^{-\mu x} e^{-\mu(D-x)} = I_0 e^{-\mu D} \tag{2.12}$$

If the source is positioned outside the body, the probability terms are e^0 and $e^{-\mu D}$ for the near and far detectors respectively (where D is the total thickness of the body), and the number of non attenuated coincidences is:

$$I = I_0 e^0 e^{-mD} = I_0 e^{-mD} \tag{2.13}$$

which is the same as it would be obtained from an internal source. Therefore, the problem of correcting for photon attenuation in the body is equivalent to the determination of the probability of attenuation for all sources lying along every LOR (Bailey *et al.*, 2004). By comparing the counts rate from the external (transmission) source with unattenuated count rate from the same source when the patient is not in tomograph, it is possible to determine the probability of attenuation for each LOR.

Further, in combined PET/CT systems, it is possible to use CT images of the object and proceed with a conversion method (such as segmentation or scaling), to convert the Hounsfield units into attenuation correction factors (Abella et al., 2012; Bailey, 2005a; Kinahan et al., 2003; Townsend, 2006). In this thesis, this method will be used in order to correct for attenuation.

2.5.2. Random Coincidences

As explained in section 2.3.4, random coincidences are due to the finite width of the coincidence timing window. The most evident consequence of random events on a reconstructed image is the introduction of a relatively uniform background which reduces contrast and distorts the relationship between image intensity and activity of the object.

Narrowing the coincidence timing window to avoid randoms can be part of the solution, but it must take into account the trade-off between minimizing the number of accepted randoms and the loss of true coincidences, as the time resolution of the detectors is finite. Efforts have been made to minimize random events by using faster electronics and shorter time window. Yet, in general corrections are needed to remove random counts from the acquisition and to improve image contrast.

Random count rates can be estimated from singles count rates for a given detector pair and coincidence time window in different ways (Cooke et al., 1984), one of these way was shown in Equation (2.10). In principle, the number of random events for every detector pair in the scanner may be estimated and removed. To implement this method, the data acquisition system should be able of recording not only coincidences but also the singles rate for each detector element. This is available in clinical scanners. One has to keep in mind that the correction for randoms cannot be done on an event-by-event basis, because a random event is indistinguishable from a true event for the coincidence circuit. This, in the end, increases the statistical uncertainty of the true coincidence rate (Cherry et al., 2006).

2.5.3. Normalization

PET scanners have a large number of detectors arranged in blocks and coupled to multiple PMTs (Cherry et al., 2003). Because of variations in the gain of PMTs, unaccuracies/tolerances in detector block building, physical variation of scintillator efficiency (Bailey, 2005a), etc., detection sensitivity of a detector pair varies from pair to pair, resulting in non-uniform count rates along in principle equivalent detector pairs. Information on these variations is required for the reconstruction of quantitative, artifact free, images. The method of correcting these variations is often known as *normalization* (Badawi and Marsden, 1999; Hoffman et al., 1989).

Normalization is frequently accomplished by exposing all detector pairs to a positron emitter source that generates two 511 KeV gamma-rays with a very uniform activity concentration and distribution to grant uniform exposure of all LORs. Data are collected for all detector pairs, and normalization factors are calculated for each pair by dividing the average of counts of all equivalent LORs by the individual detector pair count (Bailey, 2005a; Cherry et al., 2003; Zanzonico, 2004). This process is known as *direct normalization*. The main problem of this method is that it requires accumulation of a large number of counts in order to achieve an acceptable statistical accuracy for each LOR. This method is most often used in this thesis.

A different approach is to split normalization into different components and treat each one of them separately: this is the so-called *component-based* model for normalization. The normalization is factored into detector efficiency and spatial distortion correction, intrinsic detector efficiency, geometric factors, crystal interference, dead time factors, etc. (Badawi and Marsden, 1999). Detailed models based on this approach can be found in the following references: (Badawi and Marsden, 1999; Badawi et al., 2000; Ollinger, 1995; Townsend, 2006).

2.5.4. Scatter correction

Scatter is part of the attenuation phenomena, wherein photons deviate from their original directions and contribute to inappropriate LORs (Segars et al., 2008). This results in false counts. The goal of the scatter correction is the removal of these false counts. The removal of scatter approximates a narrow beam geometry, which is the condition assumed for the attenuation correction. Therefore, it is important that scatter correction should be performed before correcting for attenuation.

Scatter corrections are especially important since the fraction of scattered events in PET is usually very high, especially in 3D mode and it is a strong cause of contrast loss (Saha, 2010; Zaidi and Koral, 2006): for a scan of the abdomen, it can be 60% to 70% (Cherry et al., 2003).

Scatter contribution increases with density and depth of body tissue, density of detector material, activity in the patient, and energy window width of the PET system. Since both scattered and true coincidence rates vary linearly with the administered activity, the scatter-to-true ratio does not change with the activity. Also, this ratio does not change, at the lowest order, with the width of the time window. However, scattered events follow a different path towards the detector than non scattered ones and then they could be disentangled if goodtime resolution is at hand. A review by (Zaidi and Koral, 2006) provides an extensive account on the influence of scatter in patient imaging and methods to correct for it. Many different approaches have been suggested for scatter correction. These approaches can be divided into four categories shortly described in the following paragraphs**:** *multiple energy window technique or Dual Energy Window (DEW), convolution method, projection profile examination immediately outside the body and simulation method.*

Compton scattered events are recorded in a region of the energy spectrum below the photopeak; and there exists a critical energy above which only unscattered events are recorded. *DEW* (Cherry et al., 2006; Meikle and Badawi, 2005; Zaidi and Koral, 2006) use, in addition to the photopeak window (PW), an auxiliary energy window below the photopeak (LW), to directly estimate the scattered coincidences (Grootoonk et al., 1996); or above the photopeak (UW), in order to collect just unscattered events employed for “Estimation of Trues Method (ETM)” (Ferreira et al., 2002). Energy spectra showing the window setting, for both DEW and ETM are illustrated in Figure 2.10.

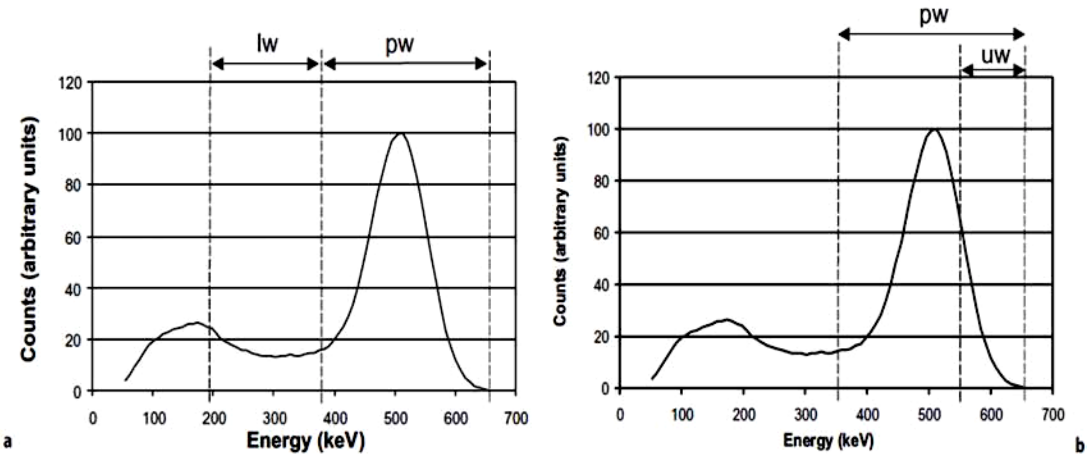

Figure 2.10. Energy spectra showing the window setting; (a) dual energy window method and (b) estimation of trues method (Meikle and Badawi, 2005).

Convolution method: A point source acquisition is used to estimate the scatter function, which is then convoluted with the source distribution to obtain an estimation of scatter data. Due to the convergence of this iterative method, the scatter estimation is improved after each iteration. The estimates of scatter events are scaled and then subtracted from the measured image data. This method is computationally efficient because of the availability of fast algorithms (Meikle and Badawi, 2005; Saha, 2010).

Projection profile examination immediately outside the body: An event detected outside the body can be related either to a random or to a scatter coincidence. After random coincidences are corrected, data from the tails (outside the object boundary) of the projection profiles are fitted to a smoothly varying function, such as a second order polynomial (Karp et al., 1990) or Gaussian (Cherry and Huang, 1995). This function then is used to estimate the scatter distribution inside the object. The method relies on the assumption that scatter is a low-frequency phenomenon and relatively insensitive to the actual radiotracer distribution. This may represent a reasonable approximation in a large variety of conditions, even for the case of a highly asymmetric source distribution (Bailey, 1998). The accuracy of the method depends on proper choice of starting points for the fitting function and the number of points used. This method has several advantages over other approaches. The fact that it does not use an auxiliary window and does not require transmission data simplifies the procedure and reduces the demand for large computer resources. Moreover, it takes into account the scatter arising from outside the detection area. Finally, the information of scatter outside the field of view can be employed to further refine more sophisticated approaches.

Simulation methods: A Monte Carlo simulation is employed to disentangle scattered and unscattered events. It uses the knowledge about the photon interaction with matter to estimate the scatter contribution. A survey of this former method and other types in this section can be found in (Meikle and Badawi, 2005; Saha, 2010).

2.5.5. Dead time

PET scanners may be regarded as a series of subsystems, each of which requires a minimum amount of time to elapse between successive events, for them to be registered as separated. Since radioactive decay is a random process, there is always a finite probability that successive events will occur within any minimum time interval, and at high count-rates, the fraction of events falling in this category can become very significant. The main effect of this phenomenon is a loss of the linear relationship between the number of coincidence events registered by the PET scanner and the total activity inside the FOV. The parameter that characterizes the counting behavior of the system at high event rates is known as dead-time (Knoll, 2000). The fractional dead-time of a system at a given count-rate is defined as the ratio of the measured count-rate and the count-rate that would have been obtained if the system behaved in a linear manner (Casey, et al., 1996).

Regarding to dead time, counting systems are usually classified as *paralyzable* or *non-paralyzable*. The paralyzable (Knoll, 2000) model describes the situation where the system is unable to process events for a fixed amount of time t after the detection of an event and if an event arrives while the system is busy due to a preceding event, the system remains dead for a further t seconds from the time of arrival of the *second* event. The relationship between the measured event rate m, the actual event rate n, and the dead time resulting from a single event is thus given by:

$$m = ne^{-nt} \tag{2.14}$$

In the non-paralyzable case, the system is also rendered dead for a time t after each event but, at difference with the previous model, while the system is dead, further events do not extend the dead perior. For such systems, the measured count rate tends asymptotically to a limiting value of t^{-1} as the actual count-rate increases, and the relationship between m, n and t is given by (Knoll, 2000):

$$m = \frac{n}{1-nt} \tag{2.15}$$

2.6. Performance evaluation

2.6.1. Energy resolution

Energy resolution can be defined as the precision with which a system can measure the energy of incident photons (Meikle and Badawi, 2005). Good energy resolution helps to exclude scattered events from the acquisition, which in turns enhances contrast and reduces background in the image. Primary causes for the degradation of the energy resolution are random statistical variations, including (Cherry et al., 2003, Knoll, 2000).

* Statistical variations in the number of scintillation light photons produced per *keV* of radiation energy deposited in the crystal;

* Statistical variations in the number of photoelectrons emitted from the photocathode;

* Statistical variations in the electron multiplication stage (dynodes) of the PMT.

Good energy resolution is necessary for a PET detector in order to achieve good image contrast and to reduce background counts (Levin et al., 2006).

In a PET system, the energy resolution can be defined by the energy resolution of the single events or the energy resolution of the coincidences (Bailey, 2005b). Measurement of energy resolution is made histograming the energy of the events acquired and plotting the number of events versus the energy measured. In scintillation detectors energy resolution is a function of the relative light output of the scintillator, as well as its intrinsic energy resolution. The intrinsic energy resolution accounts for non-statistical effects that arise in the energy measurement process. In order to achieve good image, contrast and reduced noise, a good energy resolution is necessary for a PET detector (Levin et al., 2006).

2.6.2. Spatial resolution

The spatial resolution of a PET scanner represents its ability to disentangle two close point sources (Cherry et al., 2003), and it is usually characterized by the width of the reconstructed point spread function. Spatial resolution is usually characterized by imaging a point source or a line source and measuring the corresponding full width half maximum (FWHM) of the image of these sources. Spatial resolution is usually measured along several directions, in the transaxial plane as well as along the axial direction. In the transaxial plane, radial FWHM and tangential FWHM are considered, for point sources with an offset from the scanner axis. Several factors that influence the spatial resolution in

PET are (Bailey, 2005b; Stickel and Cherry, 2005):

- Non-zero positron range.
- Non-collinearity of the annihilation photons.
- Distance between detectors.
- Width of the detectors.
- Stopping power of the scintillation detector.
- Incident angle of the photon onto the detector.
- Depth of interaction of the photon in the detector.
- Number of angular and radial sampling of the scanner.
- Reconstruction parameters.

2.6.3. Sensitivity

The sensitivity of a PET scanner quantifies the ability of a scanner to detect the coincident photons emitted from inside the FOV. It is determined mainly by four factors: the *scanner geometry*, the *detector efficiency* (stopping power for 511 *keV* photons and crystal thickness), the acquisition *energy window*, and the *dead time*. The first two factors are the main factors, and they will be investigated at length in this thesis. The *scanner geometry* establishes the total solid angle covered by the scanner over its FOV. Small diameter scanners with a large extension in the axial direction usually have higher sensitivities (Cherry et al., 2003). The *detector efficiency* is related to the probability that a photon whose trajectory intersects the detector will interact and be detected within it. This depends on detector material and thickness.

A third factor affecting the sensitivity is the acquisition *energy window*, because events falling outside this window will not be acquired (Bal et al., 2006). Finally, *dead time* (see section 2.5.5) is another source of count losses, because some of the events are rejected by the processing chain, both for dead time associated with the detection of each single photon (Bal et al., 2006; Vicente et al., 2012a, 2012b) and for coincidences. Nominal sensitivity is usually defined after a measurement at low activity and thus dead-time effects can be neglected.

2.6.4. Scatter fraction (SF)

The fraction of coincidences that have scattered (explained in section 2.3.4), and yet are acquired within the applied energy window, is known as scatter fraction (SF) (Bailey, 2005b). SF is often used to compare the performances of different PET scanners. It is given by:

$$SF = \frac{S}{R_t} \tag{2.16}$$

where S and R_t are the scatter and prompt counts rate. SF is a critical component of the noise equivalent count rate (NECR) as will be described in next section.

2.6.5. Count rate performance (NEC)

The Noise Equivalent Count Rate (NECR) (Strother et al., 1990) is an indicator of the number of useful events that the system can acquire for a given activity level. It is a performance curve suitable to compare count rate performance of different scanners or of the same scanner operating at different conditions (NEMA, 2007). As it is defined in the standard performance comparison methodology, one could say that the NECR represents the count rate which would have result in the same SNR in the image if the data would be free of scatter and random events (Bailey, 2005b). The NEC has been shown to be proportional to the square of a SNR figure (Strother et al., 1990; Surti et al., 2003; Worstell et al., 2004) where the signal refers to true events and noise to the combined statistical fluctuations from all types of events. The NEC rate has been presented in several approximately equivalent ways, for instance it is defined in (NEMA, 2007) as:

$$NEC = \frac{T^2}{T + S + R} \tag{2.17}$$

where T is the true coincidence count rate, S is the count rate of scatter coincidences and R is the count rate of random coincidences falling within the boundary of the object. The NEC has been shown to be proportional to the square of the SNR (Strother et al., 1990; Surti et al., 2003; Worstell et al., 2004) where the signal refers to the true events and the noise to the combined statistical fluctuations from all types of events.

2.7. *Monte Carlo simulations*

As we introduced before a MC simulation is a model able of simulate the behavior of the system being simulated, based on a priori knowledge of the probabilities of occurrence of the different processes or interactions involved in the measurement chain. They are a useful resort to study the interaction of radiation with matter (Agostinelli et al., 2003; Baro et al., 1995). Due to the stochastic nature of radiation emission and detection processes, the MC method is of particular interest for medical physics in areas such as radiotherapy, radiation protection and nuclear medicine (Andreo, 1991). In fact, simulation techniques constitute nowadays an essential research tool in nuclear medicine in the study of the response of imaging systems, like PET and SPECT scanners, predicting the performance of new detectors and optimizing their design (España, 2009; Zaidi, 1999).

Data obtained from MC simulations are essential in the development, validation and comparative evaluation of image reconstruction techniques and for the assessment of correction methods for photon attenuation, scattering, etc. One of the advantages of MC simulations is the possibility to change different parameters and to investigate the effects of such modifications on the performance of scanners, allowing testing several detection configurations that may be imposible or not practical in an experimental approach.

Figure 2.11 illustrates the principles and main components of MC applied to a cylindrical multi-ring PET imaging system. Some of these principles will be described in the following sections (Zaidi, 2006).

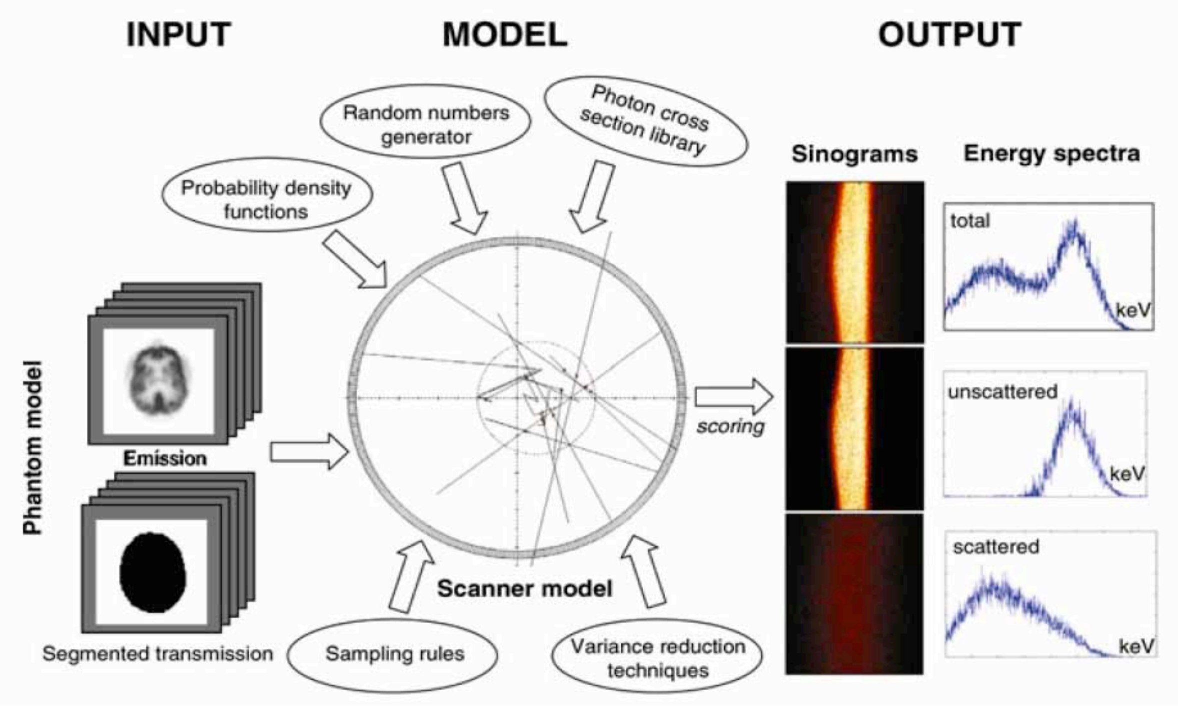

Figure 2.11. Principles and main components of a Monte Carlo program dedicated to the simulation of cylindrical multi-ring PET imaging systems. Adapted from (Zaidi, 2006)

2.7.1. Random numbers

Random numbers are of key importance when modeling a physical system using a statistical model. Every random number generator has to deliver uncorrelated, uniform and reproducible sequences with a very long period, and produce them in a short amount of time. Computer algorithms can be used to generate random numbers. An example of such an algorithm is the linear congruent algorithm where a series of random numbers I_n is calculated from a first seed value I_0, according to the relationship:

$$I_{n+1} = (aI_n + b)mod(2^k) \tag{2.18}$$

where a and b are constants and k is the integer word size of the computer (Ljungberg et al., 2012).

To obtain a stochastic variable that follows a particular PDF, several different sampling methods can be used, such as the distribution function method, the rejection method and the mixed method (Ljungberg, 1998; Zaidi, 1999).

2.7.2. Monte Carlo packages for nuclear medicine

Different MC programs have been in use in the field of nuclear imaging and internal dosimetry with many of them available as open source codes. A recent review of those can be found in (Buvat and Lazaro, 2006). There are packages that simulate the transport of radiation through matter such as: MCNP (Briesmeister, 1993), EGS4 (Kawrakow and Bielajew, 1998), PENELOPE (Salvat et al., 2008) and GEANT4 (Agostinelli et al., 2003). A number of tools for PET simulation have been developed based on these codes, such as SIMSET (Harrison et al., 2002), PETSIM (Thompson et al., 1992) or EIDOLON (Zaidi, 1999), based on MCNP, and GATE, based on GEANT4 (Jan et al., 2004). Most of them suffer from different drawbacks (handling of complex models and computing time). Further we must mention GATE, based in GEANT4, widely used (Buvat and Lazaro, 2006) in nuclear and particle physics. GATE is flexible and allows the setup of different system designs (Jan et al., 2004). However this flexibility makes the simulations very time consuming. Later in this work we will describe more in detail PeneloPET (España et al., 2009), a MC code based on PENELOPE (Salvat et al., 2008) used in current thesis. Compared with other codes, PeneloPET is easy to use and acquires less simulation time.

2.8. *Image reconstruction algorithms in PET*

The basic role of image reconstruction is to convert the counts at projections measured at many different angles around the object, into a image that quantitatively reflects the distribution of positron-emitting atoms. There are two basic approaches to image reconstruction. One approach is *analytic* (Zanzonico and Heller, 2007) in nature and utilizes the mathematics of computed tomography that relates line integral measurements to the activity distribution in the object. The paradigm of these algorithms is the *filtered back-projection* (FBP) method. The second kind of reconstruction methods is statistic-*iterative*. These model the data collection process in a PET scanner and attempt, in a series of successive iterations, to find the image that is most consistent with the measured data.

This section contains an overview of some image reconstruction algorithms used in PET.

2.8.1. Rebinning

In this thesis, we mean by rebinning algorithms the ones employed to sort data from oblique sinograms of a 3D data set into the corresponding planes of a 2D data set. In this way, it is possible to reconstruct a 3D data set with conventional 2D reconstruction schemes, while maintaining the high sensitivity of 3D acquisitions. Mainly two approaches are used in clinical routine: single slice rebinning (SSRB) and Fourier rebinning (FORE) (Defrise et al., 2005; Defrise and Gullberg, 2006).

Single-slice Rebinning (SSRB)

The 3D data sinograms are considered to consist of a set of 2D parallel projections, and the FBP is applied to these projections. However, the complexity, large volume, and incomplete sampling of the data are some of the factors that limit the use of the FBP directly for reconstruction of 3D data.

To circumvent these difficulties, a modified method of handling 3D data is commonly used. A method of 3D reconstruction involves the rebinning of the 3D acquisition data into a set of 2D equivalent projections, Figure 2.12. Rebinning is achieved by assigning axially tilted LORs to transaxial planes (plane perpendicular to the scanner axis) intersecting them at their axial midpoints. This is equivalent to collecting data in a multiple ring scanner in 2D mode, and is called the single slice rebinning algorithm (SSRB). This method works well along the central axis of the scanner, but steadily becomes worse with increasing radial distance. This approximate algorithm is based on the assumption that each measured oblique LOR only traverses a single transaxial section within the support of the tracer distribution. Then each oblique LOR can be converted into a LOR belonging to the transaxial plane halfway to the planes containing the extremities of the original LOR (Defrise et al., 2005). This is illustrated in Figure 2.13.

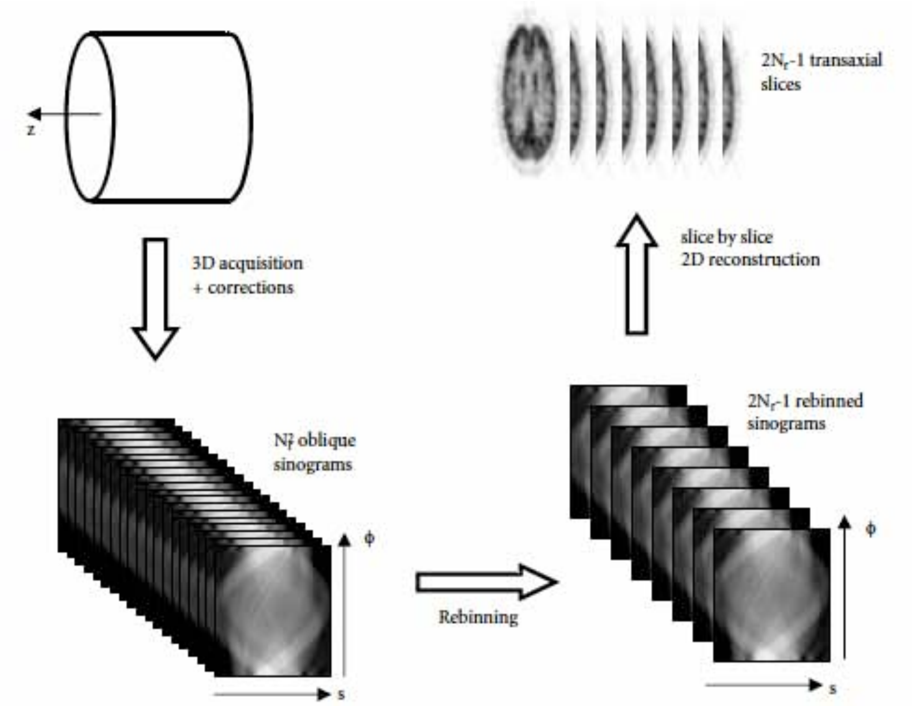

Figure 2.12. Schematic representation of the principle of a rebinning algorithm for 3D PET data. Adapted from (Defrise et al., 2005).

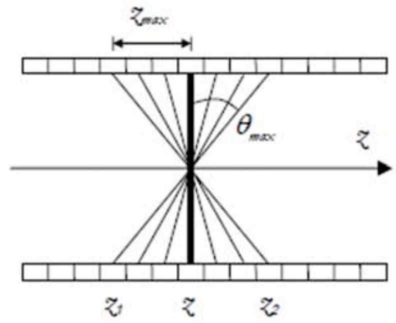

Figure 2.13. SSRB; an illustration of the set of oblique LORs transformed into a single transaxial LOR

Mathematically, the SSRB algorithm can be expressed as follows (Defrise et al., 2005):

$$S_{ssrb}(s,\phi,z) = \frac{1}{2\theta_{\max}(s,z)} \int_{-\theta_{\max}}^{\theta_{\max}} S(s,\phi,z = z,\theta)\,d\theta \tag{2.19}$$

$$\theta_{\max}(s,z) = \arctan\left(\frac{\min\{z, L - z\}}{\sqrt{R_d^2 - s^2}}\right) \tag{2.20}$$

where $\theta_{\max}$ is the maximum axial aperture for an LOR at distance x' from the axis in slice z, R_d is the scanner radius and L the number of transaxial sections sampled.

An inspection of the assumptions SSRB is based on, restricts the use of this algorithm for activity distributions that are spanned within a short radial distance from the scanner axis, as well as for LORs corresponding to small values of θ. For realistic distributions these conditions can not be met and the accuracy of this algorithm is very limited. The main advantage of SSRB is its simplicity.

Fourier Rebinning (FORE)

In another method, called the Fourier rebinning (FORE) algorithm, rebinning is performed by applying the 2D Fourier method to each oblique sinogram in the frequency domain. This method is more accurate than the SSRB method (Defrise et al., 2005) because of the more accurate estimate of the source axial location, and extends the range of 3D PET studies that can be processed using rebinning algorithms (Herraiz, 2008). An ideal rebinning transformation would place each 3D event into its correct 2D direct plane location or locations. The FORE algorithm provides a fast transformation from 3D data to 2D data based on a second-order Taylor series approximation of the 3D Fourier transformation of the data.

Rebinning is based on the relation between the Fourier transforms of oblique and direct sinograms (Bailey, 2005a). It is given by:

$$P_s = (v,k,z,0) @ P_s(v,k,z = z + k\tan q\,/\,(2pv), q) \qquad (2.21)$$

where k is the azimuthal Fourier index. The FORE method amplifies slightly the statistical noise, compared to SSRB, but results in significantly less azimuthal distortion.

2.8.2. Analytical methods

The central-section theorem states that the Fourier transform of a one-dimensional projection is equivalent to a section, or profile, at the same angle through the center of the two-dimensional Fourier transform of the object (Defrise et al., 2005). The central-section theorem is illustrated in Figure 2.14, where $¡_1\{p(s,f)\}$ is the one-dimensional Fourier transform of a projection, $¡_2\{f(x,y)\}$ is the two-dimensional Fourier transform of the image, and v_x is the Fourier space conjugate of x. The central-section theorem indicates that if we know $p(v_s,f)$ at all angles, then we can fill in values for $F(v_x,v_y)$. The inverse two dimensional Fourier transform of $F(v_x,v_y)$ will give $f(x,y)$.

$$p(v_s,f) = ¡_1(p(s,f)) = ¡_2(f(x,y))\big|_f = F(v_x,v_y)\big|_f \qquad (2.22)$$

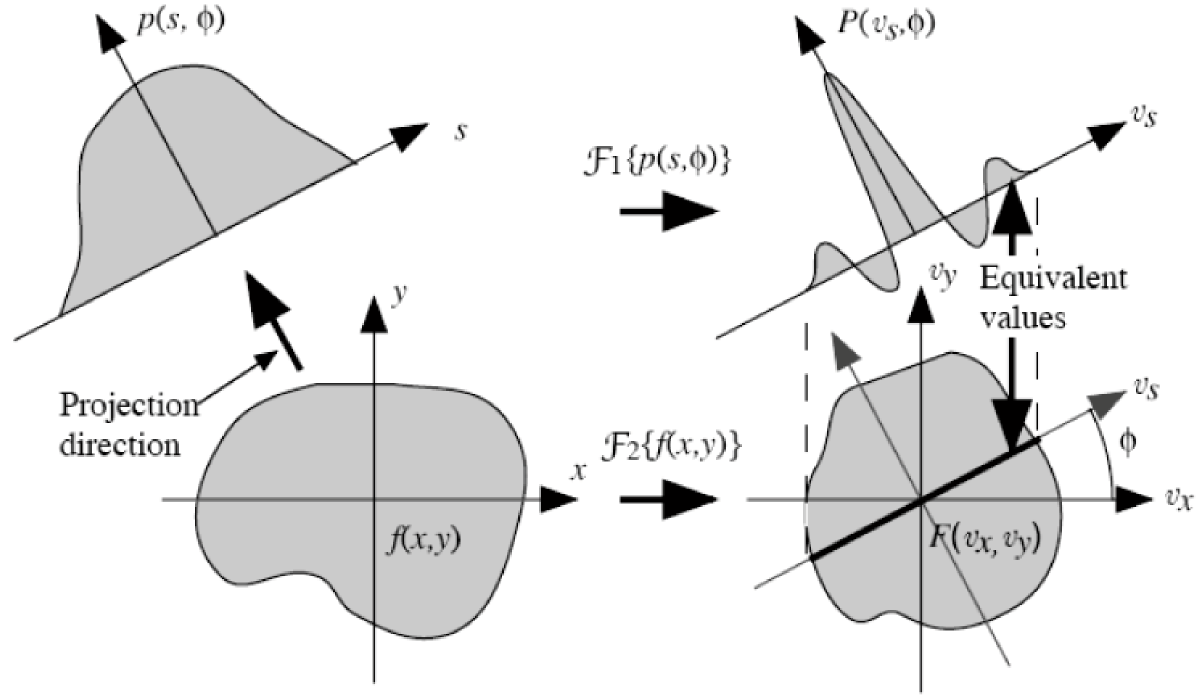

Figure 2.14. Pictorial illustration of the two-dimensional central-section theorem, showing the equivalency between the one-dimensional Fourier transform (top right) of a projection at angle ϕ (top left) and the central-section at the same angle (bottom left) through the two dimensional Fourier transform of the object (bottom right) (Bailey, 2005a).

Back-projection is the adjoint operation to the forward projection process that yields the projections of the object. Figure 2.15 shows the back-projection along a fixed angle ϕ. Conceptually, back-projection can be described as placing a value of $p(s,\phi)$ back into an image array along the appropriate LOR but, since the knowledge of where the values came from was lost in the projection step, a constant value is placed into all elements along the LOR (Henkin et al., 2006).

Due to the oversampling in the center of the Fourier space, back-projection of all the collected projections will not be enough to return a good image. In other words, each projection fills in one slice of the Fourier space resulting in over sampling in the center and less sampling at the edges. This over sampling in the center of Fourier space needs to be filtered in order to have equal sampling throughout the Fourier space. Basically, the Fourier transform of the back-projected image must be filtered with a ramp filter $(|v| = \sqrt{v_x^2 + v_y^2})$. This cone filter accentuates the values at the edge of the Fourier space and reduces the values at the center.

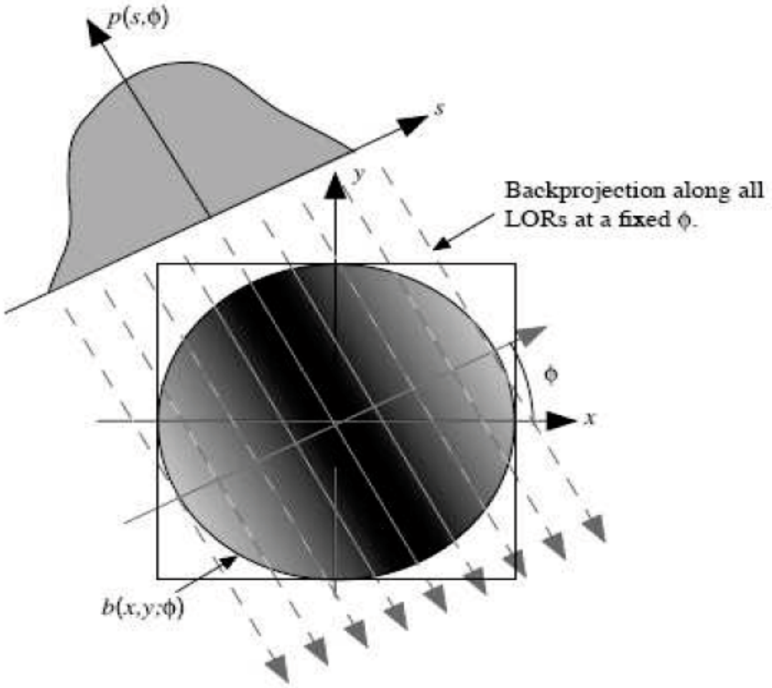

Figure 2.15. Back-projection, [illegible]*, into an image reconstruction array of all values of* [illegible] *for a fixed value of* ϕ *(Henkin et al., 2006).*

The **filtered-back-projection** (FBP) reconstruction method is the most well known standard method for reconstruction which applies the concept of back-projection and filtering explained before. Within FBP, the general expression employed to calculate the source distribution from projection data is (Defrise et al., 2005):

[illegible] (2.23)

Where [illegible] is the smoothing function that can take any shape (Henkin et al., 2006). For further noise reduction in the image an additional filter can be employed, such as Hamming or Butterworth (Cherry et al., 2003).

Analytical algorithms, and FBP in particular, are linear and, thereby, allow an easier control of most of their well known properties (i.e. spatial resolution), something crucial for quantitative data analysis (Defrise et al., 2005). Furthermore it is a standard reconstruction method for comparison of scanners (Goertzen et al., 2012). However it has some disadvantages, that it assumes Gaussian, instead of Poisson noise, therefore it creates streak artifacts (Cherry et al., 2003), also it does not allow resolution recovery compared to iterative methods. Additionally it could produce images with spurious negative values.

2.8.3. Iterative methods

Iterative reconstruction algorithms are based on a mathematical model of the physics of

PET or SPECT. The imaging process of obtaining the $y(i)$ counts on each of the i pair of detectors, from an object discretized in $x(j)$ voxels, can be described by the operation:

$$y(i) = \sum_j A(i,j)x(j) \tag{2.24}$$

where $A(i,j)$ is the system response matrix (SRM). The vector $x(j)$ and $y(i)$ corresponds to the voxelized image and the measured data respectively. In the analytical reconstruction framework; $x(j)$ is equivalent to $f(x,y)$, and $y(i)$ equivalent to $p(s,f)$.

Each element $A(i,j)$ is defined as the probability of detecting an annihilation event coming from image voxel j by a detector pair i . This probability depends on factors such as the solid angle subtended by the voxel to the detector element, the attenuation and scatter in the source volume and the detector response characteristics.

The *forward projection* operation just introduced above estimates the projection data from a given activity distribution of the source. Backward projection is the transposed operation of forward projection; it estimates a source volume distribution of activity from the projection data. The operation corresponds to:

$$b(j) = \sum_i A(i,j)y(i) \tag{2.25}$$

where $b(j)$ denotes an element of the backward projection image. Both the forward and backward projection operations require the knowledge of the SRM (Frese et al., 2003; Herraiz et al., 2006; Rafecas et al., 2004). Iterative reconstruction algorithms repeatedly use the forward and backward projection operations, which are the most time-consuming part of iterative reconstruction programs. Some implementations trade accuracy for speed by making approximations that neglect some physical processes, such as positron range, scatter and fractional energy collection at the scintillators or visible light loses in the detectors (Lee et al., 2000; Vaquero et al., 2004; Yamaya et al., 2003). This approach simplifies these operations to increase speed, but this trade-off often leads to non-optimal images.

2.8.4. EM – ML

The most widely applied algorithm for finding the maximum-likelihood (ML) estimation of activity f given the projections *p*, is the expectation maximization (EM). This was first applied to the emission tomography problem by Shepp and Vardi (Shepp and Vardi, 1982). ML, though, is a general statistical method, formulated to solve many different optimization problems of physics, biology, economy and others. The EM-ML algorithm can be written as (Herraiz et al., 2006):

$$f^{it+1}(V) = f^{it}(V)\frac{\sum_{L} SRM(L,V)\frac{p(L)}{\sum_{V'} SRM(L,V')f^{it}(V')}}{\sum_{L} SRM(L,V)} \tag{2.26}$$

where $f^{it+1}(V)$ is the expected value of voxel V at iteration it, p is the data acquired and *SRM* is the *system response matrix*. The *SRM* is a precalculated matrix that contains the probability that one emission occurred at voxel V is detected in a detector element L. The accuracy of this matrix will be extremely important for the quality of the images resulting from the reconstruction method (Mumcuoglu et al., 1996).

Usually, iterative algorithms based on ML statistical models assume that the data being reconstructed retain Poisson statistics (Shepp and Vardi, 1982). However, to preserve the Poisson statistical nature of data, it is necessary to avoid any pre-corrections (Qi et al., 1998) to the data. Corrections for randoms scatter and other effects should be incorporated into the reconstruction procedure itself, rather than being applied as pre-corrections to the data. At times, sophisticated rebinning strategies are employed to build sinograms into radial and angular sets. This also changes the statistical distribution of the data, which may no longer be Poisson (Kadrmas, 2004).

A serious disadvantage of the EM procedure is its slow convergence (Lewitt et al., 1994). This is due to the fact that the image is updated only after a full iteration is finished, that is, when all the LORs have been projected and back projected at least once. In the ordered subset EM (OSEM) algorithm, proposed by (Hudson and Larkin, 1994), the image is updated more often, which has been shown to reduce the number of necessary iterations to achieve a convergence equivalent to that of EM, as the convergence is approximately proportional to the number of image updates.

According to the literature, EM methods have another important drawback: noisy images are obtained from over-iterated reconstructions, and this is usually attributed to either the fact that there is no stopping rule in this kind of iterative reconstruction (Johnson, 1994) or to the statistical (noisy) nature of the detection process and reconstruction method (Bettinardi et al., 2002; Biemond et al., 1990). In practice, however, an image of reasonable quality is obtained after a few iterations (Hudson and Larkin, 1994).

Several techniques have been proposed to address the noisy nature of the data: filtering the image either after completion of the reconstruction, during iterations or between them (Slijpen and Beekman, 1999), removal of noise from the data using wavelet based methods (Mair et al., 1996) or smoothing the image with Gaussian kernels (Sieves method) (Liow and Strother, 1991; Snyder et al., 1987).

Maximum a priori (MAP) algorithms are also widely used (Green, 1990). MAP adds *a* priori information during the reconstruction process, the typical assumption being that, due to the inherent finite resolution of the system, the reconstructed image should not have abrupt edges, at least not more abrupt that what one can expect from the resolution of the system. Thus, MAP methods apply a penalty function to those voxels which differ more than a certain threshold from their neighbors. Whether the maximum effective resolution achievable is limited, by the use of these methods, is still an open issue (Alessio et al., 2003). On the other hand, a proper choice of reconstruction parameters, such as number of iterations, the use of an adequate system response and a smart choice of subsetting, would yield high quality images with the EM procedure (Herraiz et al., 2006).

2.8.5. Time-of-flight (TOF)

The time-of-flight (TOF) is the time difference between detection of the two photons produced by the positron annihilation. High resolution measurement of this time difference would allow one to determine the precise location at which the annihilation occurred. Although the idea of utilizing this TOF information appeared in the 1960s (Budinger, 1983), lack of fast scintillators has limited building practical TOF PET systems until the recent development of fast detectors such as LSO (Melcher and Schweitzer, 1991; Moszynski et al., 2006; Moses and Derenzo, 1999) and $LaBr_3$ (Kuhn et al., 2004; Surti et al., 2006).

Most of the TOF PET systems developed in the 80’s were 2D systems where each transverse plane is reconstructed using mostly 2D analytical reconstructions (Snyder et al., 1981; Tomitani, 1981). In principle, localization of the point of annihilation, that is, image reconstruction, can be performed directly if we can measure the time difference with enough precision. As the TOF resolution of the scanners is far from ideal (but improving every year), reconstructin methods must still be employed, for which the introduction of TOF information help increasing the SNR of the reconstructed image (Harrison et al., 2005; Manjeshwar et al., 2005; Moses, 2003; Snyder et al., 1981; Tomitani, 1981). As indicated in (Moses, 2003), and described analytically in (Snyder et al., 1981; Tomitani, 1981; Vunckx et al., 2010), the SNR improvement in TOF PET image reconstruction is determined by the TOF timing resolution.

We will give some ideas about the present status of TOF. The distance Δx of the annihilation point from the center of the (LOR) (Figure 2.16) is related to the time difference Δt by:

$$\Delta x = \Delta t \cdot c / 2 \tag{2.27}$$

where c is the speed of light.

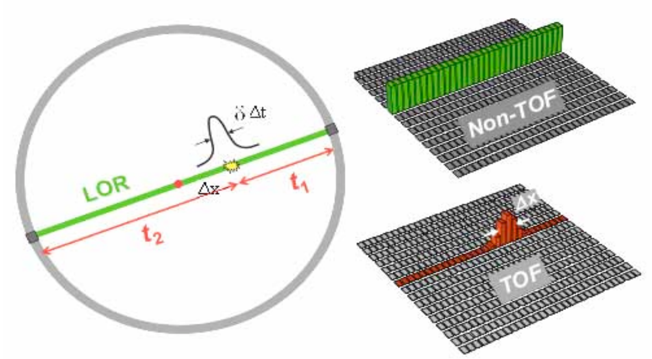

Figure. 2.16. Principle of TOF improvement of annihilation localization along the LOR

The system TOF resolution Δt in Figure. 2.16) of the scanner is defined as the Full-Width-at-Half-Maximum (Δt_{FWHM}) of the distribution of time differences collected from a centered point source. According to Equation 2.29, in order to achieve a spatial resolution better than 1 cm, a TOF resolution of 66 picoseconds would be required. In previous generations of commercial scanners, the TOF resolution was of the order of 1 ns (Moses, 2003). However, current PET/CT scanners have obtained TOF resolutions of the order of 500 ps, which offer the opportunity of using TOF information to improve the quality of the reconstructed images (Conti et al., 2005). Indeed, employing TOF information, image background, which is essentially noise, can be reduced. We expect a system time resolution of around 550 ps for current LSO based systems (Moses and Ullisch, 2006) and the race for systems with 300 ps TOF resolution or better has started (Zaidi et al., 2011).

3. PeneloPET simulations of Clinical Scanners

There are unavoidable tradeoffs when choosing the characteristics of a PET scanner. For instance, by increasing the length of the scintillator crystal, the sensitivity of the scanner improves but spatial resolution diminishes due to depth-of-interaction (DOI) effects (Kunze et al., 2000). Increasing the number of detector rings improves sensitivity, but also the complexity and cost of the PET scanner. Therefore, the selection of parameters should be carried out carefully. Simulation tools are of invaluable help for this purpose. Indeed, MC simulations are widely used in PET to optimize detector design and acquisition protocols (Braem et al., 2004; Heinrichs et al., 2003), and for developing and assessing corrections and reconstruction methods (Buvat and Castiglioni, 2002; Herraiz et al., 2006). MC methods make it possible to estimate scanner properties which cannot be easily determined experimentally, as well as to assess the change in performance of PET scanners induced by modifications in scanner characteristics (Zaidi, 1999). In recent years, the availability of powerful computers facilitated widespread use of PET-dedicated simulation codes (Agostinelli et al., 2003; Baro et al., 1995; Briesmeister, 1993; Harrison et al., 1993; Kawrakow and Bielajew, 1998; Thompson et al., 1992).

PeneloPET (España et al., 2009) is a Monte Carlo code based on PENELOPE (Salvat et al., 2008), which allows for fast and easy simulation of PET scanners. PeneloPET models the detector geometry and materials, the acquisition electronics, and the source. All these components are configured by means of a few plain text input files (España et al., 2009). PeneloPET simulations can easily be performed in a cluster of computers.

As has been mentioned, newer clinical PET scanners include time-of-flight (TOF) capability, which offers the opportunity of using this TOF information to improve the quality of the reconstructed images (Conti et al., 2005). Indeed, employing TOF information, image background, which is essentially noise, can be reduced. One of the goals of this work is to assess the capability of PeneloPET to include TOF properties of clinical scanners.

In this chapter we present results of simulations performed with PeneloPET. While PeneloPET has been validated and employed to simulate preclinical scanners (España et al., 2009), here we report for the first time detailed comparisons of PeneloPET simulations to real data for clinical scanners. The specific materials for each particular task are described in their corresponding sections for major clarity. Section 3.1 presents the main features of the Monte Carlo simulation tool and description of PeneloPET code in addition to PENELOPE algorithm. Materials and methods are followed in the next section (3.2), which includes scanners geometry definition, and performance evaluation of the Biograph scanner. Results and conclusion are following in sections 3.3 and 3.4 respectively.

3.1. Monte Carlo simulation: PeneloPET

PeneloPET is easy to use and fast MC code. Fast simulation was achieved without loosing simulation detail. For its versatility, speed and easy to analyze outputs, PeneloPET is a tool useful for scanner design, and estimation of system response. In the following section we will describe its main characteristics. For additional details see (España et al., 2009).

3.1.1. PeneloPET features

PeneloPET (España et al., 2009) is a Monte Carlo simulator based on PENELOPE (Salvat et al., 2008), which is written in FORTRAN. PENELOPE is a MC code for the simulation of the transport in matter of electrons, positrons and photons with energies from a few hundred *eV* to 1 *GeV*. It is then less generally aimed as GEANT4, but it suits well PET needs, it is fast and robust, and it is extensively used for other medical physics applications, particularly for dosimetry and radiotherapy (Panettieri et al., 2007; Sempau and Andreo, 2006; Vilches et al., 2006). The FORTRAN language used for PENELOPE as its highly standardized and it is available in many computer architectures, aimed to scientific computing, to which FORTRAN compilers have been adapted and optimized for speed and accuracy. On these grounds, PeneloPET has been developed, a FORTRAN package that allows to easily defining complete simulations of PET systems within PENELOPE.

PeneloPET has been developed by our group (GFN, Universidad Complutense Madrid) as a PhD thesis by Samuel España (España, 2009). PeneloPET simulates PET systems based on crystal array blocks coupled to photo detectors and allows the user to define radioactive sources, detectors, shielding and other parts of the scanner with a few input files. The code was at first intended for small animal PET scanners (España, 2009) but nothing prevents its use to clinical scanners. In this chapter we study the suitability of

PeneloPET for clinical scanners. The use of PeneloPET facilitates the description of the different components necessary for the accurate modeling of a PET system, starting from the geometry configuration, up to the creation of a processing chain for the detected events. Thus analytical phantoms can also be defined through the use of these basic structures.

As said before, PeneloPET is capable of preparing sophisticated simulations just by editing a few simple input text files, without requiring knowledge of FORTRAN or any other programming language. Simulations prepared with PeneloPET can be run in parallel in clusters of computers. For doing that, a Python[1] script is available to run the code. The choice of Python allows to run the script under Windows, Linux/Unix, and Mac OS X. The Python script launches the simulation on the number of CPUs desired, with different random seeds, and takes care of the initial activity and the acquisition time for each sub-process. In this way, the simulation time is reduced proportionally to the number of CPUs employed (España, 2009).

The basic components of a PeneloPET simulation are detector geometry and materials definition, source definitions, non-active materials in the field of view of the scanner, and electronic chain of detection. All these components are defined with parameters in the input files. The output data (i.e. sinograms, LORs histograms and list mode) can be exploiting with several programming languages. List mode generates files with all hits including types and time of coincidence events (random, scatter, true, and pile-up). A brief descriptions of PeneloPET input and output is given in the following sections.

3.1.1.1. Source code

PeneloPET requires a moderate time investment for the preparation of the simulation setup; the code is structured in two modules. The first one deals with the PENELOPE simulation, which takes care of the information about the scanner detectors and materials, source and decay. This module includes the routines involved in the distribution of isotopes and emission of particles generated in the decay processes, as well as their interactions.

The second module post-processes the decay and interaction data generated by the first module. It takes into account the anger logic for positioning the interaction inside the crystal array, detector pile-up, energy resolution, and aspects of the electronics (i.e.

---

[1] http://www.python.org/

coincidence time window, dead time, time resolution, and integration time). The energy window can be applied in this module. In this module no PENELOPE routines are involved. Finally continuous or pixilated detectors can be managed by this second stage of the simulation package.

3.1.1.2. Description of input files

In order to setup the simulation, four files have to be prepared by the user. As an example, Table 3.1 shows these input files for the simulation of a line source for the Biograph PET/CT scanner as described by (Jakoby et al., 2009).

The first input file in Table 3.1 (*main.inp*) contains the general parameters of the simulation, such as the acquisition protocol and acquisition time. It also enables simulation of secondary particles, and controls whether positron range and non-collinearity are taken into account. It contain options for scanner rotation, energy and coincidence windows, contributions to dead time, output format, and type of study.

In the second file (*scanner.inp*), which contains the scanner definition, multiple rings and layers, material and size of crystals can be specified. Reflector thickness as well as energy resolution, rise and fall time and scanner radius also can be easily introduced.

Non-radioactive materials other than the scintillator (already defined in the file scanner.inp), such as surrounding materials and shielding, are defined in a third file (*object.inp*). The radioactive source is defined separately in a fourth input file (*source.inp*), which contains source geometry and information about activity and isotope. Keeping separated definitions for sources and materials simplifies the comparison of simulations of ideal sources, without scatter or attenuation, to more realistic sources. Details about PeneloPET input files and options can be found in the PeneloPET manual[2].

Typical materials for crystals, shielding and phantoms are predefined in PeneloPET and, if necessary, new materials can be created in a straightforward way. The visualization tools built in PENELOPE (gview2d, gview3d (Salvat et al., 2006)) are also available in PeneloPET to display and test geometries. This is especially useful during scanner design stages (see Figure 3.2).

---

[2] http://nuclear.fis.ucm.es/penelopet/

Table 3.1. PeneloPET input files needed to simulate a cylinder source in the Biograph scanner (Jakoby et al., 2009); 'F' stand for false or disable option and 'T' stand for true or enable option. Full detail about this input file and options can be found in the PeneloPET manual.

----GENERAL PARAMETERS--- (main.inp)

```
12345 54321              !Random number generator seeds
500 1 F                  !Acquisition Real Time[sec]; Number of Frames; Read frame_list.inp
F                        !read alignments.inp file
F F                      !read coinc_matrix.inp
1000                     !Limit for the number of interactions in each particle
F T T F                  !Secundary Particles Simulation; Positron Range; Non-Collinearity;
Generate range profile
0 0 1 1                  !Start&Stop Angles [DEG]; Number of Steps per cycle; time per cycle
[sec]
4250000.                  !Lower Energy Window (eV)
650000.                          !Upper Energy Window (eV)
2.25                     !Coincidence Time Window (ns)
10                       !Triggers Dead Time (ns)]
120                      !Integration Time (ns)
80                       !Singles Dead Time (ns)
F F F                    !Hits LIST; Singles LIST; Coincidence LIST
F                        !Write Lor Histogram
F 336 336  38 11 F      !Write Sinogram; radial bins; angular bins; maximum radio; maximum ring
difference; span ;split
F 336 336 109 68 21.8  !Write Image; X Y Z voxels, Transaxial & Axial FOV (cm)]
F                        !Hits checking
T                        !Verbose
T                        !Get Rid more than 2 single en coincidencia
F                        !System Renponse Simulation:  LOR-RESPONSE
F                        !System Renponse Simulation:  SINOGRAM-RESPONSE
1        1        13     !Chord points - Transaxial Axial Longitudinal]
0.5      0.5      8.55   !Tranaxial (pitch times); Axial (pitch times); Longitudinal(cm)
2        5000000                 !Chord Aperture, Decays/Point
```

--- SCANNER PARAMETERS --- (scanner.inp)

```
48                       !Number of Detectors by Ring
26                       !Number of Detectors in Coincidence in the same Ring
4                        !Number of Rings
0.4                      !Gap Between Rings [cm]
13                       !Number of transaxial crystals by Detector [COLUMNS]
13                       !Number of axial crystals by Detector [ROWS]
1                        !Number of crystal layers by Detector
2.0 8 0.12 0.8 40 0.5    !Length[cm]; Material; Energy Resol; Rise T[ns]; Fall T[ns], Time Resol
[ns]
0.4 0.4 0.04            !Pitch (Transaxial; Axial): Distance between center of adyacent crystals,
Reflector thickness  [cm]
42.8                       !Radio: Center FOV - Center Front of Detector [cm]
```

---Body parameter--- (object.inp)

```
!TYPE MATERIAL X_CENTER Y_CENTER Z_CENTER R1 R2 HEIGHT[cm] PH_INC
TH_INC[DEG]
 C 1 0 0 0 0 10 70.0 0 0
```

---Source PARAMETER --- (source inp)

```
!TYPE ACTIVITY[Bq] UNITS ISOTOPE Material X Y Z R1 R2 H[cm] PH_INC TH_INC PH TH
TH1 TH2[DEG]
 C 3.9e6 F 1 1 0 0 0 0 0.05 70 0 0 0 0 0 180
```

3.1.1.3. Description of output files

Three levels of detail output are offered by PeneloPET, categorized as high, intermediate and lower detail. Information regarding each interaction to be recorded for further analysis is classified as the highest level. In intermediate level the single events are recorded for further analysis, finally at the third and lowest, level of detail only coincidence events are recorded in a compact LIST mode. Information about pile-up, scatter, random and self-coincidence events, obtained from the simulation, is also summarily available.

As seen in the introduction, there are different kinds of ‘coincidence’ events and all of these are listed in PeneloPET outputs. Pile-up coincidences occur when at least one of the single events has suffered pulse pile-up. When two photons in the coincidence pair come from uncorrelated annihilation process, then we have a random coincidence in PeneloPET output. As well, coincidences will be categorized as scatter, when at least one of the photon considered has interacted before reaching the scintillator. Self-coincidence flag are given to events for which the same photon, after scattering in a first detector, reaches a second detector. If the energy deposited in each detector is above the detection threshold, it may trigger two single events and yield a self-coincidence count. The remaining coincidences are labeled as true events.

Several output histograms are generated by PeneloPET, for further understanding and analysis such as sinogram projections, LOR histogram and energy spectrum. PeneloPET output can be converted into ROOT format (Brun and Rademakers, 1997) for further analysis with the tools provided in PeneloPET. In order to simplify the reconstruction of simulated data, the format of the sinograms conforms to that expected by the STIR library[3]. In this thesis we converted the list-mode to a ROOT format to produce sinograms as well as to study the time resolution of the scanner, which will be explained later in this chapter.

3.1.2. PENELOPE

As it was mentioned earlier, PENELOPE (Salvat et al., 2008) is a code for MC simulation, it is suitable for good range of energy, and allows for complex materials and geometries. PENELOPE is being broadly employed, with numerous applications in the field of medical physics (Panettieri et al., 2007; Sempau and Andreo, 2006).

PENELOPE consists of a package of subroutines (FORTRAN77 programming

---

[3] http://stir.sourceforge.net

language), invoked by a main program that controls the evolution of the stories of particle counters and accumulates the magnitudes of interest for each specific application.

These subroutines are distributed by Nuclear Energy Agency - Organization for Economic Co-operation and Development (NEA-OECD). The authors are Francesc Salvat and Jose M. Fernández-Varea of the Physics Department of the Universidad de Barcelona and Josep Sempau of the Institute of Energy of the Universidad Politécnica de Cataluña (Salvat et al., 2008).

The simulation of electrons and positrons includes the following types of interactions:

- Hard elastic collision $(\theta > \theta_c)$.
- Hard inelastic collision $(\theta > \theta_c)$.
- Hard Bremsstrahlung emission.
- Delta interaction.
- Artificially soft event $(\theta < \theta_c)$.
- Inner-Shell impact ionization.
- Annihilation (only for positrons).
- Auxiliary interaction (photonuclear interactions simulation).

The simulation of photons includes the following interactions:

- Coherent scattering (Rayleigh).
- Incoherent scattering (Compton).
- Photoelectric absorption.
- Electron-Positron pair production.
- Delta interaction.
- Auxiliary interaction.

For further explanation of the physics included in these interactions can be found in this reference (Salvat et al., 2008). The use of PENELOPE requires preparing a main program which will be responsible for calling the PENELOPE subroutines and for storing the information about the trajectories of the particles simulated.

The main program should provide PENELOPE with the information about the geometry and materials, and also other parameters as type of particle, energy, position and direction of movement of the particle to be simulated. The user can create a simulation environment through appropriate use of these tools. PENELOPE is of relatively common use in experimental nuclear physics and medical physics (Panettieri et al., 2007). For further information of PENELOPE and how it is used in PeneloPET can be found in (España, 2009).

3.2. Materials and methods

3.2.1. Geometry of the BIOGRAPH family of PET/CT scanners

In this work we investigated the Biograph PET/CT family: Biograph True-point (B-TP), Biograph Tue-point True V (B-TPTV) and Biograph mCT (B-mCT). In addition, we also considered hipotetical scanners built out of more rings than the existing ones, and thus with an extended axial FOV. In this section we will describe the general characteristics of the three scanners mentioned above, and then we will focus in B-TPTV characterization as it is used to set the simulation parameters to perform a study of the other scanners.

The B–TP scanner has three rings of 48 detector blocks, each comprising 13 x 13 crystals (4 x 4 x 20 mm^3) coupled to 4 photomultiplier tubes. This configuration covers an axial field-of-view (FOV) of 16.2 *cm* resulting in 81 image planes with a slice thickness of 2 *mm* (Jakoby et al., 2009).

The B-TP with TrueV (B-TPTV) scanner incorporates four rings of the same detector blocks as in the B-TP, so extending the axial FOV to 21.8 *cm* with 109 image planes, each 2 *mm* thick. Both scanners (B-TP and B-TPTV) operate in 3-dimensional (3D) mode (Jakoby et al., 2009), with a maximum ring difference of 38 and 27 respectively. Also the two PET scanners operate with a 4.5 *ns* coincidence time window and a 425–650 *keV* energy window.

The Biograph mCT PET scanner (Jakoby et al., 2011) is essentially based on the same geometry as the B-TPTV but acquires data with an extended ring difference of 49. Furthermore the patient bore on the mCT scanner is 78 *cm,* compared to 70 *cm* on the B-TPTV. Table 3.2 shows the main parameters of the PET scanners described above (Jakoby et al., 2011, 2009).

Table 3.2. Parameters of the Biograph PET/CT scanners evaluated (Jakoby et al., 2011, 2009)

Scanner	*B-TPTV*	*mCT*	*B-TP*
Number of block rings	*4*	*4*	*3*
Block detector per ring	*48*	*48*	*48*
Detector elements dimension	*4x4x20 mm*	*4x4x20 mm*	*4x4x20 mm*
Detector Material	*LSO*	*LSO*	*LSO*
Total crystal number	*32448*	*32448*	*24336*
Axial FOV	*218 mm*	*218 mm*	*162 mm*
Transaxial FOV	*680 mm*	*700 mm*	*605 mm*
Slice thickness	*2 mm*	*2 mm*	*2 mm*
Number of image planes	*109*	*109*	*81*
Coincidence time window	*4.5 ns*	*4.1 ns*	*4.5 ns*
Energy window	*425-650 KeV*	*435-650 KeV*	*425-650 KeV*
Energy resolution	*11.7%*	*11.5%*	*12%*
Pitch size	*4 mm*	*4 mm*	*4 mm*
Reflector thickness (estimated)	*0.4 mm*	*0.4 mm*	*0.4 mm*
Crystal length (thickness)	*2 mm*	*2 mm*	*2 mm*
Detector ring diameter	*856 mm*	*856 mm*	*856 mm*
CFOV -C. front of detector	*42.80 cm*	*42.80 cm*	*42.80 cm*

Besides these existing scanners, a study was made of the effect of an increased number of rings in the performance of these scanners, with results for 5, 8 and 10 rings. As we mentioned earlier, we will focus on B-TPTV scanner geometry, because it is used to set the electronic parameters (i.e. integration time, triggers dead time, integration time etc.) to investigate other scanners and to validate our MC code (PeneloPET).

The B-TPTV (Siemens Molecular Imaging) combines a 16-slice helical CT scanner (Somatom Sensation 16; Siemens Medical Solutions) with a whole-body LSO PET scanner. Figure 3.1 presents the B-TPTV[4].

---

[4] http://www.medical.siemens.com

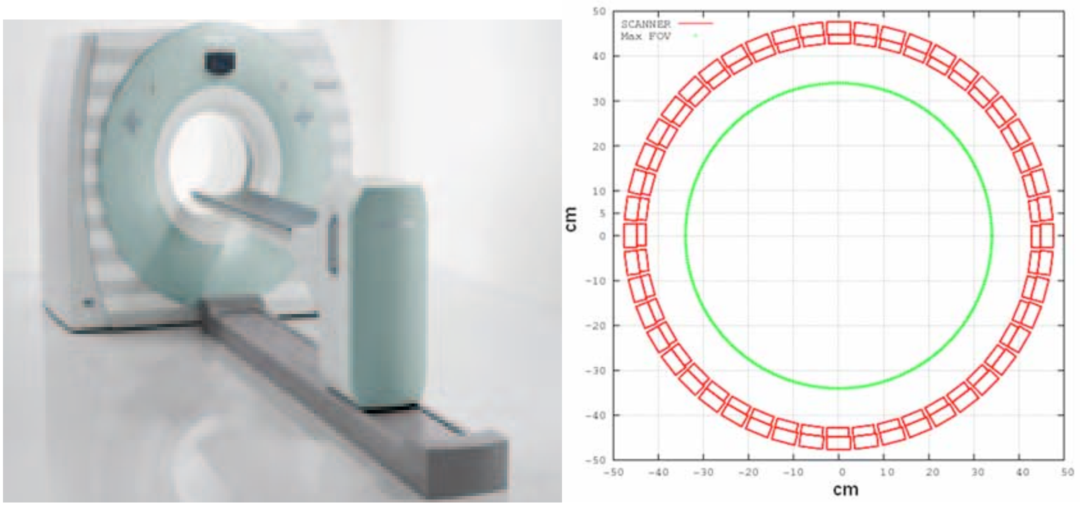

(a) (b)

Figure 3.1. B-TPTV PET/CT scanner geometrized by Siemens (a) and a transverse section of the transaxial FOV of the scanner, with scintillations detectors (b)

By using gview3D offered by PENELOPE we can visualize the scanner geometry. Figure 3.2 shows the B-TPTV scanner geometry as well as the NEMA test phantom at the center of the scanner.

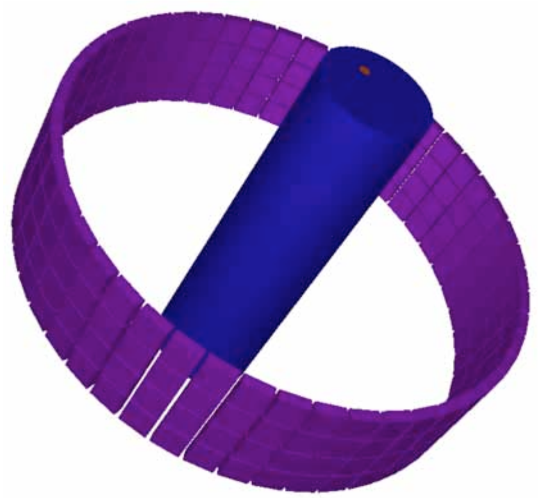

Figure 3.2. Scanner geometry of the B-TPTV scanner (detector modules) with the NEMA test phantom at the middle of the scanner.

3.2.2. Performance evaluation of the B-TPTV PET scanner

To objectively compare the performance of different clinical PET systems, they have been develops guidelines to allow an user, in the process of selecting a PET system, to obtain a relatively unbiased comparison of system parameters. We utilized the recently updated NEMA protocol NU 2-2007 (NEMA, 2007) which incorporates Watson's suggestions for PET instruments with intrinsic radioactivity (Watson et al., 2003) to compare spatial resolution, sensitivity, scatter fraction and noise equivalent count rate (NECR) to the experimental results. In addition, the stability of spatial resolution was measured. These performance parameters are seen as critical for good image quality. Comparison of these parameters for different commercial PET scanners can be found in these references: (Bailey, 2005b; Saha, 2010; Tarantola et al., 2003).

In this thesis, acquisitions for the B-TP, B-TPTV and B-mCT PET/CT scanners (Jakoby et al., 2011, 2009), in addition to an extended axial FOV scanners (Table 3.3) were simulated with PeneloPET.

Table 3.3. Characteristics of The PET Scanners Evaluated (from refs. (Jakoby et al., 2011, 2009)

Number of block rings	*Axial FOV (cm)*	*Maximum ring difference (MRD)*
B-TP (Jakoby et al., 2009)	*16.2*	*27*
B-TPTV (Jakoby et al., 2009)	*21.8*	*38*
mCT (Jakoby et al., 2011)	*21.8*	*49*
5-rings	*27.2*	*38*
8-rings	*43.6*	*38*
10-rings	*54.5*	*38*

When simulating an existing scanner, it may be the case that not every parameter of the scanner is known with complete certainty. Often, details of the geometry, materials, acquisition electronics or the processing chain of coincidences are not available. Most often, the electronics acquisition performance is not known. But figures of this performance, such as prompt, randoms, true and NEC curves are available.

PeneloPET includes simulations of acquisition electronics. Actually, it allows for different independent dead time sources. There is a *singles* dead time, which applies to every photon that reaches the scanner detectors. Further there is also a *coincidences* dead time, representing the further dead time involved in the processing of events identified as coincidences. Also, integration time, pile-up (and pile-up rejection) effects, (Vicente et al., 2012a, 2011) are included in PeneloPET.

To asses the stability of PeneloPET for clinical scanners, we take the published values (Jakoby et al., 2009) for sensitivity, noise equivalent count (NEC) rate and TOF capabilities of the B-TPTV scanner to assess that the simulations are well set.

In order to mimic the behaviour of a real PET scanner, where the full details of the electronics may not be known, we use some of the parameters which define in PeneloPET the acquisition electronics, as effective fitting variables adjusted to reproduce the experimental random counts, prompt counts and NEC curves of the B-TPTV scanner. Once fitted to the B-TPTV data, these parameters are unchanged when simulating the other scanners. Well known parameters of the scanner electronics, such as coincidence time and energy window, were set to the actual values of the real acquisitions (Jakoby et al., 2009).

As further validation, predictions of sensitivity, NEC and scatter fraction for the B-TP and mCT scanners were compared to the published measurements. And finally, once the simulations have been setup and validated, they have been used to study the effect of varying parameters, such as crystal length, number of detector rings, energy resolution, coincidence time and energy windows, on the performance of Biograph scanner (B-TPTV).

3.2.3. *Sensitivity*

Acquisition method

PeneloPET simulations were performed to estimate the system sensitivity, following the NEMA protocol NU 2-2007. A 70 *cm* long polyethylene tube with an inner diameter of 1 *mm* was activated with 3.9 MBq of ^{18}F. This activity is low enough to assure that dead time losses were less than 1% and that the ratio of random to true events was less than 5%. The sensitivity at two transaxial positions (0 and 10 *cm*) was obtained. Simulations accumulated more than 10^6 detected events at each position. The simulations employed the same maximum ring difference (27 and 38 for B-TP and B-TPTV, respectively, and 49 for mCT) as the acquisitions of the real scanners (Jakoby et al., 2011, 2009).

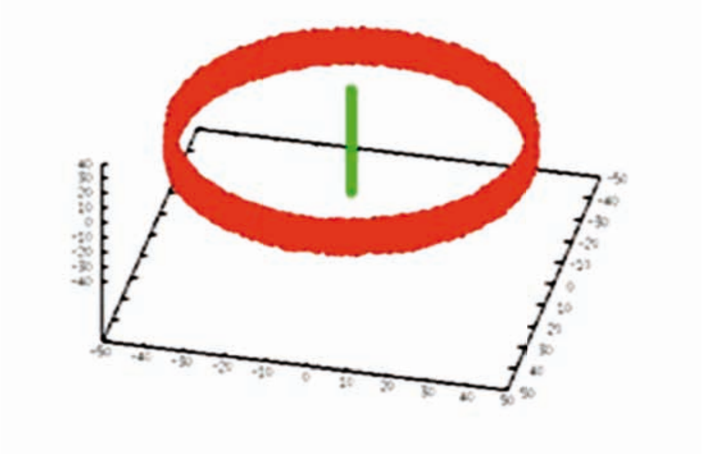

Figure. 3.3. Source emissions (green points) and interactions of the emitted photons with the detector crystals (red points).

In addition, the dependence of the sensitivity, on the number of block detector rings was explored. The simulations yield and estimation of the increase in sensitivity and count rate performance obtained with additional detector rings as well as with the increase of maximum ring difference. For the extended rings, one has to note that the maximum ring difference was kept constant to the same value as the one of the mCT scanner, namely 48. Figure 3.3 shows the PeneloPET output simulation of B-TPTV, a line source emissions and interactions of the emitted photons with the detector crystals.

3.2.4. Scatter Fraction (SF) and Noise Equivalent Count (NEC) Rate

The SF is a critical component of the noise equivalent count (NEC) rate computation, widely used as a golden measure to optimize acquisition parameters such as timing and energy windows, and for making comparisons among clinical scanners. The fraction of coincidences that have scattered and yet are acquired within the applied energy window is known as SF (Bailey, 2005b). Scatter counts decrease image contrast, just like random counts. Following the NU 2-2007 protocol, the scatter fraction was measured from low activity simulations, where random counts are negligible (NEMA, 2007).

Another important parameter of a PET scanner is the NEC rate that we described in Chapter 2 (section 2.6.5).

NEC is plotted as a function of activity concentrations. The peak of the NEC curve depends on geometry, scanner materials, energy windows, and also on the acquisition electronics, mainly dead time and coincidence time window. In the simulation, the coincidence window was set to 4.5 *ns*, 11.7% energy resolution and the energy window was 425–650 *keV*. The simulated energy resolution was based on the reported energy resolution for LSO detectors (Jakoby et al., 2008).

Acquisition method

As we mentioned earlier we used NU 2-2007 protocol to determine both SF and NEC rate. A 70 *cm* long and 20 *cm* diameter polyethylene cylinder (see appendix A1) is placed with its isocenter in the isocenter of the FOV of the scanner. A 70 cm line source is activated with 1.04 *GBq* of ^{18}F (sufficient to achieve count rates beyond the peak of the NECR) and inserted axially into the cylinder whole, located 4.5 *cm* below the central phantom axis (see Figure 3.4). Data were simulated for 35 frames, spanning 10 hours of acquisition.

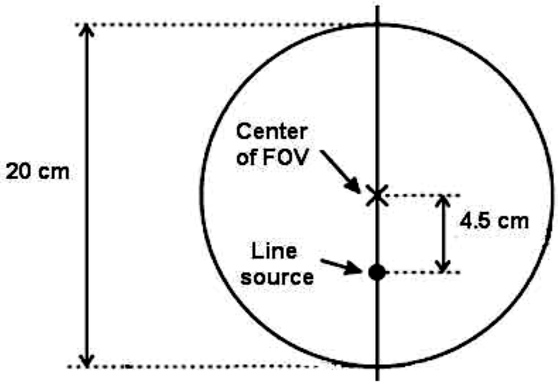

Figure 3.4. Positioning of the NEMA scatter phantom, used for the measurement of NEC and SF.

3.2.5. Spatial resolution

Acquisition method

Again, the NU 2-2007 protocol (NEMA, 2007) was followed to determine the resolution from simulated acquisitions; an ^{18}F activated point source with low activity in a glass capillary was modeled. The activity was low enough to assure a ratio of random to total events below 5%. Simulated data were acquired at two axial positions (center of the axial FOV and 1/4 off-center), at three (*x, y*) locations: (0, 1 *cm*), (10 *cm*, 0), and (0, 10 *cm*). The position of the point source is illustrated in Figure 3.5, where the spatial resolution was measured (NEMA, 2007) The acquisition time was long enough so that at least one hundred thousand counts were acquired for each position. The images were reconstructed using FBP (with ramp filter) from the sinogram data. The resulting images had 336 × 336 × 109 voxels with a voxel size of 2 × 2 × 2 mm^3.

The resulting images analyzed as follows: for each of the six point source images, the FWHM and FWTM measured for each of the 3 directions *x, y* and *z*. All the measures in the *x* and *y* plane are referred to as *transverse*, while those in the *z* direction are referred as *axial*.

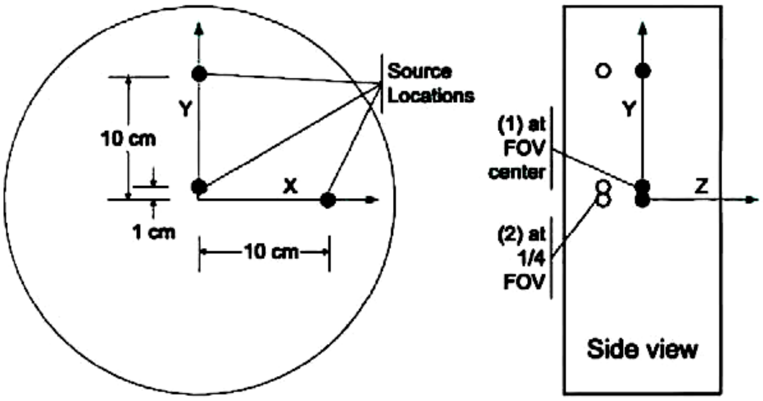

Figure 3.5. Arrangement of the six points sources in the measurement of spatial resolution. Three sources are positioned at the center of the axial FOV and three sources are positioned at one-fourth of the axial FOV away from the center. At each position, sources are placed on the positions indicated in a transverse plane perpendicular to the scanner axis (NEMA, 2007).

3.2.6. Time-of-flight (TOF)

PeneloPET simulations allow us to control the time resolution of the scanner, by tuning an additional parameter (time jitter) that can be manipulated to produce the expected time resolution.

Acquisition method

Time difference distributions were obtained from a 1 *MBq* of ^{18}F point source located at the center of the scanner. These distributions were fit to a Gaussian. The FWHM of the Gaussian was used as a measure of the TOF resolution.

3.2.7. Impact of Scintillator Crystal size and Energy resolution and Coincidence Time Window on Scanner performance

Two scanner parameters which could affect sensitivity were studied: crystal length and crystal energy resolution. The relationship between crystal length and sensitivity was investigated via simulations using crystals with an axial length from 2.0 *cm* to 5.7 *cm*. Furthermore, sensitivity as a function of energy resolution in the range of 10% - 50% was studied. In addition, several values for the lower energy level discriminator (LLD) were simulated with a constant value of 650 *keV* for the higher level energy discriminator. It is well known that the scatter fraction may decrease by increasing the LLD (Carney and Townsend, 2006). Furthermore another factor which can be affects the NEC and under the scope of this section is the coincidence time window. We assessed the effect of LLD and coincidence time window on both NEC and SF.

3.2.8. Impact of the Number of Detector Rings on the Scanner Performance

The dependence of the sensitivity, NEC rate and SF on the number of block detector rings was explored. Variations of the Biograph PET scanner with the same geometry and characteristics but with additional block detector rings (from 3 to 10) were considered. A maximum ring difference of 38 was used for all scanners, except for the B-TP and mCT, for which maximum ring differences of 27 and 49, respectively, were employed. The simulations yield and estimation of the increase in sensitivity and count rate performance obtained with additional detector rings as well as with the increase of maximum ring difference.

3.2.9. Uncertainty estimates

When simulating existing PET systems, uncertainties due to statistical fluctuations can be reduced to a level of insignificance by running the simulation with large enough number of events. In addition, the existing physics models within PENELOPE (Salvat et al., 2008), have been validated against experimental data and are therefore not a significant source of uncertainties. Thus, simulated predictions can be obtained, which are within a few percent of the experimental results of the PET scanners (España et al., 2009). The main source of uncertainty in the simulation is the lack of precise knowledge of every parameter of the real scanners. It may be, for example, that exact information about scanner geometry and every material of the scanner, such as bed, shielding and covers is not fully known. Most often, only general geometry details and some performance results are readily available for commercial scanners. The same applies to the internal electronics and event processing chain. Thus, it is necessary to use simulations flexible enough to include parameters that can be optimized to reproduce the experimental performance results. In the case of the Biograph scanners, we have chosen the following performance measurements to optimize the simulations:

1- Sensitivity. The measured sensitivity values for the B-TPTV scanner were taken as a reference. PeneloPET simulations, which employ the basic geometry definitions for this scanner (radius, block size, crystal dimensions) when assumed no reflector in between crystals, overestimate sensitivity by 12% (see Table 3.4). This could be due to a series of causes, for instance the radius of the actual scanner may be a few percent larger than assumed, crystals may be slightly shorter, or sizeable attenuation of photons in front-covers and bed may be present. Or also, there may be a small amount of reflector in between scintillator crystals. Other authors indeed have chosen to modify the length or shape of the crystals (MacDonald et al., 2008). However, we have chosen to include a reflector thick enough (around 0.4 *mm*) to reproduce the B-TPTV sensitivity. We chose so because there is indication that a reflector is present in between crystals, according to brochures and pictures from the manufacturer of the scanner, and this small size of reflector is still consistent with published values for block and crystal sizes. We make no claim that this result of the simulation implies that there is any amount of reflector in the real system.

2- The measured sensitivity values to which we fitted the simulations include uncertainties of the order of 5%, which mostly originate from the uncertainty on source activities employed in the measurements (Jakoby et al., 2009), and therefore these uncertainties are translated into the sensitivity predictions of the simulations. Other predictions that depend mainly on the geometry of the scanner, such as scatter fraction then bear similar uncertainties. The comparison with measured results for other scanners supports this estimate.

3- Count rate as a function of activity concentration curves. Reproducing the experimental behavior of the system would require very detailed knowledge of the acquisition electronics. As this information is not available, we have taken the trues, randoms and NEC rates as a function of activity concentration curves for the B-TPTV scanner as a reference to tune some of the parameters of the simulation defining the electronics. As it was the case for sensitivity, the 5% uncertainty of the activity of the source employed in the experimental measurements is then translated as uncertainty in the results of the simulation. In order to avoid regions in which additional bottlenecks (such as disk and computer dead-times) in the processing of events by the real scanners may arise, the fit of the simulations was done to data count rates below the peak of the NEC. In this region, the deviations of the tuned simulations from the data of the real B-TPTV system remained below 10%. We thus estimate the deviations of the predictions of the simulations for all other Biograph systems should remain below 10%, for count rates smaller than the NEC peak.

3.3. Results and discussion

3.3.1. Sensitivity

As mentioned before, simulations without crystal reflector would overestimate the experimental sensitivity quoted by (Jakoby et al., 2009) by 12%. This overestimation is also similar to the one reported by Jan *et al*. (Jan et al., 2005) who made a simulation study of ECAT EXACT HR+ clinical PET scanner and found a 10%, overestimation of the sensitivity predicted by the simulations. Also, Schmidtlein *et al*. (Schmidtlein et al., 2006) studied the GE Advance/Discovery PET scanner, and their simulations using GATE overestimated the sensitivity of the real scanner by as much as 20%.

The use of a reflector thickness of the order of 0.4 *mm* yields good agreement with the measured sensitivity at several distances to the axis of the scanner. Indeed, an average sensitivity of 8.2 kcps, both at 0 and 10 *cm* off-center, was obtained with this assumption for reflector thickness, which was subsequently employed in all simulations in this work.

Once this assumption is made, sensitivity of the B-TP and mCT are predicted within 2% of the experimental values. Table 3.4 presents the sensitivity for these systems, as well as for extended axial FOV systems. In general our simulated sensitivities for B-TP and mCT are in good agreement with the measured (Jakoby et al., 2011, 2009) ones.

Table 3.4. Sensitivity results of the PeneloPET simulation as well as measured and the simulated results of different systems

Sensitivity [kcps/MBq] @ 0 and 10 cm off center				
Number of block rings	*Axial FOV (cm)*	*Simulated (this work)*	*Simulated (Eriksson et al., 2007)*	*Experimental*
B-TP	*16.2*	*4.6*	*4.8*	*4.5*
B-TPTV	*21.8*	*w/o reflector 9.2* *with reflector 8.2*	*8.7*	*8.2*
mCT	*21.8*	*9.8*	-	*9.7*
5-rings	*27.2*	*12.5*	-	-
8-rings	*43.6*	*31.7*		-
10-rings	*54.5*	*48.7*	*47.8*	-

In Table 3.4 results for the sensitivity of scanners with 5, 8 and 10 rings are also quoted. The Biograph scanners have been simulated by Eriksson *et al* (Eriksson et al., 2007) using GATE, and thus we can also compare to the results of their simulations. They assumed no reflector and obtained sensitivity for the B-TPTV about 6% larger than the experimental values (Table 3.4) and about 5% smaller than the one we obtain with PeneloPET under similar assumptions. They also predicted sensitivity for the B-TP and for a 10 rings Biograph that are within few percent of the predictions we show here. Thus we can conclude that for sensitivity our simulations are in reasonable agreement with the ones of Eriksson *et al*., within the uncertainties expected.

From Table 3.4 one can also comment on the sensitivity increase for 5, 8 and 10 rings scanners. From 4 (B-TPTV) to 5 rings, the sensitivity would increase a 40%. With 10 rings, which corresponds to an axial FOV of 54 *cm* the sensitivity would increase by a factor 6. This result is similar to that obtained by Eriksson et al. (Eriksson et al., 2007) with GATE. It must be recalled that a maximum ring difference of 38 was employed for these cases, which corresponds to the value used in the B-TPTV scanners. For the simulation of B-TP and mCT, the maximum ring difference was set to 27 and 49, respectively.

It must be recalled that a maximum ring difference of 38 was employed for these cases, which corresponds to the value used in the B-TPTV scanners. For the simulation of B-TP and mCT, the maximum ring difference was set to 27 and 49, respectively.

3.3.2. Scatter Fraction (SF) and Noise Equivalent Count (NEC) Rate

Figures 3.6 and 3.7 and Table 3.5 present the simulated and experimental results for randoms, trues and NEC rates for the B-TPTV scanner. Acquisitions according to the NU 2-2007 protocol for NEC measurement (NEMA, 2007) were simulated with 4.5 ns coincidence time and 425–650 keV energy windows, as for the experimental systems. PeneloPET singles and coincidence dead-times were adjusted to reproduce the experimental random, trues, and NEC curve below the NEC peak.

A NECR peak of 161 kcps at a concentration of 32.5 kBq/ml was fitted to the experimental value of 161 kcps at a concentration of 31.5 kBq/ml (Jakoby et al., 2009). Certainly it would have been possible to match the NEC peak value and position of the simulations more closely to the experimental results if the whole range of data were employed in the fit; however one can see how at high activity concentrations, beyond approximately 33 kBq/ml, the experimental curves show a strong change in slope. This is very likely due to additional dead time losses at high count rates, perhaps associated to bottlenecks in disk data storage and CPU event processing, which are not considered in the simulations. We thus fit the simulations only to data below 33 kBq/ml.

The simulated peak true coincidences rate of 873 kcps appears then at 46 kBq/ml, compared to a measured true peak coincidence rate of 804 kcps at an activity concentration of 38 kBq/ml as seen in Figure 3.6. We consider that this difference between simulated and measured value of the true coincidences is a reasonable indication of the uncertainty in the simulated results for count rates versus activity curves, and it is of similar magnitude than the quoted error of 5% in the experimental activity (Jakoby et al., 2009).

Once these measurements settled the parameters of the acquisition electronics in the simulations, they are employed unchanged for the other scanners analyzed in this work: BTP and mCT scanners and 5, 8 and 10 ring scanners. The differences between the simulated NEC peak values and the experimental ones are less than 3% for both BTP and mCT scanners. For the position of the NEC peak, a difference of 3% is observed for BTP and 14% for the mCT. This may be considered as a measure of the reliability of simulations for these performance figures. The corresponding NEC rate curves are plotted in Figure 3.7, along with the experimental ones.

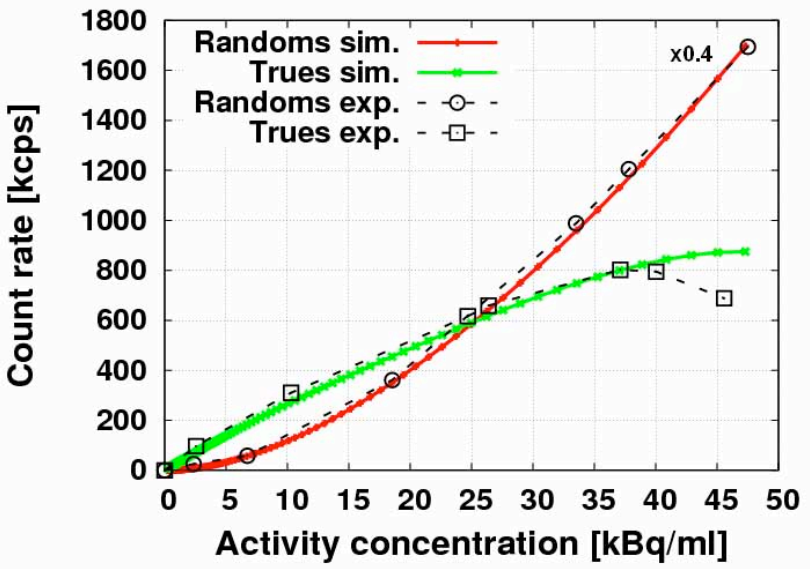

Figure 3.6. Comparison of random and true rate curves as a function of activity concentration predicted by PeneloPET simulations adjusted to the experimental results of the B-TPTV. The random rate curve has been multiplied by 0.4.

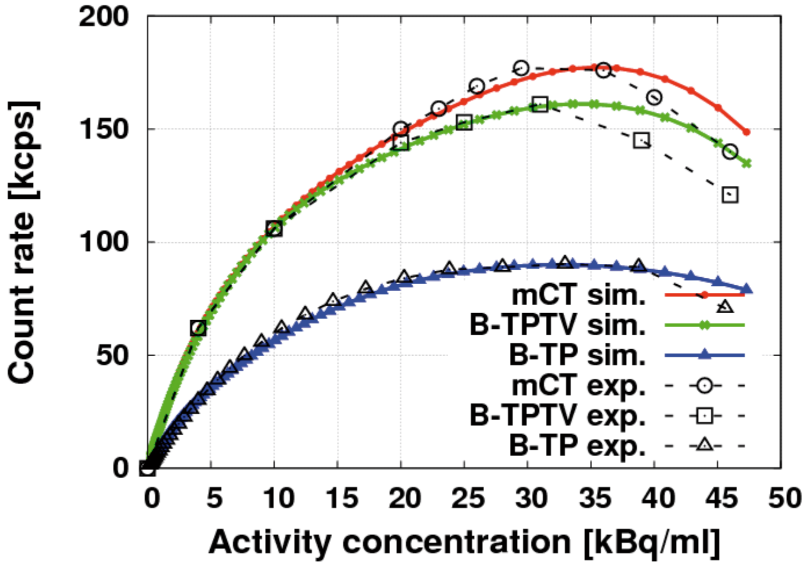

Figure 3.7 Comparison of NEC rate curves as a function of activity concentration of the fit of PeneloPET to the experimental data. All curves have been obtained with coincidence time and energy windows same as in (Jakoby et al., 2009, 2011).

Table 3.5. Summary of values for NEC, and SF for different scanner configurations, according to simulations. In boldface are shown the results that were employed to fix some scanner parameters in the simulations. All results are obtained with a time coincidence window and an energy window same as the measured (Jakoby et al., 2011, 2009).

Number of block rings	*NEC Peak (Kcps) @(kBq/ml)*			*Scatter fraction (%)*		
	Simulated (this work)	*Simulated (Eriksson et al., 2007)*	*Experimental*	*Simulated (this work)*	*Simulated (Eriksson et al., 2007)*	*Experimental*
B-TP	*90 @ 33*	*100@34*	*93@34*	*34.3*	*33*	*32.0*
B-TPTV	***161@32.5***	*177@34*	*161@31.5*	***31.3***	*35*	*32.5*
mCT	*177@34*	*-*	*180.3@29*	*34.8*	*-*	*33.5*
5-rings	*259@39*	*-*	*-*	*30.8*	*-*	*-*
8-rings	*489@35*	*-*	*-*	*32.0*	*-*	*-*
10-rings	*787@30*	*800@31*	*-*	*33.1*	*35*	*-*

The fair agreement with experimental results of the simulated NEC peak for both BTP and mCT scanners gives confidence to predictions of NEC peak values for 5, 8 and 10 rings quoted in Table 3.5. The NEC peak for the 10-ring system is 787 kcps at a concentration of 30 kBq/ml, also in good agreement with the simulated study (800 kcps @ 31 kBq/ml) of Eriksson et al. (Eriksson et al., 2007). As expected, an increase in peak NEC rate can be observed for additional detector rings up to the point that the NEC peak for the 10-ring system is five times larger than for the B-TPTV system. A similar behavior was also observed in simulations employing GATE (Eriksson et al., 2007) and SimSET (Badawi et al., 2000).

Another prediction of simulations that can be compared to experiment is the SF. It is independent on electronics, being influenced only by time and energy windows and scanner and source geometry. The SF is estimated according to the NU 2-2007 protocol. The simulations and the experimental values for SF are within 4% (Table 3.5). One must note that the SF is a genuine prediction of the simulations, as no parameters have been fitted to reproduce it. The scatter fraction remains fairly constant for all the scanners simulated.

Overall, our simulated results for SF and NEC obtained for the B-TP, B-TPTV and mCT PET scanners are in fair agreement with the experimental results (Jakoby et al., 2011, 2009) and with simulations with GATE (Eriksson et al., 2007).

3.3.3. Spatial resolution

The FWHM and FWTM of the reconstructed point source images are reported in Table 3.6 for showing simulated and experimental spatial resolution results of the B-TPTV scanner. For the simulations average spatial resolutions at 1 *cm* and 10 *cm* radial off-center are 4.4 *mm* and 5.3 *mm*, respectively. They are in reasonably agreement with the experimental values of 4.4 ± 0.3 *mm* and 5.0 ± 0.3 *mm* (Jakoby et al., 2009). Other values reflected in Table 3.6 are in general also in agreement with the measurements.

Table 3.6. Simulated and experimental spatial resolution for the B-TPTV scanner. Experimental results bear an uncertainty of ± 0.3 mm (Jakoby et al., 2009)

	FWHM (mm)		*FWTM (mm)*	
	Simulated	*Experiment*	*Simulated*	*Experiment*
		1 cm off center		
Transverse	*4.6*	*4.2*	*8.5*	*8.1*
Axial	*4.2*	*4.5*	*8.4*	*9.2*
Average resolution	*4.4*	*4.4*		
		10 cm off center		
transverse radial	*5.5*	*4.6*	*9.0*	*9.4*
Transverse tangential	*5.6*	*5.0*	*10.2*	*9.4*
Axial	*4.4*	*5.5*	*7.5*	*10.5*
Average resolution	*5.3*	*5.0*		

3.3.4. Time-of-Flight (TOF)

In Figure 3.8 TOF spectra obtained from simulations for a point source located at the center of the scanner is shown. For this centered source a peak appears centered at a ToF of 0 sec, as expected. As it was the case for other quantities related to the acquisition electronics, precise timing properties of every element of the scanner are not openly available. The timing performance of the scanner depends not only on the timing properties of the scintillator but also on the electronics and post processing of events. PeneloPET time stamps the detection events with the arrival time of the photons the each detector. To account for detector or electronics time jitter effects, there is an additional parameter in the input of PeneloPET which provides the standard deviation in *ns* for additional gaussian time jitter added to the time stamp of each event. With no additional time jitter, we obtain a FWHM in the time spectrum of about 53 *ps*, in agreement with what is expected from effective size, due to positron range effects in water, of a ^{18}F source. In order to reproduce the reported TOF resolution of the Biograph scanners (Kadrmas et al., 2009; Lois et al., 2010), of about 550 *ps* FWHM (see Figure 3.8) an additional jitter of 170 *ps* is included in the simulations..

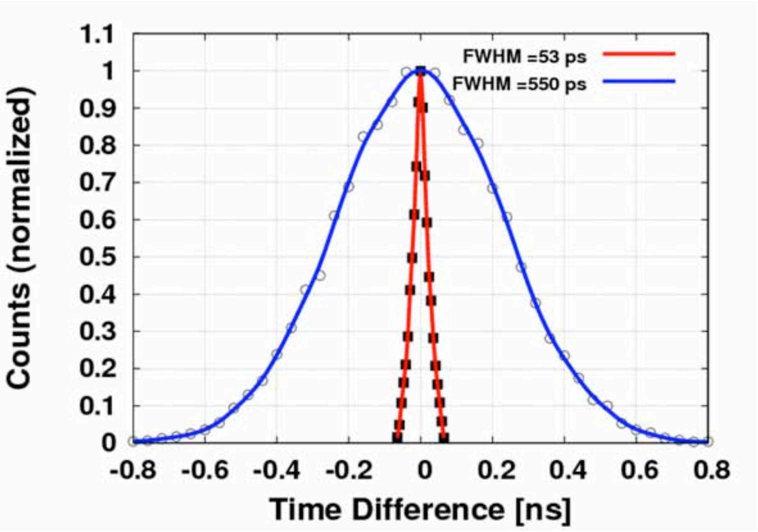

Figure 3.8. Gaussian fit of the simulated TOF distribution from a centered source. And additional time jitter of 170 ps is employed in the simulations to produce a TOF resolution of 550 ps (FWHM) for the B-TPTV scanner.

3.3.5. Impact of the characteristics of the scintillator crystal energy window and coincidence time window on the scanner performance

Crystal length

Crystal length is one of the parameter which induces the percentage of registered coincidence and the sensitivity of the system. In this part we study the relationship between crystal length and sensitivity. According to (Eriksson et al., 2007) increasing the crystal length to 3 *cm* will result in a sensitivity gain of 1.4. The simulations were performed using different crystal lengths (from 2.0 *cm* to 5.7 *cm*) following the NEMA protocol explained earlier.

A thin crystal with high stopping power will help reduce the distance travelled by the photon in the detector and reduce parallax effects. However, a thin crystal reduces the scanner sensitivity. The impact of varying crystal length on system sensitivity is shown in Figure 3.9. Up to a crystal length of 3 *cm*, a linear relationship between sensitivity and crystal length can be observed (black line). Beyond 3 *cm*, the increase of sensitivity seems to approach an asymptotical value. For the performance simulations, the same crystal length of 2 *cm* was used as employed in the actual scanners. With 3 *cm* of crystal, the gain increases by a factor of 1.5, similar to the simulated study of Eriksson *et al.* (Eriksson et al., 2007).

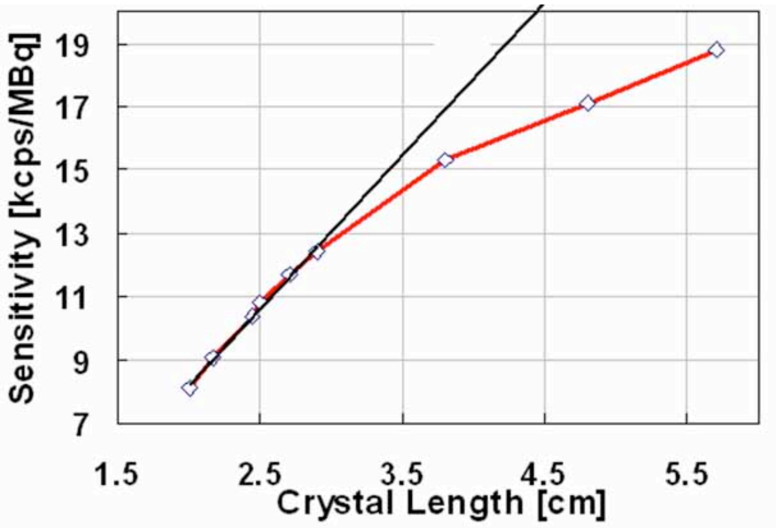

Figure 3.9. Simulated sensitivity of the B-TPTV scanner as a function of the crystal length

Crystal energy resolution

Energy resolution is another factor which affects the sensitivity of the scanner. To achieve good image contrast and to reduce background, its important to have a good energy resolution scintillator (Levin et al., 2006). Here, we assess the impact of different energy resolution (from 10% to 50%) on the sensitivity of the scanner.

The sensitivity as a function of crystal energy resolution is shown in Figure 3.10 for the same energy window of 425 to 650 *keV*. For a given energy window, sensitivity is affected by the energy resolution. It can be observed that beyond an energy resolution of 20%, the sensitivity decreases linearly with increasing energy resolution. For an energy resolution of less than 20%, the sensitivity is barely affected. In our simulations we employed the reported energy resolution for LSO of 11.7% (Jakoby et al., 2008).

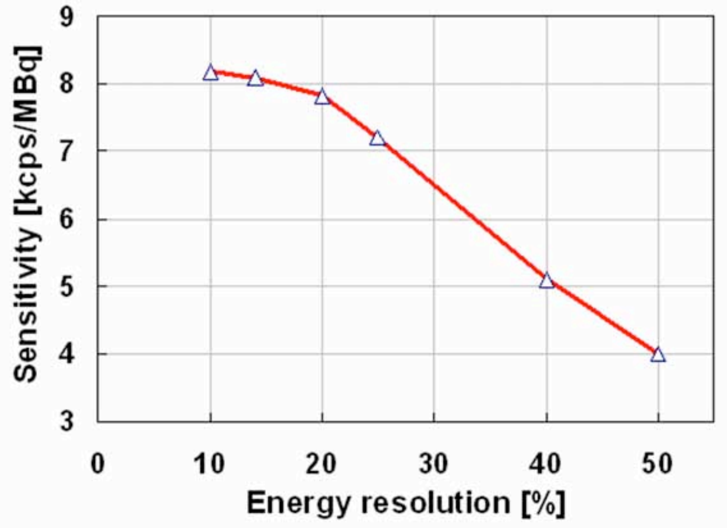

Figure 3.10. Sensitivity of the B-TPTV scanner as a function of energy resolution for a fixed energy window of 425 - 650 keV.

Lower energy level discriminator (LLD)

The scatter fraction in a 3D PET system is controlled by the energy window, especially the LLD setting. It is well known that the scatter fraction may decrease by increasing the LLD (Carney and Townsend, 2006). The closer the LLD is to the 511 *keV* photopeak the better the scatter rejection (Eriksson et al., 2004). How high we can set this without losing good counts depends on the energy resolution of the scintillators. Here we studied NEC and SF as a function of LLD values of (375, 400, 425, 450 and 475 *keV*) and a constant upper level discriminator (ULD) of 650 *keV*.

Table 3.7 presents SF values for different LLDs. As expected, simulations with a wider energy window (375-650 *keV*) result in the highest SF while an LLD of 475 *keV* yields the lowest SF. These results agree with the simulated study of (Eriksson et al., 2007) as narrowing the energy window results in a reduction of SF.

Table 3.7. Simulated values for SF vs LLD for B-TPTV PET scanner

Lower level discriminator (keV)	*Scatter fraction (%)*
375	*53.1*
400	*46.8*
425[a]	*31.3*
475	*23.2*

[a] *default value for the real scanner*

Figure 3.11 shows the resulting peak NEC rate for different LLDs. Less scatter events will be detected if the LLD is raised but raising it too much would also cause a loss of true events. Thus an optimal LLD value exists that maximizes the NEC. Indeed, an LLD of 425 *keV*, as employed in the experimental systems, as it appears to yield the highest peak NEC rate (see Figure 3.11) according to our simulations.

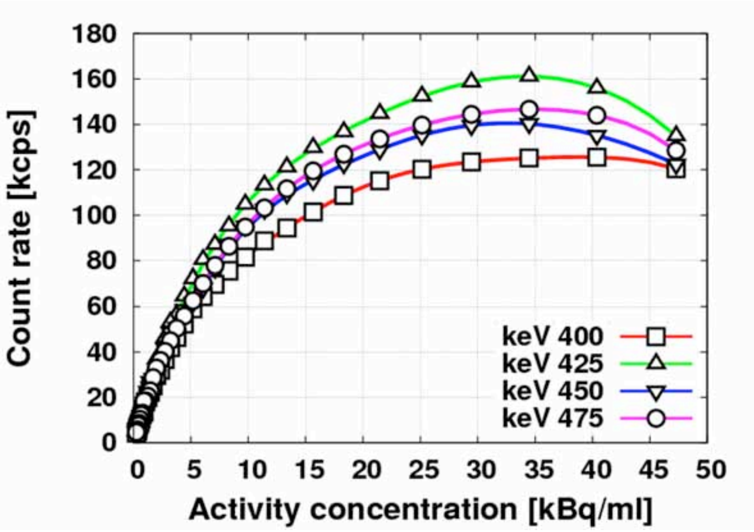

Figure 3.11 NEC rates as a function of the LLD for the B-TPTV scanner.

Coincidence time window

Coincidence events require that both photons from positron annihilation are detected by the system electronics within a certain time window (Cherry et al., 2003). The acquisition electronics has to allow for a coincidence time window large enough to include the actual TOF required for a photon to reach the detector ring. However, a too large coincidence time window may result in an increase of random coincidences. Therefore, the optimal choice of time coincidence window which yielded the maximum NEC was investigated. For this purpose, acquisitions with coincidence time windows of 4, 4.5, 5, 6 and 7 *ns* were considered. Other than for this study, a default 4.5 *ns* coincidence time window was employed for all other simulations in this work.

Using too wide time coincidence windows will cause an increase in random events, and therefore the NEC count rate would decrease. However, a count rate reduction would follow from the use of too narrow coincidence time windows. Thus, again, there would be an optimum value of the time coincidence window. Simulated results of NEC curves for different coincidence time windows are shown in Figure 3.12. 4.5 *ns* yields the highest peak NEC rate. This is the default value employed the for B-TPTV scanner (Jakoby et al., 2009).

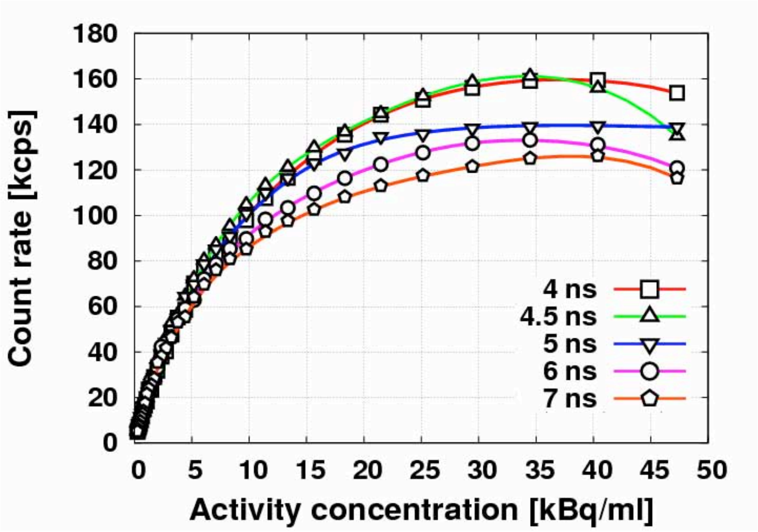

Figure 3.12. NEC curves with different coincidence time windows for the B-TPTV scanner. 4.5 ns optimized the highest value

3.3.6. Simulation speed

The computation time required to obtain PeneloPET simulations of preclinical scanners has been already reported (España et al., 2009). Here we give an indication on the simulation speed for clinical settings, for which the amount of events that are simulated but do not result in recorded coincidences (due to attenuation, smaller sensitivity and scatter outside the smaller energy windows) is much larger. We quote the simulation speed for the setup employed to evaluate the NEC curve for the B-TPTV scanner, both at the peak of the NEC and near the end of the acquisition, with low activity and almost no random counts, that is near the origin in the NEC curve. In a single core of an Intel(R) Xeon(R) CPU E5-2650@2.00GHz it is possible to simulate 256 detected coincidences per wall clock second at the peak of the NEC and about 100 detected coincidences for the smallest activities with negligible fraction of random counts. This is with hyper threading on and no other user tasks running in the computer. The simulation speed for the same case with a total of 16 PeneloPET threads working in the same processor achieves nearly 14 times higher simulation speed, that is, 3500 detected coincidences per second at the NEC peak, 1,400 when there are no random counts detected, always per wall clock second. It is thus possible to obtain more than million counts in a couple of hours in a machine with one eight-core multi-threading processor.

3.4. Summary and conclusion

In this chapter we assessed the capability of PeneloPET to simulate clinical PET/CT systems. For this purpose, performance measurements of the B-TP, B-TPTV and mCT PET/CT scanners (Siemens Medical Solutions USA, Inc.) were simulated and the results compared with experimental data and results of other simulations.

We have shown that PeneloPET is flexible enough to easily accommodate different dead time ingredients in the electronics, which have been optimized so that the experimental NEC curves for the B-TPTV could be reproduced. Once the simulation was set to reproduce the sensitivity of the B-TPTV scanner, predictions for scatter fraction derived from the simulation (Tables 3.4 – 3.5), agree within 5% with the measured values for the three scanners under investigation. Furthermore, the sensitivity and NEC rate curves for both the B-TP and mCT are also reasonably predicted, after fixing parameters of the simulations to the B-TPTV experimental rate curves. The simulated and experimental spatial resolution results were also comparable (Table 3.6). These performance results validate the use of PeneloPET to simulate the clinical scanners. Therefore, simulations were employed to investigate the variation of several basic scanner parameters on the performance of the B-TPTV system. For example, Figure 3.9 – 3.10 shows an inverse relationship between crystal energy resolution and sensitivity, for a given energy window. Furthermore, the impact of the energy window on the system sensitivity was explored, as well as the effect on the peak NEC values and SFs. Simulations allowed the identification optimal choices of coincidence time and energy windows. For the B-TPTV, the simulations confirmed that the default factory values of a 425 to 650 *keV* energy window and a 4.5 *ns* coincidence time window are the best choices.

The sensitivity of the PET system can be increased by adding more detector rings and also by increasing the maximum accepted ring difference. The good agreement of the simulations with the measurements on existing scanners, allow us to make reliable predictions for scanners with larger number of rings or larger ring difference. The extended ring difference of the mCT PET scanner leads to a 19% increase in sensitivity compared to the B-TPTV scanner. The larger ring difference of the mCT also leads to a 10% increase of the peak NEC, compared to the B-TPTV (Table 3.5). These results are in agreement with previous simulation done with GATE (Eriksson et al., 2007) or with SimSET (MacDonald et al., 2008). We have shown that PeneloPET is capable of easily incorporating TOF properties of the scanners in the simulation. This is of paramount importance to describe modern clinical PET systems.

In conclusion, we have shown that PeneloPET is suitable for simulating and investigating clinical systems. The Biograph TruePoint, TruePoint with TrueV and mCT PET/CT systems were simulated successfully in all aspects.

4. Image reconstruction

4.1. Introduction

In positron emission tomography, images are obtained using tomographic reconstruction methods from the measured projections of the object or the patient examined. As it was mentioned earlier in chapter two, PET images are usually reconstructed either analytically by algorithms like FBP or iteratively by algorithms like OSEM. Despite their high computational cost, iterative image reconstruction methods techniques are becoming more and more popular, as they can produce images of better contrast and signal-to-noise ratio (SNR) than the conventional FBP (Barrett et al., 1999; Riddell et al., 2001; Schiepers et al., 1997).

In general, iterative reconstruction algorithms require two major steps, projection and back-projection. These two steps are repeated until a satisfactory image is obtained. This iterative process is time-consuming and it has been a major bottle-neck of these algorithms. One important advance that allowed the adoption of these methods was the appearance of algorithms like OSEM, in which image updates are made using just part of the data in each iteration. This way, the number of operations and the computational cost of each image update is considerably reduced. Additionally, the improvement in speed and memory of modern computers, as well as the possibility of using several processors in parallel also reduced the computational time required to reconstruct iteratively an image. In recent years, there have been several attempts to speed-up the reconstruction even more by using Graphics Processing Units (GPUs) (Herraiz et al., 2011).

GPUs have been proposed for many years as potential accelerators in complex scientific problems (*General-Purpose Computing on Graphics Processing Units repository*, 2010) like image reconstruction, with large amount of data and high arithmetic intensity. Indeed, tomographic reconstruction codes are suitable for massive parallelization, as the forward and backward projection can be organized as single instruction multiple data (SIMD) tasks and distributed among the available processising units by assigning part of the data to each unit (Hong et al., 2007; Jones and Yao, 2004).

In this thesis, image iterative reconstructions were performed with the code developed in our group, GFIRST (Herraiz et al., 2011) (see section 4.1), implemented in CUDA (Compute Unified Device Architecture NVIDIA CUDA Programming Guide v.2.5.0).

GFIRST is an adaptation of FIRST ("Fast Iterative Reconstruction Software for (PET) tomography") (Herraiz et al., 2006) also developed in our group. Additional improvements in the code have been implemented for this work, such as additional regularizations, PSF modeling and the possibility of using TOF information.

Although TOF-PET was proposed and tested already at the early use of PET (Moses and Derenzo, 1999), it received little attention for many years, mainly because the fast scintillators required for TOF which were available at the early times provided very low sensitivity. In the last few years, interest was revived by the introduction of new scintillators such as LSO, with an attractive combination of properties (Kuhn et al., 2004; Moses and Derenzo, 1999; Moszynski et al., 2006; Surti et al., 2003), including fast timing characteristics, good stopping power, and high light output.

With higher timing precision, PET systems can measure the TOF difference between two coincident annihilation photons with enough precision to be able to constrain the estimated location of the positron annihilation along the LOR. When the TOF information is included in the image reconstruction process, it can improve the image quality and the accuracy of the quantification, improving lesion detectability (Surti and Karp, 2009; Surti et al., 2006).

Therefore, there is a high interest in TOF-PET because of the significant potential performance improvements that could be obtained compared to conventional PET, as it has been already shown in simulated data (Harrison et al., 2005; Surti et al., 2006) and experimental measurements on TOF scanners.(Conti et al., 2005; El Fakhri et al., 2011; Lois et al., 2010; Muzic and Kolthammer, 2006; Surti et al., 2007; Watson, 2006)

Most often TOF data are organized into sinograms, each event in the TOF data is assigned to a specific sinogram depending on the TOF for that event. There is, therefore, a complete set of 3D sinograms for each TOF bin. This timing information is then taken into account during the fully 3D reconstruction of the data. The image obtained incorporating the timing information can be directly compared with the image reconstructed without timing information, and the improvement in SNR can be assessed.

In this chapter we present image reconstruction with GFIRST from data with and without TOF information, for the clinical PET-CT scanner Biograph True-Point with TrueV (B-TPTV) simulated in the previous chapter. Therefore, the goals of this part of the thesis were to demonstrate that GFIRST code can incorporate TOF information, and to investigate the gain in image quality that can be achieved using TOF in different situations, with the help of realistic simulations. The quality of the reconstructed images have been estimated by measuring the image SNR and contrast in hot lesions (spheres <15 mm), as well as by the noise in the background, both with and without TOF.

The chapter is organized as follows: section 4.1 presents the description of GFIRST. Methods and materials follow in next section (4.2), which includes a description of the image quality phantom used, the details of the FBP reconstruction, and the normalization, gap-filling, and attenuation corrections. We also describe in this section the modifications implemented in GFIRST during this thesis work, like the use of a PSF, regularization by a median filter and the use of TOF. Section 4.3 presents the main results, comparing SNR, contrast and noise of the images obtained in different cases. Finally, the conclusions are in Section 4.4.

4.2. GFIRST: GPU-Based Fast Iterative Reconstruction of Fully 3-D PET Sinograms

GFIRST (Herraiz et al., 2011) is an adaptation of FIRST (Herraiz et al., 2006), developed in our group. The main goal of GFIRST was to obtain a significant acceleration of the algorithm without compromising the quality of the reconstructed images, and with speed-ups large enough to compete with the reconstruction times obtained in a cluster of CPUs. The code is a rather straight-forward implementation of the MLEM algorithm, avoiding whenever possible clumsy GPU-specific coding, allowing edition and modifications with no significant effort nor deep knowledge of CUDA and GPU programming. Besides, the GPU code is as similar as possible to the CPU code, what makes it easier to handle and debug it. Indeed, approximations in the forward and backward projection kernels were avoided and the same system response matrix (SRM) as in the original CPU code was used, in order to avoid a loss of accuracy or artifacts in the final images. However, use of memory is optimized and the acceleration obtained is very noticeable.

Unlike some previously proposed reconstruction codes implemented in the GPU (Pratx et al., 2009; Reader et al., 2002), which used list mode data, GFIRST was designed to work with sinograms (Fahey, 2002). Although list-mode data, for which all the relevant information from each detected coincidence is stored, might provide optimal images, sinogram data organization also has some interesting features and advantages. Sinograms are commonly used in most of the current commercial scanners (Fahey, 2002), and they are often easily available to the user. Usually, their size is smaller than list mode files, so they are easier to handle and store. Furthermore, in a sinogram, data are spatially ordered and can thus be accessed in a simple and ordered way. This allows for very fast backward projection implementations. Finally, under certain approximations imposed by the sinogram, the simulated system exhibits many symmetries, thus reducing the size of the SRM.

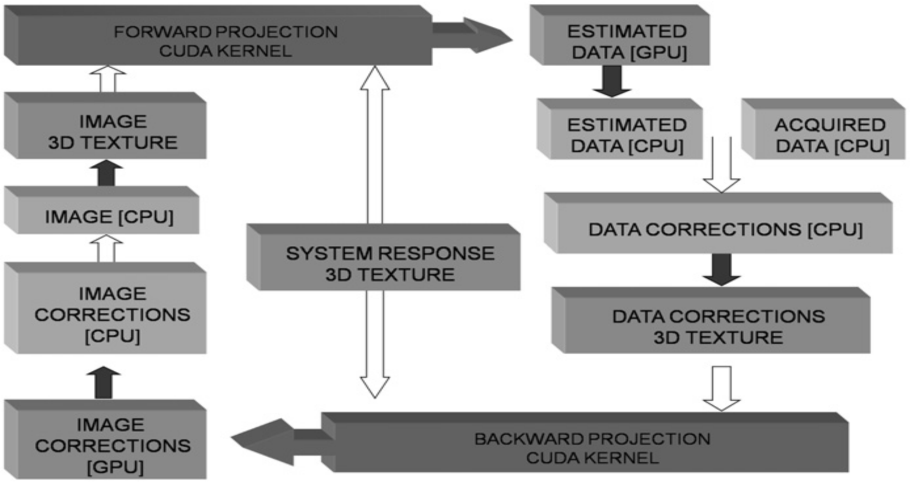

Figure 4.1. Flowchart of the implementation of the code in the GPU (Herraiz et al., 2011).

GFIRST was implemented in CUDA, an application programming interface (API), which allows writing programs in C or Fortran language with extensions to execute part of them (CUDA kernels) on the GPU. Since forward and backward projections take up most of the reconstruction time, only these two steps are implemented as CUDA kernels called from the main reconstruction a Fortran code, running in the CPU. Figure 4.1 shows the data flow between CPU and GPU.

Due to the large number of threads that can be executed in parallel on GPUs, the usual bottlenecks of these implementations are memory access. GFIRST uses texture memory, a kind of global memory available in the GPU that is allocated and indexed for fast access (Sanders and Kandrot, 2010).

As shown in Figure 4.1, three 3-D textures are defined in GFIRST: one for the image being reconstructed, another for the SRM, and a third corresponding to the corrections obtained after comparing measured and estimated data. The SRM is uploaded into GPU global memory as a 3-D array and then attached to a 3-D texture at the start of the program. Further information about GFIRST implementation can be found in (Herraiz et al., 2011).

In order to control noise artifacts and drive the image estimate sequence toward a smoother convergence, several methods have been used to regularize the image updating mechanism in GFIRST. One of the methods of controlling noise in the images reconstructed is to add a smoothing step between iterations. In this work we apply a smoothing step by either convolution with a Gaussian or by applying a median filter (see section 4.3.9).

4.3. Methods and materials

The scanner employed for the simulation was the Biograph TPTV PET/CT (Jakoby et al., 2009). The TOF resolution of this system for a point source in air is 550 ps. Data was simulated with PeneloPET as described in the previous chapter and then rebinned into both non-TOF and TOF sinograms. Sinograms consisted of 336 x 336 x 559 bins (angualar, radial and sinogram planes respectively) for the non-TOF case, as well as for each temporal bin in the TOF case. TOF sinograms organization is described later in this chapter.

4.3.1. Image quality phantom

The NEMA image quality phantom (Figure 4.2) of 23 cm in diameter was used for all the simulations of this chapter. The four smallest spheres (diameters of 10, 13, 17, and 22 mm) were filled with ^{18}F at an activity concentration eight times higher than the background (5.3 kBq/cc as background and 42.4 kBq/cc for each small sphere). The two largest spheres, of 28 mm and 37 mm respectively, were filled with non-radioactive water and the central lung insert was filled with air. List-mode acquisitions were simulated with different number of counts to study the image quality with different levels of noise. The reconstructions, with and without TOF, were performed with 5 iterations of 5 subsets each. The image matrix size was 336 × 336 × 109 voxels (voxels size is 2mm). Lesion SNR, contrast and noise were studied as a function of iteration number for the small spheres (<15 *mm*)

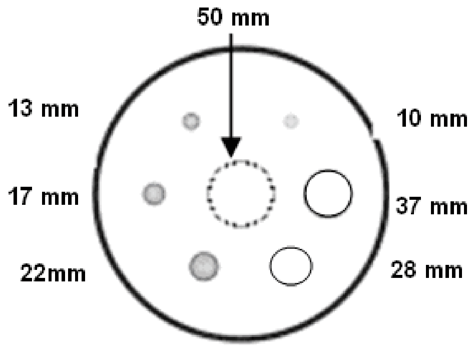

Figure 4.2. Drawing of the phantom with hot and cold spheres and the central lung insert with no activity (NEMA, 2007).

4.3.2. Organization of the TOF 3D PET data

The output data in list-mode provided by PeneloPET, is a large binary file that includes for each coincidence event, the information regarding the coincidence type, the TOF and the coordinates of the event required to assign it to a sinogram bin. We developed a code using ROOT[5], to read this information from the list-mode data and using the same procedure as the one implemented in PeneloPET based on Michelograms (described in chapter 2), we can produce the sinograms with and without TOF.

4.3.3. Sinograms

In PeneloPET, the sinograms corresponding to different combinations of rings in which each of the gamma ray has been detected are grouped together using Michelograms as described earlier in chapter 2. Here, *span* refers to axial compression, while *segment* denotes the group of sinograms that have been assumed to have similar ring differences. The span number represents the ring difference between two adjacent segments. The sinogram is stored as a continuous file, starting from segment 0 (direct sinograms), and then continuing to segment +1, segment -1… until segment -3. Thus the corresponding tilting angle can be calculated by:

$$\text{[illegible]} \; \frac{span \times zpitch}{R_{det} + D} \qquad (4.1)$$

where *span* is the span of the Michelogram, *Zpitch* is the pitch in the *z* direction, R_{det} is the radius of the crystal ring, and *D* is the depth-of-interaction.

The Biograph TPTV PET scanner uses 55 rings with a maximum ring difference of 38 and up to 7 segments, using a span of 11. Therefore, the sinogram has 109 and 559 direct and indirect planes respectively. Figure 4.3 illustrates the Michelogram for this scanner as

---

[5] http://root.cern.ch/drupal/

obtained from PeneloPET. Each line in this figure represents a sinogram.

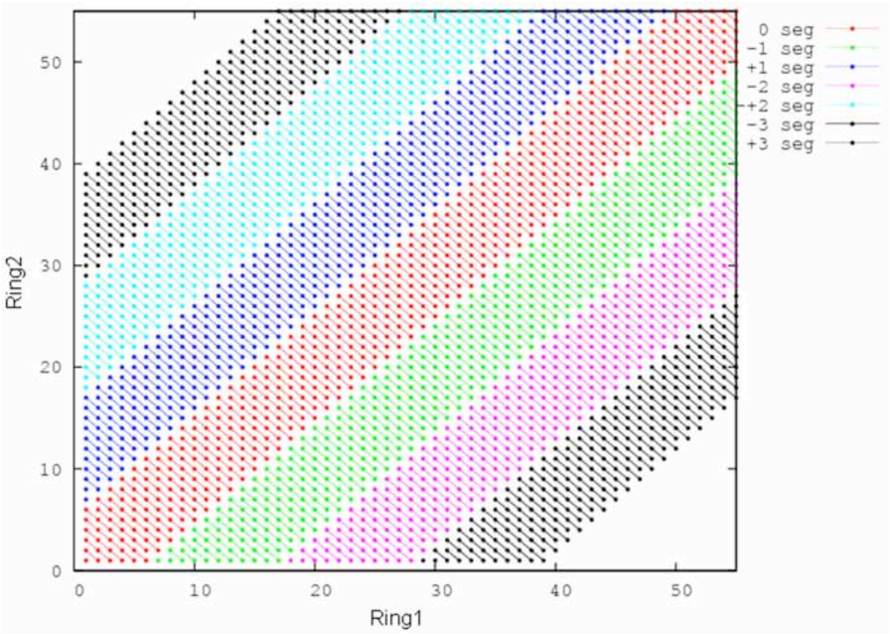

Figure 4.3. Michelogram of the Biograph TPTV scanner with span 11 and 7 segments.

4.3.3.1. TOF sinogram

The TOF information encoded in the list-mode data in the commercial Biograph PET-CT scanner uses 78 *ps* time bins. The data is later reorganized into sinograms with 312 *ps* time bins: Four bins of 78 *ps* are added to form the 312 *ps* bins. Figure 4.4 illustrates this time alignment and TOF sinograms (from -1 to +1).

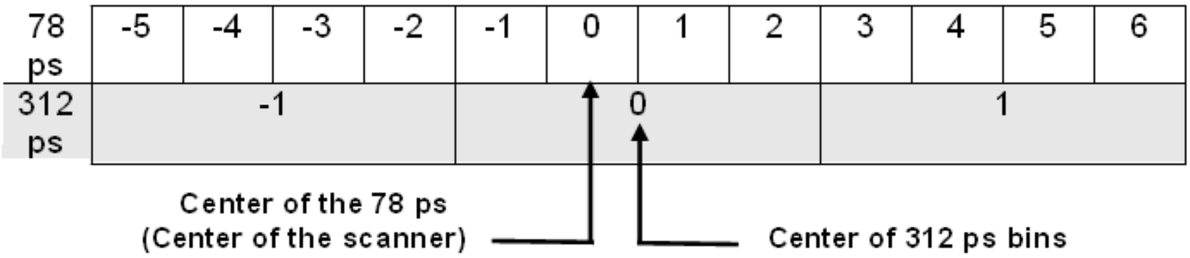

Figure 4.4. Time alignment used in this thesis, as suggested by Siemens

After reorganization of the data into sinograms with 312 *ps* time bins, data can be further assigned to conventional sinograms or TOF sinograms.

In our case, working with simulations, we have used a similar criterium. We used a TOF sinogram with 13 TOF bins (each 312 *ps* wide) covering a total of 4.056 *ns* coincidence time window. Figure 4.5 shows an example of the 2D sinograms for different TOF bins (from -3 to +3) obtained with the image quality phantom.

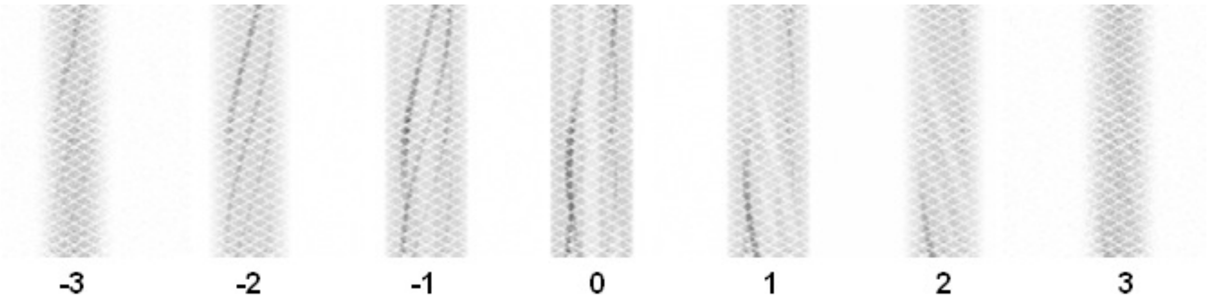

Figure 4.5. Sinograms of the NEMA image quality phantom (TOF bins from -3 to +3, each 312 ps wide).

4.3.4. FBP reconstruction

The analytical reconstruction algorithm FBP is the standard way to obtain an image from a 2D sinogram (Brooks and Di Chiro, 1976). It is based on the central (or Fourier) slice theorem which relates the frequencies of the image in a particular direction with the frequencies of its projections (Defrise et al., 2005; Khalil, 2010; Phelps, 2006). It is a fast and linear method, which provides a standard reconstruction procedure. On the other hand, it also has the limitation of assuming an ideal emission and detection of the radiation, as well as Gaussian noise in the data. Although these assumptions are valid to a large extent in CT, they are not so realistic in PET. This is the reason why iterative algorithms, which overcome these limitations, have been more popular in PET than in CT.

The FBP algorithm is simple. First, it applies 1D convolutions with a specific high pass filter to the radial distribution of each angle (Cho et al., 1974) and then performs the back-projection of the filtered projections to a common image plane.

In this thesis, we developed a FBP reconstruction program which has been used to evaluate different results of this thesis. The program was implemented in MATLAB based on the *iradon.m* function provided in the Image Processing Toolbox of MATLAB.

4.3.5. Normalization

In order to obtain good reconstructed images, we have to include the normalization corrections in the reconstruction algorithms. This normalization takes into account the differences in the sensitivities of different bins of the sinogram. In Chapter 2 we explained methods used for normalization. In this thesis, the normalization factors were computed using a simulation of a uniform cylindrical phantom source of ^{18}F covering the entire FOV of the Biograph scanner. Figure 4.6 shows the uniform phantom at the middle of the scanner and one of the transverse 2D sinograms obtained. Comparisons of normalized and non-normalized sinograms are shown in Figure 4.7.

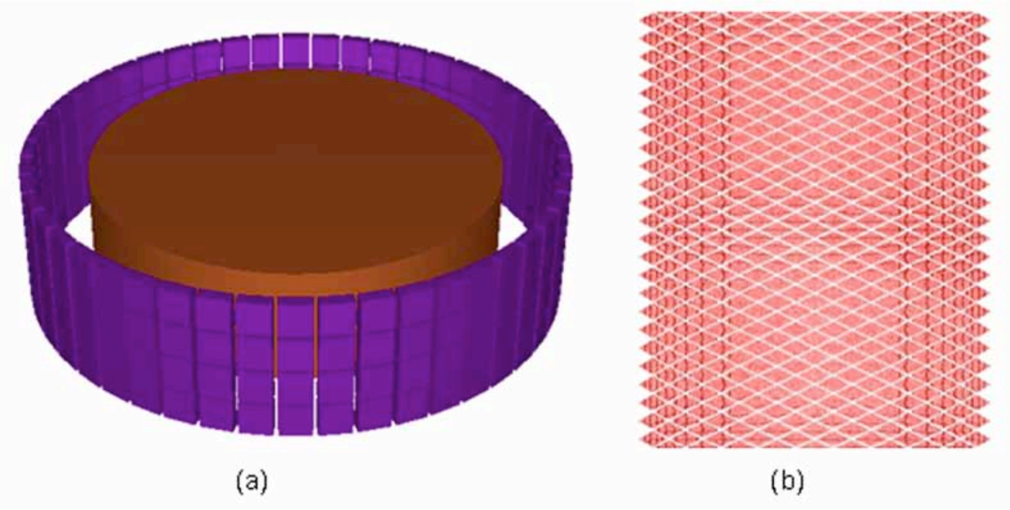

Figure 4.6. Simulation of uniform phantom (normalization phantom) at the center of the PET scanner FOV (a); and simulated sinogram obtained (b).

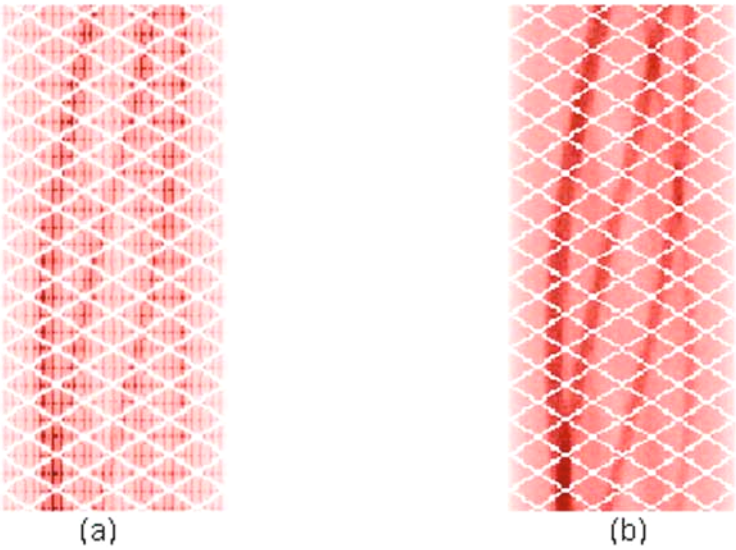

Figure 4.7. Image quality phantom sinograms; Before normalization (a) and after normalization (b)

4.3.6. Gap filling

It is important to take into account that the Biograph TPTV PET-CT scanner has 1 crystal gap between detector blocks in the same plane, and 1 crystal gap between detector blocks in the axial direction. As a consequence, the bins in the sinogram connected with these gaps do not have any count. This is clearly illustrated in Figure 4.7. As analytical methods like FBP assume complete sampling in all projections, large artifacts are created in the images if these gaps are not filled before the reconstruction.

Different methods have been proposed to fill the gaps in the sinogram (Herraiz et al., 2008; Karp et al., 1988; Tuna et al., 2010). In this thesis, we used an inpaint method for gap-filling using the library "inpaint-Nans" implemented in Matlab[6]. This tool is meant to fill holes represented with NaNs (Not a Number) in an image.

The gap-filling procedure uses a mask (Figure 4.8b) created from the normalization acquisition. As in that case, the source is large enough to activate all the sinogram bins, those bins without counts in the normalization sinogram are considered gaps, and the value of these bins in any other acquired sinogram is set to NaN.

The gap-filling process interpolates the missing data using the values around the gaps. In other words, the algorithm looks for NaN elements in the sinogram and performs a smooth interpolation to fill those elements (see Figure 4.8). A comparison of image reconstruction with and without normalization and gap-filling, as well as a profile through the images is shown in Figures 4.9 and 4.10 respectively. Clear visual and quantitative improvements are obtained with the gap-filling method.

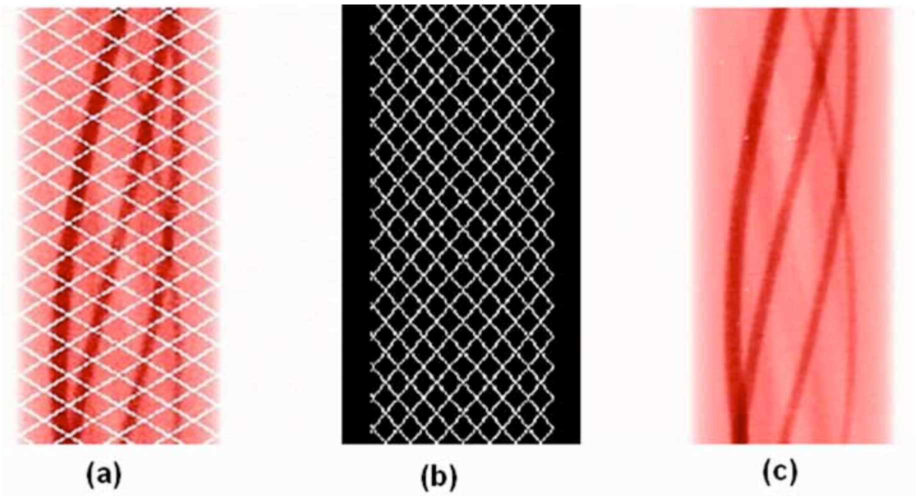

Figure 4.8. Example of a Normalized 2D sinogram with gaps (a); Mask used to define the gaps (b) and gap-filled sinogram (c).

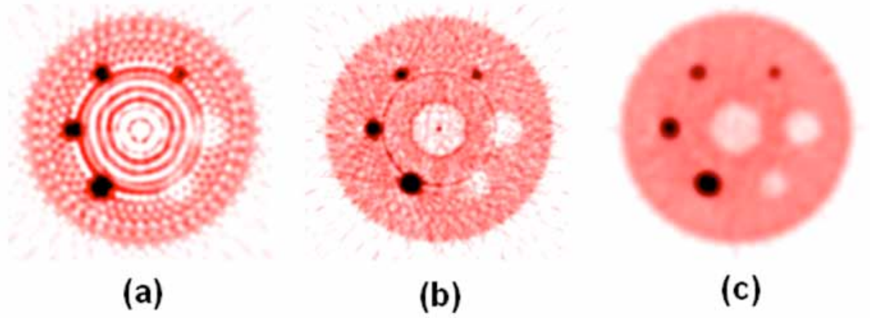

Figure 4.9. FBP reconstruction of the image quality phantom: without normalization (a), with normalization (b) and with normalization and gap filling (c).

---

[6] http://www.mathworks.com/matlabcentral/fileexchange/4551-inpaintnans/content/Inpaint_nans/inpaint_nans.m

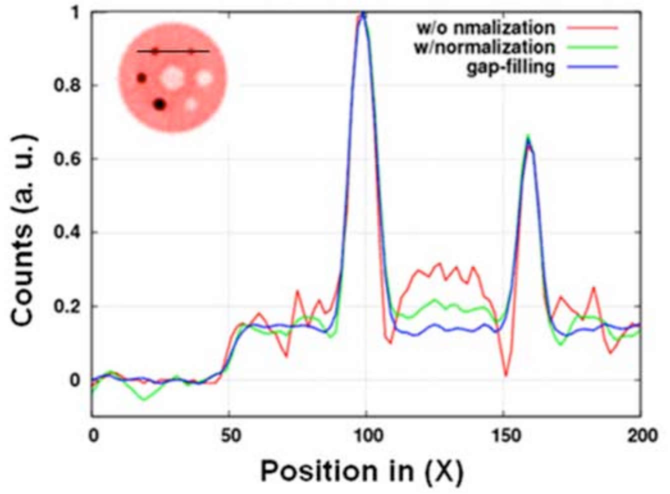

Figure 4.10. Radial profile of the small spheres of the image quality phantom

4.3.7. Attenuation correction

As we described in Chapter 2, the transmission of photons through any material can be characterized by a linear attenuation coefficient which depends on the photon energy and the atomic number of the material.

The information of the attenuation of the annihilation gamma-rays through the patient or the phantom can be derived from a CT scan. In this thesis we used a MATLAB code to create the water-filed cylinder (Figure 4.11) that represents the object present in the PeneloPET simulations. The values of the cylinder represent the attenuation coefficients in water for gamma rays with energy of 511 *keV*. We then used the projection of this phantom and to obtain the total linear attenuation in each sinogram bin, as it is shown in Figure 4.11. The final attenuation map is obtained as the exponential of the total linear attenuation. The significant improvement of images reconstructed with attenuation correction is shown in Figure 4.12. The profile of the largest sphere (22 mm) also demonstrated visually the improvement (Figure 4.13).

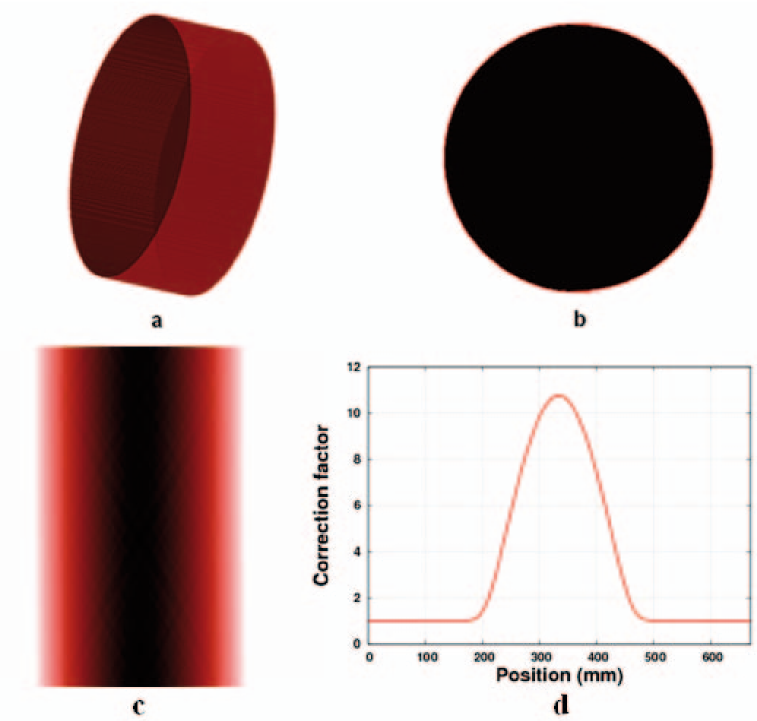

Figure 4.11. CT-based attenuation correction of PET emission data: attenuated cylinder (a), CT image (b), sinogram of the attenuation map obtained from the CT image (c) and profile of the sinogram (d).

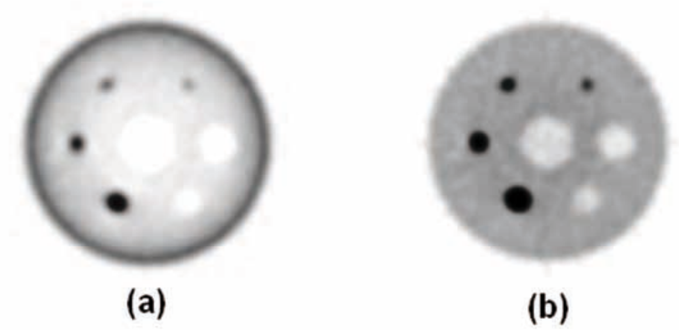

Figure. 4.12. Comparison of images reconstructed without (a) and with (b) attenuation correction.

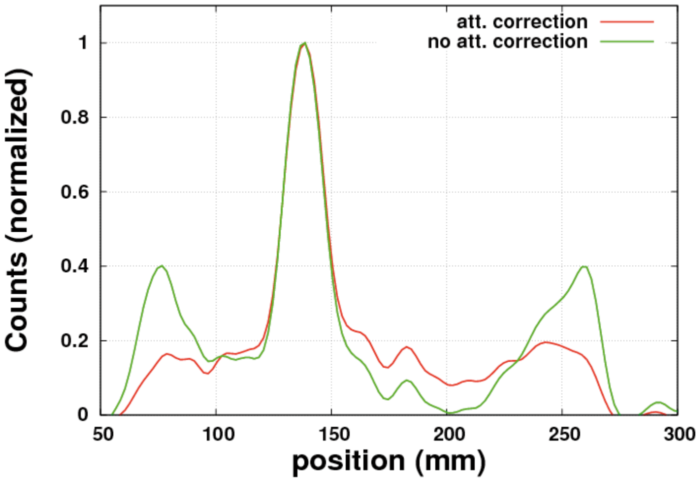

Figure. 4.13. Radial profile along the largest sphere of the reconstructed images with (red) and without (green) attenuation correction.

4.3.8. Resolution recovery with a PSF

Blurring effects in PET such as positron-range, non-collinearity of the gamma rays, inter-detector scatter and crystal-size, among others, limit the maximum resolution achievable in reconstructed PET images.

The blurring caused by these effects is not recovered when standard analytical methods like FBP are used, yielding images with suboptimal resolution. Although it is possible to apply some deconvolution methods to the sinograms before FBP is used (Herraiz et al., 2006) to enhance resolution, iterative methods are a more natural and flexible way to incorporate these resolution recovery methods in the reconstruction process.

There are several ways to implement resolution recovery methods in a iterative tomographic reconstruction algorithm. In FIRST (Herraiz et al., 2006), this was obtained by a detailed modelling of the System Response Matrix (SRM), which contains the probability coefficients of the detecting a pair of gamma-rays in a LOR coming from a decay in a particular voxel. This realistic modelling allows for realistic forward-projection. The algorithm seeks for the image that, after being projected and blurred by all these effects, provides the projections that are statistically most compatible with the data acquired.

As the modelling and storage of the SRM is challenging (Herraiz et al., 2006), many authors have used instead a Point Spread Function (PSF) (Bettinardi et al., 2011; Cui et al., 2011; Tong et al., 2010) that incorporates blurring effects in the reconstruction. The PSF is applied by a convolution in the image domain, which reduces significantly the computational cost of including the blurring effects in the reconstruction process. Although the use of the PSF is an approximation of the SRM, it represents an effective and practical way to take into account these effects.

The PSF can be modelled with different levels of detail. It may be modelled with a simple and unique gaussian, but it may be also constructed such that it depends on the position in the FOV, it may be anisotropic, or even non-symmetric (Fu and Qi, 2008; Herraiz et al., 2007; Tong et al., 2010). In this work, as we are primary interested in the study of TOF, a unique Gaussian PSF has been used along all the FOV.

In order to improve the reconstruction method and increase the convergence rate of the algorithm, an unmatched forward/backward projector pair was used. This method was initially proposed by (Zeng and Gullberg, 2000) to increase the convergence rate of the algorithm. Figure 4.14 shows the flowchart implementation of PSF in GFIRST.

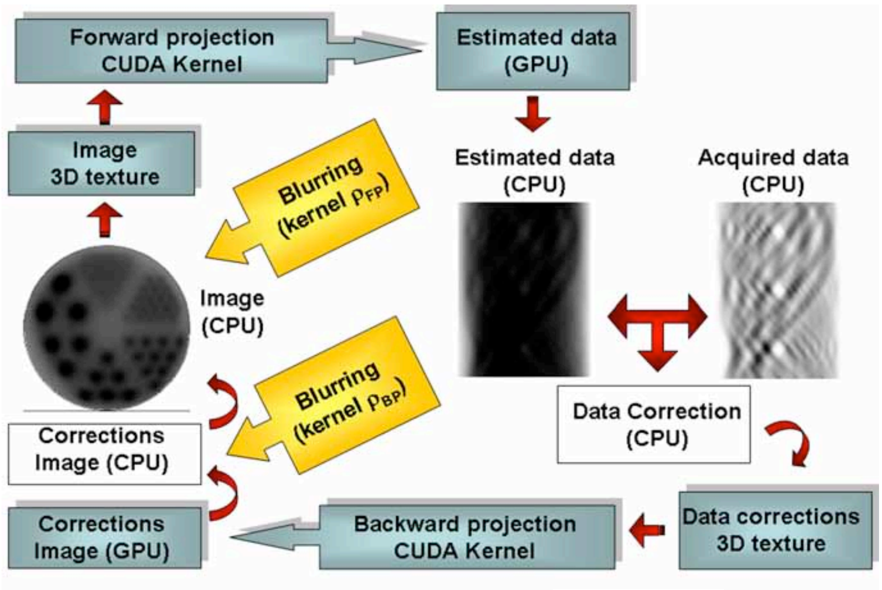

Figure 4.14. Flowchart of the implementation of RR-GFIRST code (Vicente, 2012).

We have studied the optimal width for the PSF as the value that provides the images with the highest contrast as a function of noise for non-TOF images. This width has been then used in all the reconstructions of this thesis.

We evaluated several values of the FWHM of the Gaussian PSF to be used in this work (see Figure 4.15), being the values measured in mm.

It can be seen in Figure 4.15, that larger values of the PSF in the forward projection (PSF 2 and 4) yield higher contrast and larger values of the PSF in the backward projection (PSF 1 and 3) yield smoother images but with slower convergence (i.e. the same level of contrast is obtained with higher number of iterations). This means that with a larger PSF in the backward projection it can take several iterations more to reach the maximum, or at least a near-maximum value, of the objective function (likelihood).

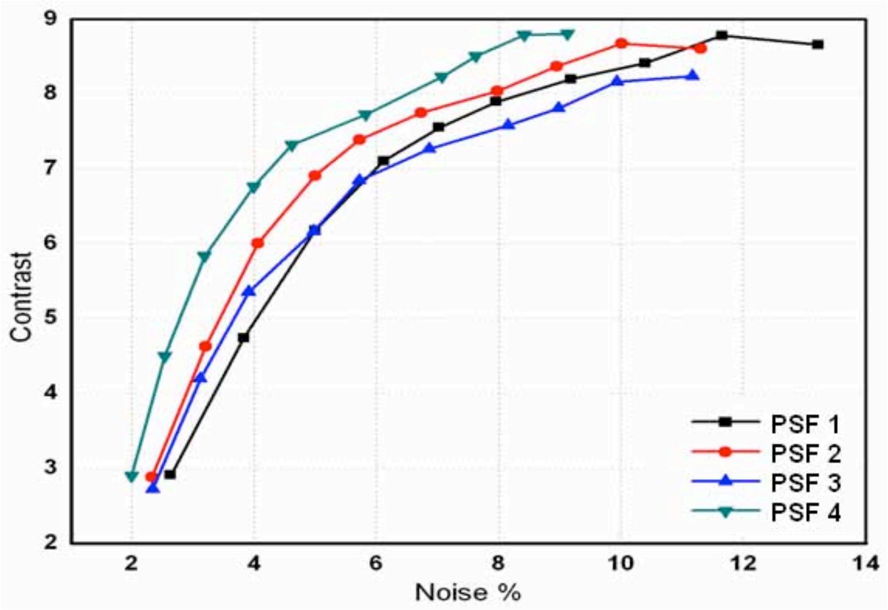

Figure 4.15. Contrast and noise in the image quality phantom (using as reference the 17-mm spheres) for different number of iterations using different PSF values. Each point corresponds to one iteration.

4.3.9. Regularization with a median filter

One of the important problems of iterative reconstruction methods is that when the number of iterations is large, the images become too noisy. This is a well-known problem, and several solutions have been proposed in the literature. First, the total number of iterations can be reduced, limiting the noise in the images. In this case, the problem consists on how to define the optimal number of iterations. Different stopping rules have been proposed (Gaitanis et al., 2010), but as the convergence rate may differ in different regions of the image, the optimal value could not be the same for the whole FOV. Other approach proposed is to reconstruct the images with a large number of iterations to ensure that all regions have converged, and then apply a post-reconstruction smoothing of the image to reduce the noise (Nuyts and Fessler, 2002). The main drawback of this approach is its long computational cost. A different approach was to modify the reconstruction algorithm imposing some constraints in the level of smoothing of the reconstructed images. The family of these new regularized algorithms is usually known as Maximum-A-Posteriori (MAP) reconstruction algorithms. One relatively straightforward way to modify the OSEM algorithm to incorporate the MAP methods, is by means of the One-Step Late (OSL) method (Green, 1990). In this case, after every iteration, the image is smoothed by applying a penalization to those voxels which deviates significantly from their neighbours. This is the method used in this thesis, using the median value of the neighbourhood of each pixel as a reference value.

In this thesis we extended the code to include the one-step-late approached proposed by (Green, 1990), using the median filter regularization. This method efficiently removes noisy patterns in the reconstructed images without blurring the locally monotonic structures (Schiepers et al., 1997).

Similarly to the mean filter, the median filter considers each pixel in the image and looks at its nearby neighbors to decide whether or not its value may be representative of its surroundings. Instead of simply replacing the pixel value with the mean of neighboring pixel values, it replaces it with the median of those values. The median is calculated by first sorting all the pixel values from the surrounding neighborhood into numerical order and then replacing the pixel being considered with the middle pixel value. If the neighborhood under consideration contains an even number of pixels, the average of the two middle pixel values is used.

Using the median filter has two main advantages over other filters like the mean filter. First, the median is more robust than the mean respect to outliers, as a single unrepresentative pixel in a neighborhood will not affect the median value significantly. Second, since the median value must actually be the value of one of the pixels in the neighborhood, the median filter does not create new unrealistic pixel values when the filter straddles an edge. For this reason the median filter is much better at preserving sharp edges than the mean filter.

4.3.10. Incorporation of TOF information in GFIRST

As described earlier in Chapter 2, including the TOF information in the image reconstruction can improve the image quality and the quantitative accuracy, thereby improving lesion delectability (Surti and Karp, 2009; Surti et al., 2006). Here, we extended GFIRST to incorporate TOF information, as GFIRST was initially developed for non-TOF sinogram reconstruction (Herraiz et al., 2011). The code was adapted to include the TOF kernel, which only involved minor modifications, as GFIRST was designed to be flexible and easily modified. Figure 4.16 shows images reconstructed iteratively, (after 1 iteration of 5 subsets) and a profile thought the images along the 10 and 13 mm spheres of the image quality phantom, with and without TOF information. The improvement in image quality with TOF information is clear.

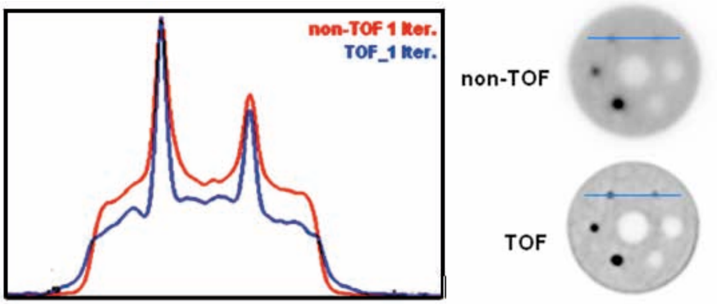

Figure 4.16: Profile of images reconstructed with and without TOF for 10 and 13 mm spheres after one iteration

4.4. Assessment of the impact of TOF on image quality

TOF reconstruction algorithms promise large improvement in image SNR (Rose, 1973) as reported by several literatures (Harrison et al., 2005; Manjeshwar et al., 2005). The localization of the annihilation point along the line of TOF allows the reconstruction algorithm to filter out coincidence events that have an inconsistent TOF value. This has a direct positive effect on the noise variance of the resulting image. Image quality for a certain system is defined as how good an image is for a particular task and an overall measure of a system performance (i.e., not just how well it collects counts). One class of image quality metrics called estimators (Barrett, 1990) consists of objective measures like SNR (Rose, 1973), contrast and noise variance (Karp et al., 2008; Tong et al., 2010).

We computed the SNR as the difference between the lesion and background relative to the noise level in the background:

$$SNR = \frac{Signal\ -\ Background}{\sigma_B} \tag{4.2}$$

where the signal is defined as the mean value in a region of interest (ROI) well inside the lesion, the background is defined as the mean value in a ROI localized in a fairly uniform area outside the lesion, and the noise in this formula is defined as the standard deviation of the value in the background ROI.

The contrast is a measure of the convergence of an iterative algorithm, which tends to increase and converge towards an asymptotic ‘true’ value. The measured contrast deviates from the real value due to Partial Volume Effects (PVE) caused by the limited resolution of the image. As the resolution improves, the PVE is reduced and the contrast increases. The contrast is defined as:

$$Contrast = \frac{Signal}{Background} \tag{4.3}$$

On the other hand, with iterative algorithms, noise increases monotonically with each iteration. To make it easier to compare the noise among different acquisition, it is defined as the ratio between the standard deviation of the background and the background level (in %)

$$Noise = \frac{\sigma_B}{Background} \times 100 \tag{4.4}$$

Acquisition method

A NEMA image quality phantom (see section 4.3.1) was simulated. Several list mode acquisitions were simulated with different number of counts covering typical high and low statistics cases counts rates (970×10^6, 112×10^6, and 12×10^6 counts).

A conventional version of the reconstruction algorithm (GFIRST) without TOF information was used to reconstruct non-TOF images and a version incorporating a TOF time resolution kernel was used to reconstruct the TOF images. Data were reconstructed with a high resolution mode, 336 × 336 × 109 voxels, and voxel size of $2 \times 2 \times 2$ mm^3. Main input information of the GFIRST algorithm is presented in appendix A2.

Standard NU 2-2007 (NEMA, 2007) analysis was performed by drawing circular regions of interest (ROIs) on the spheres as well as on the background regions. The ROIs used for evaluating the background noise were manually defined. Twelve ROIs of the same size as the ROIs drawn on the hot spheres were drawn randomly throughout the background (Figure 4.17). Taking the mean value in each region, results in the average mean value of all regions were used for the calculations of SNR. A quantitative analysis was performed by estimating SNR as a function of the number of iterations in the reconstruction, and contrast as a function of noise for different numbers of iterations.

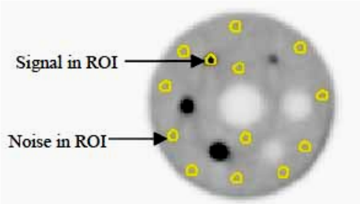

Figure 4.17. Simulated NEMA image quality phantom with 12 background ROIs and one signal ROI (10 mm sphere) used to compute SNR, contrast, and background noise.

The choice of the total number of iterations should ideally be matched to the statistics of the data. Hence both non-TOF and TOF reconstructions were performed with 1 to 5 iterations and 5 subsets. The SNR was defined by equation (4.2), and contrast and noise were defined according to equations (4.3) and (4.4), respectively. For each sphere, SNR was plotted as a function of iteration number, and contrast as a function of noise for different numbers of iterations. The gain in SNR (G_{SNR}) due to TOF compared with non-TOF that can be computed as the ratio $SNR_{max\text{-}TOF}/SNR_{max\text{-}nonTOF}$.

4.5. Results and discussion

Image quality assessment at high statistics (970 Mcounts)

The results obtained in this section are representative of cases in which there is little noise in the acquired data, which correspond to acquisitions with a high injected activity and/or long acquisition time.

A central slice of the reconstructed volume of the IQ phantom containing the hot spheres is shown in Figure 4.18 using five iterations. Improved image quality can be observed for the smallest lesion (10 mm sphere) when images are reconstructed using the TOF information. The SNR for the lesions smaller than 15 mm was studied and the results are shown in Figure 4.19, where lesion SNR is plotted as a function of iteration number. The maximum SNR was reached earlier for the spheres reconstructed with TOF than without TOF, where noise continues to increase. The non-TOF image takes longer to reach a value consistent with convergence. The iteration number that maximized the SNR of the smallest sphere lesion (10 mm) can be selected as a practical standard for further study. As can be seen in Figure 4.19, the maximum SNR for the 10 mm sphere using non-TOF reconstruction occurred at iteration 4. When TOF is used, this maximum occurred at iteration 2, with an improvement in image quality.

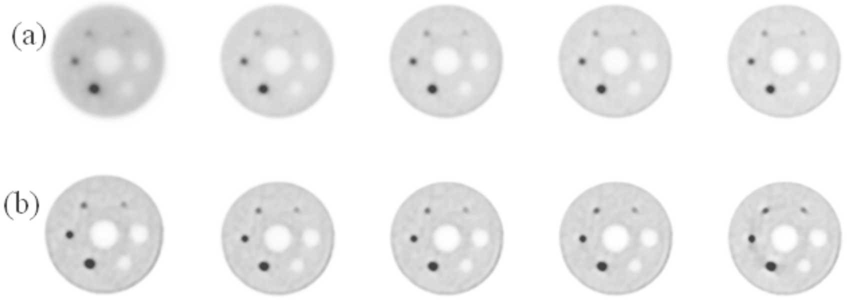

Figure 4.18. Reconstructed images of the NEMA image quality phantom with 8:1 sphere-to-background ratio. Non-TOF images (a) and TOF images (b). Results for 1 to 5 iterations are shown, from left to right.

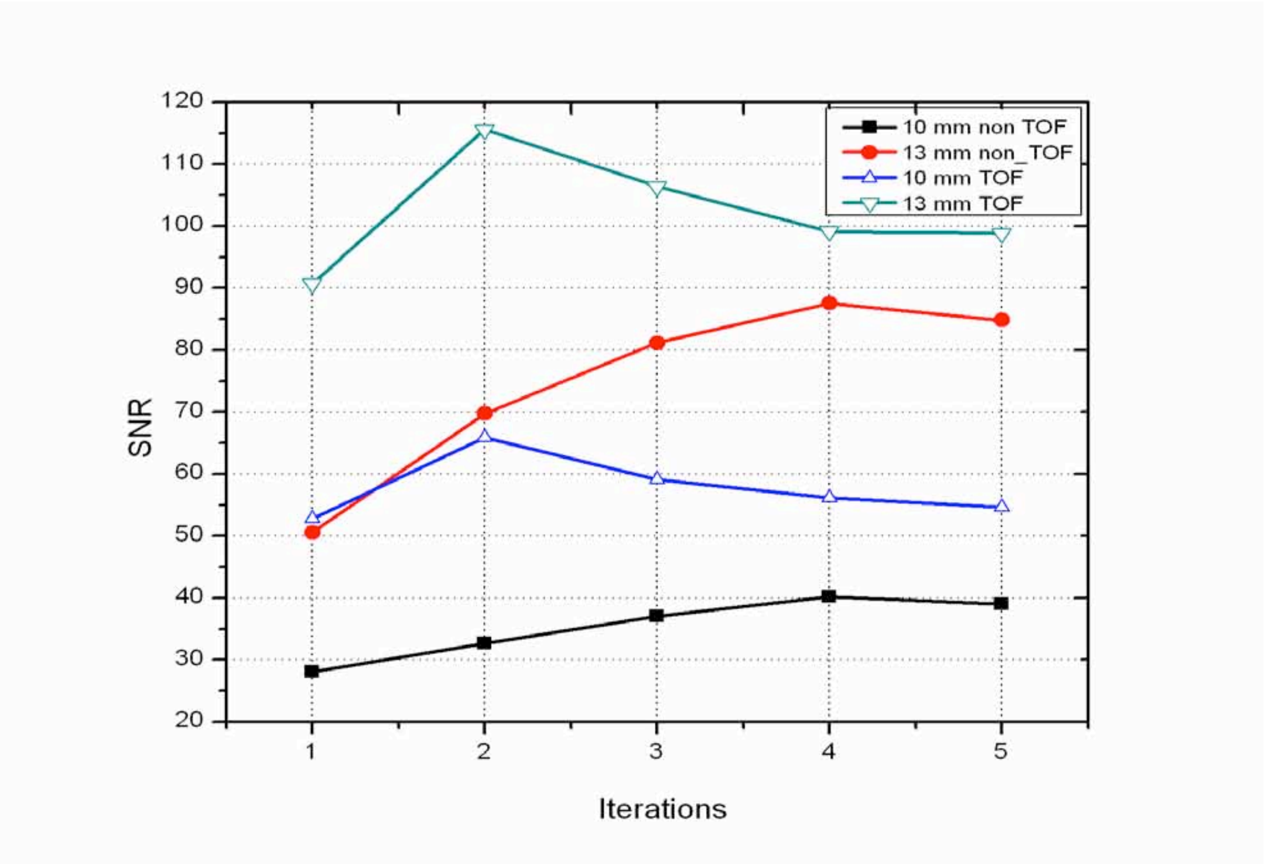

Figure 4.19: Lesion SNR vs number of iterations for both TOF and non-TOF. Each point corresponds to 1 iteration with 10 subsets.

Table 4.1. Contrast as a function of iteration number for the small spheres (shaded cells correspond to maximum SNR obtained)

Iteration	*Contrast*			
	TOF		*Non TOF*	
	10 mm	*13 mm*	*10 mm*	*13 mm*
1	*2.8*	*4.0*	*1.8*	*2.3*
2	*3.1*	*5.0*	*2.3*	*3.5*
3	*3.9*	*6.2*	*2.6*	*4.3*
4	*4.3*	*6.8*	*2.9*	*4.8*
5	*4.6*	*7.5*	*3.0*	*5.2*

In Table 4.1, the contrast is listed as a function of iteration number for the 10 mm, and 13 mm spheres for both the non-TOF and TOF reconstruction (the contrast to background ratio used in the simulation was 8:1). It can be seen that for a given iteration number, contrast level is higher for the TOF cases compared with the non-TOF ones. The shaded cells correspond to the optimal iteration number for each reconstruction method according to the SNR as obtained from Figure 4.19. A 5 – 10% in contrast is seen for the TOF reconstruction, at the optimum SNR point.

Figure 4.20, shows the contrast as a function of noise for the 10 and 13 mm spheres (each data point correspond to 1 iteration with 10 subsets), for non-TOF and TOF reconstruction. It can be seen (Figure 4.20) that for a given iteration number, both contrast and noise levels are higher with TOF compared to non TOF, as a clear consequence of the faster convergence of TOF reconstruction. When the optimal number of iterations in each case is selected, a similar value for contrast is reached, being the main difference the amount of noise in the images. For example, the 10 mm sphere has a contrast of 2.93 at 4 iterations without TOF and 3.09 at 2 iterations with TOF, whereas the noise level at those iterations is 4.5% and 3.6% for the non-TOF and the TOF cases respectively.

These results are in agreement with previous studies performed to assess the impact of TOF on image quality, like the one developed by Cristina Lois and collaborators (Lois et al., 2010) on a mCT Biograph scanner, and the experimental study performed in the B-TPTV PET/CT scanner (Jakoby et al., 2012). In both cases, with TOF information a greater SNR is achieved for the same contrast level, yielding higher lesion delectability, mostly because noise is reduced.

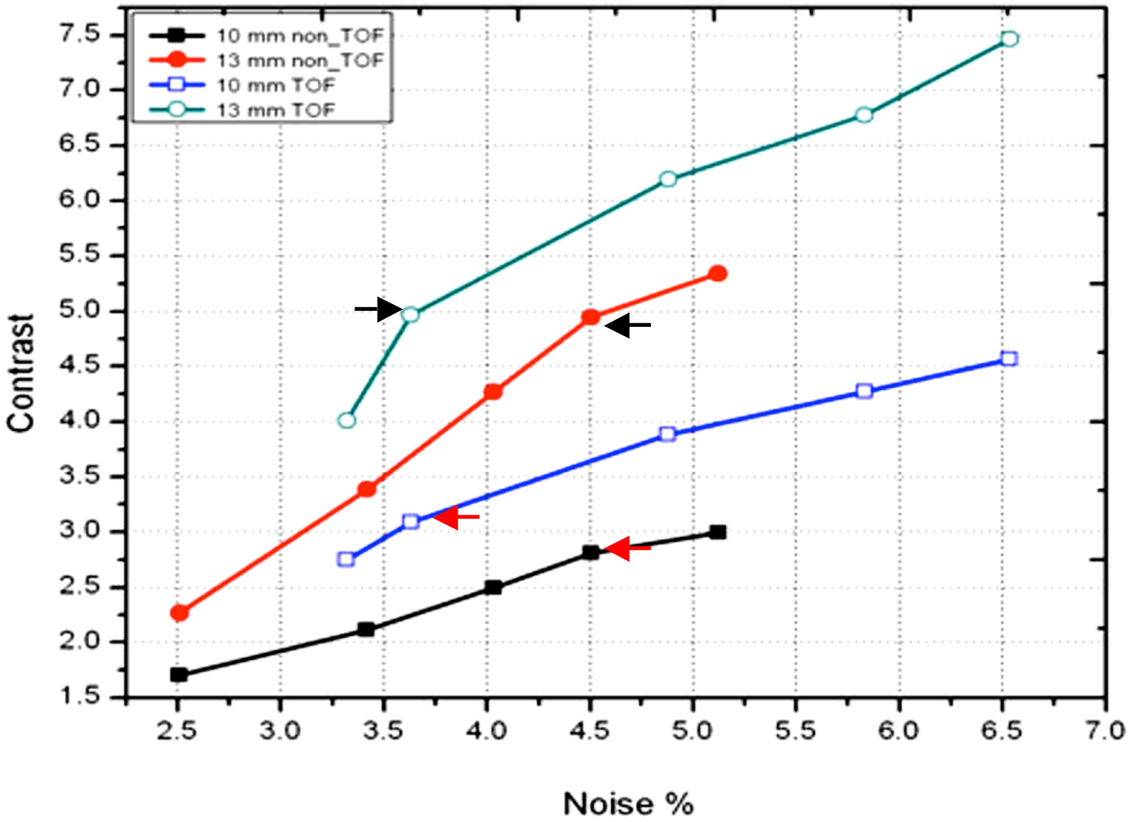

Figure 4.20. Contrast as a function of noise level for both non-TOF and TOF images (each data point corresponds to one iteration). The arrows indicate the selected iteration with higher SNR for each case.

Image quality assessment at intermediate count statistics (112 Mcounts)

In this section we assessed the impact of the TOF information in the image quality in a case with less counts.

Figure 4.21 shows lesion SNR plotted as a function of iteration number. We can observe the same behavior found with high number of counts, being the maximum of SNR reached earlier for the TOF-case than non-TOF one. The maximum SNR for both 10 and 13 mm spheres using TOF occurred at iterations 2, while it is reached at iteration 3 for non-TOF reconstruction. We can see that in both cases, the SNR reached is lower than in the previous case, due to the lower number of counts. The increase in the SNR for the 10 mm sphere with TOF respect to the case without TOF one, varied from a 60% in iteration 1, to a 6% in iteration 5. This result agrees with the clinical study for liver lesions performed by George El Fakhri (El Fakhri et al., 2011).

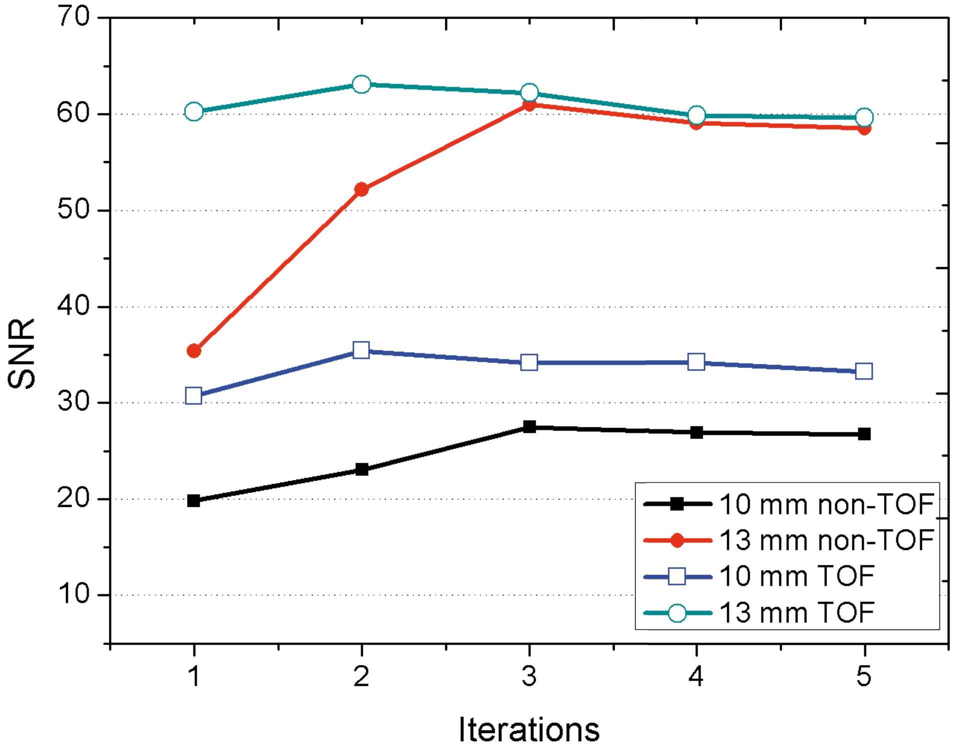

Figure 4.21: Lesion SNR vs number of iterations for both TOF and non-TOF. Each point corresponds to 1 iteration with 5 subsets.

In Table 4.2, noise and contrast are listed as a function of iteration number for the 10 and 13 mm spheres, both for non-TOF and TOF reconstructions. It can be observed that for a fixed iteration number, both contrast and noise level are higher for TOF compared with non-TOF, as a consequence of the faster convergence of the TOF reconstruction. When the optimal number of iterations for the SNR in the lesions is selected, a similar value for contrast is reached with the two methods. For example, the 13 mm sphere has a measured contrast of 3.81 at 3 iterations without TOF and 3.87 at 2 iterations with TOF, being the noise level lower in TOF reconstruction: 5.41% without TOF respect to 5.04% with TOF.

Table 4.2 Contrast and background noise for each iteration (shaded cells corresponds to maximum SNR obtained above)

Iteration	*Contrast*				*Noise (%)*	
	TOF		*Non-TOF*			
	10 mm	*13 mm*	*10 mm*	*13 mm*	*TOF*	*Non-TOF*
1	*2.3*	*3.3*	*1.8*	*2.4*	*4.4*	*3.9*
2	*2.8*	*3.9*	*2.3*	*3.3*	*5.0*	*4.5*
3	*3.3*	*4.4*	*2.7*	*3.8*	*6.0*	*5.4*
4	*3.6*	*4.6*	*2.9*	*4.1*	*6.9*	*5.8*
5	*3.8*	*4.7*	*3.0*	*4.5*	*7.5*	*6.9*

Image quality assessment at low count statistics (12 Mcounts)

In this case, we considered acquisitions with low number of detected coincidences, which are often found in studies with low injected activity, or low acquisition times, that may occur in a single frame of dynamic studies.

Figure 4.22 and Figure 4.23 present SNR as a function of iteration number and contrast as a function of noise level, respectively. As expected, SNR in these acquisitions is lower than in the previous simulated studies. Nevertheless, the behavior of SNR and contrast for both non-TOF and TOF reconstructions is similar to previous cases. For instance, the maximum SNR is reached at iteration 2 with TOF compared to the 3 iterations required without TOF, as Figure 4.21 shows.

Furthermore, lesion detection SNR was significantly higher for all iterations for TOF than for non-TOF. The contrast when using TOF is higher compared to the non-TOF case.

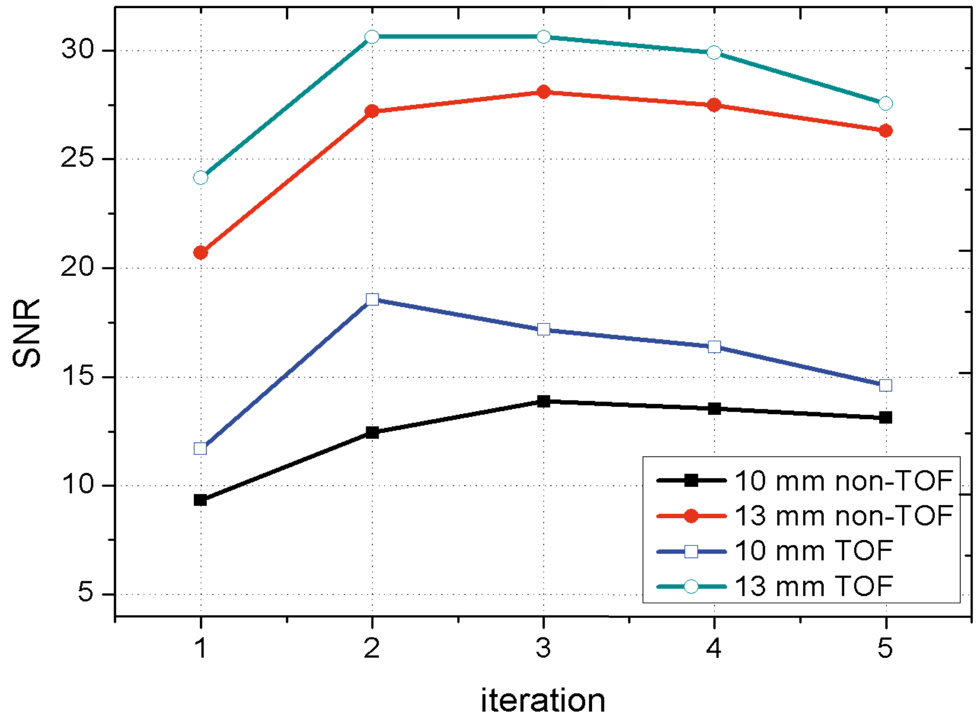

Figure 4.22. Lesion SNR respect to number of iterations for both TOF and non-TOF reconstructions. Each point corresponds to 1 iteration with 5 subsets.

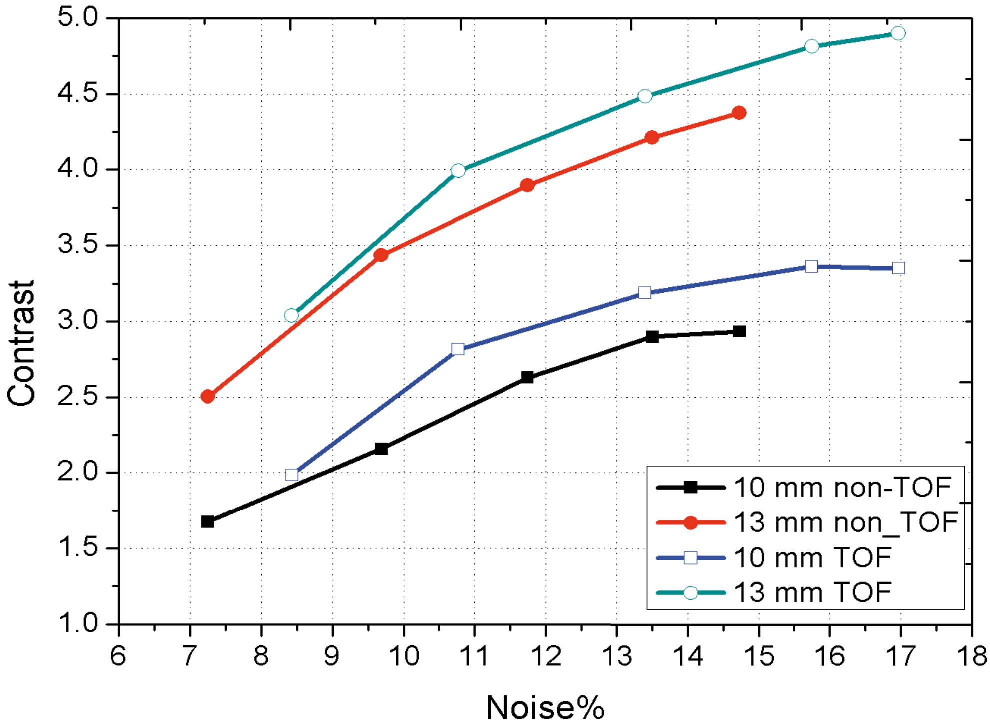

Figure 4.23. Contrast as a function noise for both non-TOF and TOF. Each data point corresponds to one iteration.

4.5.1. Comparison of TOF and non-TOF results

Table 4.3 Contrast and background noise comparisons for 10 mm spheres of the non- TOF and TOF images for the 3 different studies, each value corresponsd to the optimal number of iterations as obtained from the SNR for both TOF and non-TOF.

	Contrast			**Noise %**			**SNR/iteration**		
Counts (Mcts)	**970**	**112**	**970**	**112**	**12**	**12**	**970**	**112**	**12**
Non-TOF	**2.9**	**2.7**	**2.9**	**2.7**	**2.6**	**2.6**	**4**	**3**	**3**
TOF	**3.1**	**2.8**	**3.1**	**2.8**	**2.8**	**2.8**	**2**	**2**	**2**

Table 4.3 presents the comparison between contrast as a function of noise of the 10 mm spheres in all the studies performed above. We can observe that, as expected, the contrast obtained in the three studies with TOF is higher than for non-TOF reconstructions, whereas the noise increases as the number of counts is reduced, being lower for TOF studies.

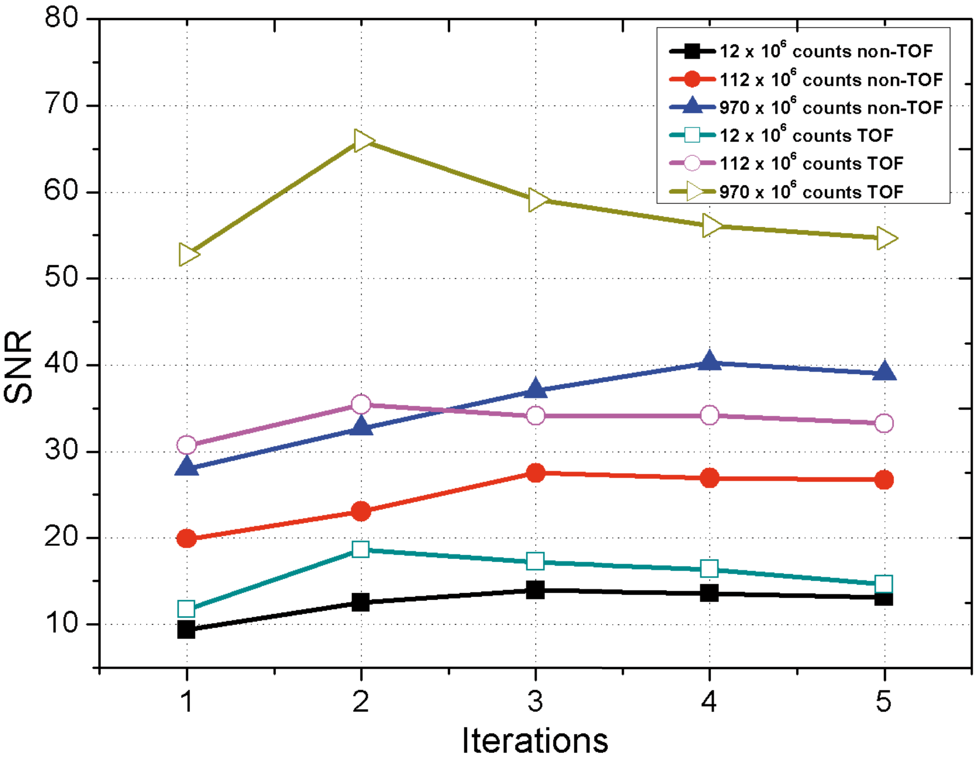

Figure 4.24: Lesion SNR vs number of iterations for the 10 mm spheres for both TOF and non-TOF reconstructions.

Figure 4.24 shows the SNR of the 10 mm spheres for both non-TOF and TOF reconstructions. It is clear that, as expected, the high-counts study has significantly higher SNR compared with the low-statistics one for both cases.

Furthermore form Table 4.4 it can be observed that the SNR gain when using TOF is larger for the high-counts study, compared with the lower statistics one. The maximum SNR gain for the high-statistics (970 Mcounts) is 21% larger for the smallest sphere (10 mm) at 112 Mcounts and 27% for the 12 Mcounts at iteration 2. Our results of SNR Gain (Table 4.4) agree with the clinical study by (Lois et al., 2010) where they obtained a SNR gain in TOF images with a range of 1.2 to 2.

TOF reconstruction converged faster than non-TOF and resulted in lower image noise, which agrees with study performed (Kadrmas et al., 2009) to asses TOF performance in a clinical study.

Table 4.4. SNR_{gain} of the 10 mm spheres, each value correspond to optimal number of iterations as obtained from the maximum SNR for both TOF and non-TOF

Counts (Mcts)	**970**	**112**	**12**
SNR_{gain}	**2.0**	**1.6**	**1.5**

4.6. Conclusion

This work, based on simulation studies using the image quality phantom, focused on the assessment of image quality obtained with TOF incorporated into the reconstruction, particularly in small lesions (spheres <15 mm). The reconstruction method used was based on GFIRST, using the OSEM3D algorithm with a Gaussian PSF for modeling the system-response-matrix, a median filter for the regularization and incorporating TOF information.

It is well known that, working with iterative algorithms, there is a trade-off between contrast and noise. For GFIRST we identified the number of iterations required to achieve the optimal SNR, which was different for non-TOF and TOF reconstructions. This was expected, due to the better localization of the annihilation events when TOF is included. The appropriate number of iterations that offer a good trade-off between contrast and noise was explored at high and low statistics. In all these studies, TOF reconstruction converged faster and resulted in lower image noise.

The iteration number which maximized the SNR for small lesions was identified to be 2 for TOF reconstruction for high and low counts. For non-TOF reconstructions SNR was best at iteration 4 for high counts and at iteration 3 for lower counts. It is interesting to note that this criterion provided images which reached similar contrast, but the TOF image had the advantage of a lower noise level.

The goals of this work were to demonstrate that GFIRST is flexible to incorporate TOF information, and to investigate the gain in image quality with TOF. Our GFIRST framework was validated for non-TOF sinograms reconstruction in a previous work, (Herraiz et al., 2011). Here, we further demonstrate that the same GFIRST framework can be utilized for reconstructing TOF PET data using the sinograms. GFIRST is flexible to include PSF, median filter and TOF information, in addition to low reconstruction time (around 1 minute per iteration), so that it could be used for real clinical TOF PET scanners.

Furthermore, this work has demonstrated with phantom studies that the incorporation of TOF information results in a more rapid convergence of the reconstruction algorithm, and lower noise for the same contrast. It has been shown quantitatively that the SNR gain due to TOF has the greatest effect in high counts studies.

5. Summary and conclusions

In this final chapter the main contributions of this thesis are summarized, and the conclusions derived from the results of this work are presented.

MC simulations have been proven to be a very useful tool to study imaging characteristics and parameters of PET scanners that in some cases cannot be directly measured experimentally. The design of new PET scanners is one area that benefits from extensive simulations (as shown in chapter 3), as well as improved data analysis, correction techniques and image reconstruction algorithms assessment (chapter 4) among other applications.

The main contributions of this thesis are:

- A PET Monte Carlo simulation tool (PeneloPET) has been extended and validated for clinical scanner. Simulations of acquisitions mimicking the NEMA protocol for measuring sensitivity, NEC and SF were performed. We have shown that PeneloPET is flexible enough to easily accommodate characteristics of the electronics, which have been adapted to reproduce the experimental NEC curves of the B-TPTV scanner. Once the simulation was set to reproduce the sensitivity of the B-TPTV scanner, predictions for scatter fraction derived from the simulation, agree with the measured values for the three scanners of the same family under investigation. Furthermore, the sensitivity and NEC rate curves for both the B-TP and mCT are also reasonably predicted.
- With PeneloPET we were able of assessing the impact of the modification of some parameters of clinical scanners on their performance. We studied the performance of the PET scanners using sensitivity, NEC and SF as figures of merit. For instance, the impact of the energy window on the system sensitivity, the NEC peak value and SFs was studied in detail. Simulations allowed the identification of optimal choices for coincidence time and energy windows. In general, the optimal values obtained correspond to the ones being used in the real scanners.
- We have shown that PeneloPET is capable of incorporating TOF properties of the scanners in the simulation. This is of paramount importance to describe modern clinical PET systems.

- The reconstruction software GFIRST was modified to incorporate TOF information, and with it we investigated the gain in image quality that can be achieved using TOF in different situations.
- The incorporation of TOF information results in more rapid convergence of the reconstruction algorithm, better image contrast, and lower noise. Furthermore, it has been shown quantitatively that the SNR gain due to TOF has the larger effect in higher counts acquisitions.

5.1. Final Conclusions

As a summarizing conclusion, with this thesis we have completed the set of tools for the improvement of clinical PET scanners, both in the simulation and reconstruction arena. TOF properties of the scanner have been incorporated and a GPU reconstruction code, extremely fast and very accurate, able for clinical settings, has been set. The results obtained in this thesis paved the way for the ongoing and future developments of the group where this work has been carried out, Indeed, the availability of a very fast reconstruction code opens up the possibility for high quality on-line (even list-mode) image reconstructions and for the incorporation of powerful data correction techniques. This will show up in coming projects in collaboration with the long-standing partners at LIM (Gregorio Marañón Hospital) with clinical teams specialized in PET imaging at the Massachusetts General Hospital (Boston) and the Hospital Clínico (Madrid).

Summary

SIMULATION AND IMAGE RECONSTRUCTION OF CLINICAL TOF-PET SCANNERS

Khaled M A Abushab

Positron emission tomography (PET) is the most sensitive molecular imaging technique. Positron-emitting radioisotopes are used to label molecules of interest (tracers) which are injected in small amount into a patient for clinical examinations and medical research *in vivo*. The tracer will distribute in the body according to its particular physiological pathway and its distribution can be imaged in a PET scanner by measuring and localizing the two gamma-rays originated from the annihilation of the positron emitted by the radioisotopes.

Although PET was originally used as a research tool for the study of the biodistribution of many different radiotracers, in recent years it has become very important in the clinical practice, especially in oncology. Most of the clinical PET studies today use ^{18}F-FDG as a radiotracer, as this allows measuring glucose metabolism, which is known to be significantly enhanced in most tumors. The combination of PET images with anatomical information provided by a CT scanner in combined PET/CT scanners, has been an important step towards its use in the clinic.

The recent introduction of a new generation of PET/CT scanners with fast scintillators and good stopping power for 511 keV photons has been another significant improvement in the technique. These scanners may use the difference between the arrival times of the pair of photons originating from positron annihilation (Time-of-Flight information) to improve the quality of the reconstructed image. Therefore, Positron Emission Tomography (TOF-PET) may improve the image signal-to-noise ratio (SNR) and therefore, the detectability of lesions in the images.

Nevertheless, there are still some limiting factors for a wider use of the technique. On one hand, PET needs non-stable isotopes which decay emitting a positron, and therefore for isotopes like ^{18}F, this requires a cyclotron which can produce the isotopes by collision of accelerated particles. This problem is being addressed by the construction of more cyclotrons which could provide the required isotopes for most of the large hospitals. Other problem of PET is its relative poor resolution (about 5 mm) compared with other imaging modalities like CT or MRI. New scanners with are being designed to improve this resolution. And finally, there is a need for reducing the amount of radiation injected into the patients for a PET scanner, in order to minimize the possible side effects of the radiation. This is being solved by the use of new scanner designs with higher sensitivity and better localization in the patient of the detected events with the TOF technique, which allows obtaining images with similar quality with lower radiation doses to the patient. This thesis is focused on the study of some of these new designs with simulations and the evaluation of the improvement obtained by the new TOF-PET/CT scanners in different situations.

Monte Carlo (MC) methods give us a chance to estimate scanner properties which cannot be obtained experimentally, as well as well as testing the changes in the performance of PET scanners due to changes in the scanner, without having to builds all these prototypes. PeneloPET is a MC code based on PENELOPE (also a MC code), for PET simulations which considers detector geometry, acquisition electronics and materials, and source definitions. This tool is used for the simulation of transport of electrons, positrons and photons, with energies up to 1 GeV. PeneloPET is a code for PET simulations with basic components of detector geometry, acquisition electronics and material and source definitions. MC simulations are widely used in PET for optimizing detector design, acquisition protocols, and for developing and assessing corrections and reconstruction methods.

This thesis is based on PeneloPET simulations of several acquisitions with some of the last generation TOF-PET/CT scanners. One of the main goals of this thesis is to validate PeneloPET, which have been already validated in preclinical scanners, with clinical PET scanners. Thus, we used PeneloPET to simulate the Biograph TruePoint (B-TP), Biograph TruePoint with TrueV (B-TPTV) and Biograph mCT PET/CT scanners. These configurations consist of three (B-TP) and four (B-TPTV and mCT) rings of 48 detector blocks. Each block comprises a 13 × 13 matrix of 4 × 4 × 20 mm^3 lutetium oxyorthosilicate (LSO) crystals. Simulations were adjusted to reproduce some experimental results from the actual scanners and validated by comparing their predictions to further experimental results. Sensitivity, spatial resolution, noise equivalent count (NEC) rate and scatter fraction (SF) were estimated. The simulations were then employed to assess optimum values of system parameters, such as energy and time coincidence windows and to evaluate the effect of system modifications (such as number of rings) on performance. Furthermore we checked the capability of the PeneloPET code to incorporate TOF of the scanners.

We have shown that PeneloPET is flexible enough to easily accommodate different dead time ingredients in the electronics, which have been optimized so that the experimental NEC curves for the B-TPTV could be reproduced. Once the simulation was set to reproduce the sensitivity of the B-TPTV scanner, predictions for SF derived from the simulation, agree within 5% with the measured values for the three scanners under investigation. Furthermore, the sensitivity and NEC rate curves for both the B-TP and mCT are also reasonably predicted, after fixing parameters of the simulations to the B-TPTV experimental rate curves. The simulated and experimental spatial resolution results were also comparable.

These performance results validate the use of PeneloPET to simulate the clinical scanners. Therefore, simulations were employed to investigate the variation of several basic scanner parameters on the performance of the B-TPTV system. We have shown that PeneloPET is capable of easily incorporating TOF properties of the scanners in the simulation. This is of paramount importance to describe modern clinical PET systems.

This thesis also studies the impact in the reconstructed images of the TOF information. PET images map the origins of photons emitted from the patient. If the PET scanner detects these two photons within a particular interval of time, called the coincidence window, it will record a line of response (LOR) that connects the points where the two photons were detected. The collection of LOR data is referred to as the projection data. We used our GFIRST code based fully 3D iterative reconstruction 3D-OSEM in addition to investigate the gain in image quality that can be achieved using the TOF information in different simulated cases. We estimate image SNR and contrast in hot lesions (spheres of less than 15 *mm* in diameter), as well as background noise in reconstructed images, both with and without TOF information.

In this thesis we have demonstrated the benefit of TOF information in PET scanners based on a simulated phantom. We found that TOF information in our reconstructed code yields better image contrast and lower noise, and also that TOF reconstructed achieved larger SNR than without TOF. It has been shown quantitatively that the SNR gain due to TOF has the greatest effect in high counts statistics.

As a summarizing conclusion, this thesis shows that PeneloPET is a powerful tool for simulating and design clinical PET scanners. Furthermore, the reconstruction code, GFIRST has shown enough flexibility to incorporate TOF information and study its impact on the reconstructed image quality. The combination of these tools presented in this thesis can be used to develop new clinical scanner designs that could provide images with better resolution, better lesion detectability and requiring lower radiation dose to the patients.

Supervisors: José Manuel Udías Moinelo
Joaquín López Herraiz

LIST OF FIGURES

Figure 2.1. Basic principle of PET scanner and data processing (Steinbach, 2011) *10*

Figure 2.2. Experimental b^- *spectra obtained from decaying* ^{64}*Cu.* b^- *particles are affected by the electric field of the positively charged nuclei and thus the energy spectrum is shifted towards lower energies.* b^+ *particles, on the other hand, are repelled by the nuclei so the energy spectrum it is shifted towards higher energies (Krane, 1987).* *11*

Figure 2.3. In PET, each detector generates a timed pulse when it registers an incident photon. These pulses are sent to a coincidence circuitry, and if they fall within a short time-window, they are deemed to be coincident. A coincidence event is assigned to a LOR joining the two relevant detectors *12*

Figure 2.4. Scheme representing the definition of positron range. From its emission, the positron follows an erratic path until the annihilation process (a). Non-colinearity is independent of radionuclide, and the error introduced depends on the separation of the detectors. This is due to the fact that the annihilation does not take place exactly at rest, as the electrons are at room temperature and thus have some momentum. Thus the two annihilation photons are not emitted exactly at 180^{o}*, but with a slight deviation. Two detectors detect these photons and assign the event to a straight line, which is not the original annihilation line (b)* *13*

Figure 2.5. basic elements of a PMT. Adapted from (Powsner and Powsner, 2008) *17*

Figure. 2.6. Different types of detected events in PET: (a) true, (b) multiple, (c) single, (d) random and (e) scattered (adapted from (Cherry et al., 2003)). *19*

Figure 2.7. The projections of a point source at different angles (left) are represented with a sine curve in a sinogram representation of the data acquired (Bailey, 2005). *23*

Figure 2.8. A 3D PET sinogram contains the 2D direct sinograms and all oblique sinograms (a). Axial mashing may be performed to reduce the 3D PET data size (b). The "span" parameter determines the number LORs which will be combined. *24*

Figure 2.9. Three examples of Michelograms for a 8-ring scanner corresponding to three different acquisitions: 2D acquisition (a), 3D acquisition without mashing (b), and 3D acquisition with "mash" (c), where the span is 5 (2 + 3) and maximum ring difference (MRD) is 7 (8-1). Axial location is along the bottom left to top right diagonal direction (Defrise et al., 2005) *25*

Figure 2.10. Energy spectra showing the window setting; (a) dual energy window method and (b) estimation of trues method (Meikle and Badawi, 2005). *30*

Figure 2.11. Principles and main components of a Monte Carlo program dedicated to the simulation of cylindrical multi-ring PET imaging systems. Adapted from (Zaidi, 2006) *35*

Figure 2.12. Schematic representation of the principle of a rebinning algorithm for 3D PET data. Adapted from (Defrise et al., 2005). *38*

Figure 2.13. SSRB; an illustration of the set of oblique LORs transformed into a single transaxial LOR ... *38*

Figure 2.14. Pictorial illustration of the two-dimensional central-section theorem, showing the equivalency between the one-dimensional Fourier transform (top right) of a projection at angle ϕ *(top left) and the central-section at the same angle (bottom left) through the two dimensional Fourier transform of the object (bottom right) (Bailey, 2005a).* *40*

Figure 2.15. Back-projection, $b(x,y,f)$*, into an image reconstruction array of all values of* $p(s,f)$ *for a fixed value of* ϕ *(Henkin et al., 2006).* *41*

Figure 3.1. B-TPTV PET/CT scanner geometrized by Siemens (a) and a transverse section of the transaxial FOV of the scanner, with scintillations detectors (b) *56*

Figure 3.2. Scanner geometry of the B-TPTV scanner (detector modules) with the NEMA test phantom at the middle of the scanner. *56*

Figure. 3.3. Source emissions (green points) and interactions of the emitted photons with the detector crystals (red points) *58*

Figure 3.4. Positioning of the NEMA scatter phantom, used for the measurement of NEC and SF. *60*

Figure 3.5. Arrangement of the six points sources in the measurement of spatial resolution. Three sources are positioned at the center of the axial FOV and three sources are positioned at one-fourth of the axial FOV away from the center. At each position, sources are placed on the positions indicated in a transverse plane perpendicular to the scanner axis (NEMA, 2007) *61*

Figure 3.6. Comparison of random and true rate curves as a function of activity concentration predicted by PeneloPET simulations adjusted to the experimental results of the B-TPTV. The random rate curve has been multiplied by 0.4. .... *66*

Figure 3.7 Comparison of NEC rate curves as a function of activity concentration of the fit of PeneloPET

to the experimental data. All curves have been obtained with coincidence time and energy windows same as in (Jakoby et al., 2009, 2011). 67
Figure 3.8. Gaussian fit of the simulated TOF distribution from a centered source. And additional time jitter of 170 ps is employed in the simulations to produce a TOF resolution of 550 ps (FWHM) for the B-TPTV scanner. 69
Figure 3.9. Simulated sensitivity of the B-TPTV scanner as a function of the crystal length 70
Figure 3.10. Sensitivity of the B-TPTV scanner as a function of energy resolution for a fixed energy window of 425 - 650 keV. 71
Figure 3.11 NEC rates as a function of the LLD for the B-TPTV scanner. 72
Figure 3.12. NEC curves with different coincidence time windows for the B-TPTV scanner. 4.5 ns optimized the highest value 73
Figure 4.1. Flowchart of the implementation of the code in the GPU (Herraiz et al., 2011). 80
Figure 4.2. Drawing of the phantom with hot and cold spheres and the central lung insert with no activity (NEMA, 2007). 82
Figure 4.3. Michelogram of the Biograph TPTV scanner with span 11 and 7 segments. 83
Figure 4.4. Time alignment used in this thesis, as suggested by Siemens 83
Figure 4.5. Sinograms of the NEMA image quality phantom (TOF bins from -3 to +3, each 312 ps wide). 84
Figure 4.6. Simulation of uniform phantom (normalization phantom) at the center of the PET scanner FOV (a); and simulated sinogram obtained (b). 85
Figure 4.7. Image quality phantom sinograms; Before normalization (a) and after normalization (b) 85
Figure 4.8. Example of a Normalized 2D sinogram with gaps (a); Mask used to define the gaps (b) and gap-filled sinogram (c). 86
Figure 4.9. FBP reconstruction of the image quality phantom: without normalization (a), with normalization (b) and with normalization and gap filling (c). 86
Figure 4.10. Radial profile of the small spheres of the image quality phantom 87
Figure 4.11. CT-based attenuation correction of PET emission data: attenuated cylinder (a), CT image (b), sinogram of the attenuation map obtained from the CT image (c) and profile of the sinogram (d) 88
Figure. 4.12. Comparison of images reconstructed without (a) and with (b) attenuation correction. 88
Figure. 4.13. Radial profile along the largest sphere of the reconstructed images with (red) and without (green) attenuation correction. 88
Figure 4.14. Flowchart of the implementation of RR-GFIRST code (Vicente, 2012). 90
Figure 4.15. Contrast and noise in the image quality phantom (using as reference the 17-mm spheres) for different number of iterations using different PSF values. Each point corresponds to one iteration. 91
Figure 4.16: Profile of images reconstructed with and without TOF for 10 and 13 mm spheres after one iteration 93
Figure 4.17. Simulated NEMA image quality phantom with 12 background ROIs and one signal ROI (10 mm sphere) used to compute SNR, contrast, and background noise. 94
Figure 4.18. Reconstructed images of the NEMA image quality phantom with 8:1 sphere-to-background ratio. Non-TOF images (a) and TOF images (b). Results for 1 to 5 iterations are shown, from left to right. 95
Figure 4.19: Lesion SNR vs number of iterations for both TOF and non-TOF. Each point corresponds to 1 iteration with 10 subsets 96
Figure 4.20. Contrast as a function of noise level for both non-TOF and TOF images (each data point corresponds to one iteration). The arrows indicate the selected iteration with higher SNR for each case. .97
Figure 4.21: Lesion SNR vs number of iterations for both TOF and non-TOF. Each point corresponds to 1 iteration with 5 subsets 98
Figure 4.22. Lesion SNR respect to number of iterations for both TOF and non-TOF reconstructions. Each point corresponds to 1 iteration with 5 subsets. 100
Figure 4.23. Contrast as a function noise for both non-TOF and TOF. Each data point corresponds to one iteration. 100
Figure 4.24: Lesion SNR vs number of iterations for the 10 mm spheres for both TOF and non-TOF reconstructions. 101

LIST OF TABLES

Table 2.1. Properties of some scintillators used in PET detectors. Note that some of these specifications are subject to change as developers change dopants and trace elements in the scintillator growth. For example, the light output, peak wavelength, decay time and density for LYSO vary some what for different versions of the basic scintillator. Adapted from (Lewellen, 2008)......16
Table 3.1. PeneloPET input files needed to simulate a cylinder source in the Biograph scanner (Jakoby et al., 2009); 'F' stand for false or disable option and 'T' stand for true or enable option. Full detail about this input file and options can be found in the PeneloPET manual......51
Table 3.2. Parameters of the Biograph PET/CT scanners evaluated (Jakoby et al., 2011, 2009)......55
Table 3.3. Characteristics of The PET Scanners Evaluated (from refs. (Jakoby et al., 2011, 2009)......57
Table 3.4. Sensitivity results of the PeneloPET simulation as well as measured and the simulated results of different systems......64
Table 3.5. Summary of values for NEC, and SF for different scanner configurations, according to simulations. In boldface are shown the results that were employed to fix some scanner parameters in the simulations. All results are obtained with a time coincidence window and an energy window same as the measured (Jakoby et al., 2011, 2009)......67
Table 3.6. Simulated and experimental spatial resolution for the B-TPTV scanner. Experimental results bear an uncertainty of ± 0.3 mm (Jakoby et al., 2009)......68
Table 3.7. Simulated values for SF vs LLD for B-TPTV PET scanner......72
Table 4.1. Contrast as a function of iteration number for the small spheres (shaded cells correspond to maximum SNR obtained)......96
Table 4.2 Contrast and background noise for each iteration (shaded cells corresponds to maximum SNR obtained above)......99
Table 4.3 Contrast and background noise comparisons for 10 mm spheres of the non- TOF and TOF images for the 3 different studies, each value corresponsd to the optimal number of iterations as obtained from the SNR for both TOF and non-TOF......101
Table 4.4. SNR_{gain} of the 10 mm spheres, each value correspond to optimal number of iterations as obtained from the maximum SNR for both TOF and non-TOF......102

APPENDICES

Appendix A1:

NEMA NU 2-2007 scatter phantom

The NEMA NU 2-2007 Scatter phantom (NEMA, 2007) is designed in accordance with the recommendations by the National Electrical manufacturers Association (NEMA) to standardize the measurement of count rate performance of a scintillation camera in the presence of scatter. Scatter Phantom is a 70 *cm* long polyethylene cylinder with a diameter of 20 *cm*. A line source filled with radioactivity and inserted into the phantom at a radial distance of 4.5 cm.

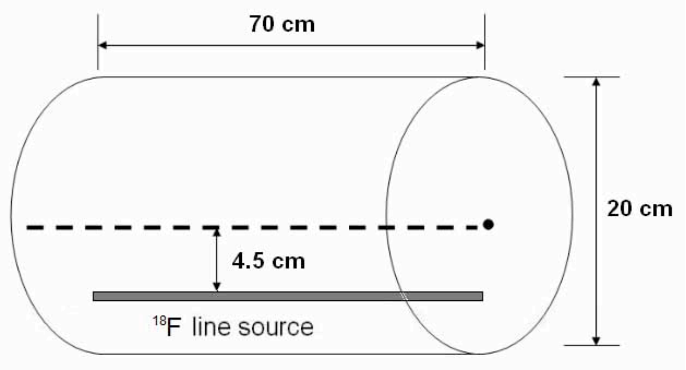

Figure A.1. *NEMA NU 2-2007 scatter phantom diagram* (NEMA, 2007).

Appendix A2:

Main input data of GFIRST for Biograph scanner (B-TPTV), here it is implemented all information regarding to TOF bins PSF and median filter in addition to number of iterations and subsets as well as image resolution.

```
static const float PI = 3.1415926f;

// PARAMETERS OF THE DATA -----
static const int NTBINS =13;                  // Number of TOF Bins

static const int NRAD = 336;                  // Number of radial bins
static const int NANG = 336;                  // Number of angles
static const int NROWS = 55;                  // Number of "rings"
static const int SPAN = 11;                   // Span of the sinogram (11 = Differences 5 and 6)
static const int NSINOGS = 559;               // Number of sinograms
static const int NSEGMENTS = 7;               // Number of segments
static const int NDATA = NSINOGS*NANG*NRAD;     // Total number of bins in the sinogram
//static const int MAXRINGDIF = 38;   // Maximum ring difference of the sinogram

// PARAMETERS OF THE RECONSTRUCTED IMAGE -----
static const int RES =336;                        // X-Y resolution
static const int NZS = (2*NROWS-1);               // Z number of slices
static const int NVOXELS=RES*RES*NZS;   // Total number of voxels in the image
static const int NPT = RES;
static const int NZSM = NZS/2;

// PARAMETERS OF THE RECONSTRUCTION
const int NITER = 5;
const int NSUBSETS = 5;
const int NDATA_PART = NZS*NRAD;      // Number of LORs projected simultaneously
float PSF_FW = 7.0;      // PSF for forward  (voxel units) Large = More Resolution
float PSF_BW = 5.0;     // PSF for backward (voxel units) Large = Smoother / Slower convergence

//  PARAMETERS OF THE SCANNER ----------------
__device__ __constant__ float pitch = 4.0f;                    // (mm)
__device__ __constant__ float DIAM_DET = 856.f;            // Distance between detectors (mm)
__device__ __constant__ float FOV = 680.f;                    // Field of View (mm)
__device__ __constant__ float TOF_FOV = 680.f;              // Field of View of the TOF (mm)
__device__ __constant__ float beta = 0.1f;                     // MEDIAN FILTER
```

Appendix B1:
List of publications and conference proccedings related to this thesis

- Abushab, K.M., Herraiz, J.L., Vicente, E., Cal-González, J., España, S., Vaquero, J.J., Jakoby, B.W., Udías, J.M., "*PeneloPET simulations of the Biograph PET scanner: Validation and Performance Investigations*". IEEE Transactions on Nuclear Science (submitted) 2012.

- K. M. Abushab, J. López Herraiz, E. Vicente Torrico, S. España Palomares, J.J. Vaquero López, J.M. Udías Moinelo, "*PeneloPET simulation of the Biograph PET scanner*" International scientific meeting on nuclear physics , La Rabida, Spain, 2012.

- Abushab, K.M., Herraiz, J.L., Vicente, E., Espana, S., Vaquero, J.J., Jakoby, B.W., Udias, J.M., 2011, "*PeneloPET simulations of the Biograph ToF clinical PET scanner*", in: Nuclear Science Symposium and Medical Imaging Conference, 2011, Conference Record of the 2011 IEEE. pp. 4420 –4428.

- K. M. Abushab, J. López Herraiz, E. Vicente Torrico, S. España Palomares, J.J. Vaquero López, J.M. Udías Moinelo "*Monte Carlo simulation of Biograph PET/CT*" XXXIII Reunión Bienal de la Real Sociedad Española de Física, 2011, pp. 214-215, Santander, España.

- K. M. Abushab, J. López Herraiz, E. Vicente Torrico, S. España Palomares, J.J. Vaquero López, J.M. Udías Moinelo, "*Validation of the peneloPET application for clinical PET/CT*" Encuentros de Física Nuclear 2010, El Escorial, España.

- K. M. Abushab, J López Herraiz, E Vicente Torrico, S España Palomares, JJ Vaquero López, JM Udías Moinelo. "*Validation of peneloPET simulations of the Biograph PET/CT scanner with TOF capabilities*". Proceedings del XXVIII Congreso Anual de la Sociedad Española de Ingeniería Biomédica (CASEIB), s.p., 2010.

BIBLIOGRAPHY

Abella, M., Alessio, A.M., Mankoff, D.A., MacDonald, L.R., Vaquero, J.J., Desco, M., Kinahan, P.E., 2012. Accuracy of CT-based attenuation correction in PET/CT bone imaging. *Physics in Medicine and Biology* 57, 2477–2490.

Abushab, K.M., Herraiz, J.L., Vicente, E., Cal-González, J., España, S., Vaquero, J.J., Jakoby, B.W., Udías, J.M., 2012. PeneloPET simulations of the Biograph PET scanner: validation and performance investigations. *IEEE Transactions on Nuclear Science* (submitted).

Abushab, K.M., Herraiz, J.L., Vicente, E., Espana, S., Vaquero, J.J., Jakoby, B.W., Udias, J.M., 2011. PeneloPET simulations of the Biograph ToF clinical PET scanner, in: *Nuclear Science Symposium and Medical Imaging Conference*, 2011., Conference Record of the 2011 IEEE. pp. 4420 –4428.

Agostinelli, S., Allison, J., Amako, K., Apostolakis, J., Araujo, H., et al., 2003. GEANT4- a simulation toolkit. *Nuclear Instruments and Methods in Physics Research Section A*: Accelerators, Spectrometers, Detectors and associated equipment 506, 250–303.

Alessio, A., Sauer, K., Bouman, C.A., 2003. MAP Reconstruction From Spatially Correlated PET Data. *IEEE Transactions on Nuclear Science* 50, 1445–1451.

Allemand, R., Gresset, C., Vacher, J., 1980. Potential advantages of a cesium fluoride scintillator for a time-of-flight positron camera. Journal of Nuclear Medicine 21, 153–155.

Andreo, P., 1991. Monte Carlo techniques in medical radiation physics. *Physics in Medicine and Biology* 36, 861.

Assié, K., Breton, V., Buvat, I., Comtat, C., Jan, S., Krieguer, M., Lazaro, D., Morel, C., Rey, M., Santin, G., Simon, L., Staelens, S., Strul, D., Vieira, J.-M., Walle, R.V. de, 2004. Monte Carlo simulation in PET and SPECT instrumentation using GATE. *Nuclear Instruments and Methods in Physics Research Section A*: Accelerators, Spectrometers, Detectors and Associated Equipment 527, 180–189.

Ay, M.R., Zaidi, H., 2006. Assessment of errors caused by X-ray scatter and use of contrast medium when using CT-based attenuation correction in PET. *European Jurunal of Nuclear Medicine and Molecular Imaging* 33, 1301–1313.

Badawi, R.D., Kohlmyer, S.G., Harrison, R.L., Vannoy, S.D., Lewellen, T.K., 2000. The effect of camera geometry on singles flux, scatter fraction and trues and randoms sensitivity for cylindrical 3D PET-a simulation study. *IEEE Transactions on Nuclear Science* 47, 1228–1232.

Badawi, R.D., Marsden, P.K., 1999. Developments in component-based normalization for 3D PET. *Physics in medicine and biology* 44, 571.

Badawi, R.D., Marsden, P.K., Cronin, B.F., Sutcliffe, J.L., Maisey, M.N., 1996. Optimization of noise-equivalent count rates in 3D PET. *Physics in medicine and biology* 41, 1755.

Bailey, D.L., 1998. Quantitative procedures in 3D PET, in: *The Theory and Practice of 3D PET*. ed: Kluwer Academic, p. 77.

Bailey, D.L., 2005a. *Positron Emission Tomography*: Basic Sciences. Springer.

Bailey, D.L., 2005b. Data Acquisition and Performance Characterization in PET, in: Bailey, D.L., Townsend, D.W., Valk, P.E., Maisey, M.N. (Eds.), *Positron Emission Tomography*. Springer London, pp. 41–62.

Bal, G., Vandenberghe, S., Charron, M., 2006. Coincidence imaging, in: Charron, M. (Ed.), *Pediatric PET Imaging*. Springer New York, New York, NY, pp. 135–171.

Baro, J., Sempau, J., Fernández-Varea, J.M., Salvat, F., 1995. PENELOPE: an algorithm for Monte Carlo simulation of the penetration and energy loss of electrons and positrons in matter. *Nuclear Instruments and Methods in Physics Research Section B*: Beam Interactions with Materials and Atoms 100, 31–46.

Barrett, H.H., 1990. Objective assessment of image quality: effects of quantum noise and object variability. *Journal of the Optical Society of America*. A 7, 1266–1278.

Barrett, H.H., Wilson, D.W., Tsui, B.M.W., 1999. Noise properties of the EM algorithm. I. Theory. *Physics in medicine and biology* 39, 833.

Bendriem, B., Townsend, D.W., 1998. The Theory and Practice of 3D Pet. Springer.

Berko, S., Hereford, F.L., 1956. Experimental studies of positron interactions in solids and liquids. *Reviews of Modern Physics* 28, 299–307.

Bettinardi, V., Pagani, E., Gilardi, M.C., Alenius, S., Thielemans, K., Teras, M., Fazio, F., 2002. Implementation and evaluation of a 3D one-step late reconstruction algorithm for 3D positron emission tomography brain studies using median root prior. *European Jurunal of Nuclear Medicine and Molecular Imaging* 29, 7–18.

Bettinardi, V., Presotto, L., Rapisarda, E., Picchio, M., Gianolli, L., Gilardi, M.C., 2011. Physical Performance of the new hybrid PET/CT discovery-690. *Medical Physics* 38, 5394–5411.

Biemond, J., Lagendijk, R.L., Mersereau, R.M., 1990. Iterative methods for image deblurring. *Proceedings of the IEEE* 78, 856–883.

Boellaard, R., Van Lingen, A., Lammertsma, A.A., 2001. Experimental and clinical evaluation of iterative reconstruction (OSEM) in dynamic PET: quantitative characteristics and effects on kinetic modeling. *Journal of Nuclear Medicine* 42, 808–817.

Braem, A., Llatas, M.C., Chesi, E., Correia, J.G., Garibaldi, F., Joram, C., Mathot, S., Nappi, E., Silva, M.R. da, Schoenahl, F., Séguinot, J., Weilhammer, P., Zaidi, H., 2004. Feasibility of a novel design of high resolution parallax-free Compton enhanced PET scanner dedicated to brain research. *Physics in Medicine and Biology* 49, 2547–2562.

Briesmeister, J.F., 1993. MCNP 4 A, Monte Carlo code for N-particle transport system. New Mexico, Los Alamos National Laboratory.

Brooks, R.A., Di Chiro, G., 1976. Principles of computer assisted tomography (CAT) in radiographic and radioisotopic imaging. *Physics in Medicine and Biology* 21, 689–732.

Brun, R., Rademakers, F., 1997. ROOT—an object oriented data analysis framework. *Nuclear Instruments and Methods in Physics Research Section A*: accelerators, spectrometers, detectors and associated equipment 389, 81–86.

Budinger, T.F., 1983. Time-of-flight positron emission tomography: status relative to conventional PET. *Journal of nuclear medicine* 24, 73–78.

Buvat, I., Castiglioni, I., 2002. Monte Carlo simulations in SPET and PET. *The Quarterly Journal of Nuclear Medicine* 46, 48–61.

Buvat, I., Lazaro, D., 2006. Monte Carlo simulations in emission tomography and GATE: An overview. *Nuclear Instruments and Methods in Physics Research Section A*: Accelerators, Spectrometers, Detectors and Associated Equipment 569, 323–329.

Byrne, C., 2001. Likelihood maximization for list-mode emission tomographic image reconstruction. *IEEE Transactions on Medical Imaging* 20, 1084–1092.

Cal-González, J., 2010. Aplicación de simulaciones Monte Carlo para el análisis de información CT y su uso en PET y Dosimetría. Master dissertation, Madrid, Universidad Complutense de Madrid.

Cal-Gonzalez, J., Herraiz, J.J., España, S., Corzo, P.M.G., Vaquero, J.J., Desco, M., Udías, J.M., 2012. Positron range estimations: PeneloPET simulations and results. *Physics in Medicine and Biology*.

Cal-González, J., Herraiz, J.L., España, S., Desco, M., Vaquero, J.J., Udías, J.M., 2009.

Positron range effects in high resolution 3D PET imaging, in: *Nuclear Science Symposium Conference Record (NSS/MIC)*, 2009 IEEE. pp. 2788–2791.

Cal-González, J., Herraiz, J.L., España, S., Vicente, E., Herranz, E., Desco, M., Vaquero, J.J., Udías, J.M., 2011. Study of CT-based positron range correction in high resolution 3D PET imaging. *Nuclear Instruments and Methods in Physics Research Section A*: Accelerators, Spectrometers, Detectors and Associated Equipment 648, S172–S175.

Carney, J.P.J., Townsend, D.W., 2006. Clinical count rate performance of an LSO PET/CT scanner utilizing a new front-end electronics architecture with sub-nanosecond intrinsic timing resolution. *Radiation Physics and Chemistry* 75, 2182–2185.

Casey, M.E., Nutt, R., 1986. A multicrystal two dimensional BGO detector system for positron emission tomography. *IEEE Transactions on Nuclear Science* 33, 460–463.

Casey,, M.E., Gadagkar,, H., Newport, D., 1996. A component based method for normalization in volume PET. Presented at the Three-Dimensional Image Reconstruction in Radiology and Nuclear Medicine, GRANGEAT, P. & AMANS, J. L., eds, Aix-Les-Bains, France. Kluwer Academic, pp. 66–71.

Cherry, S.R., Dahlbom, M., Cherry, S., Dahlbom, M., 2006. PET: physics, instrumentation, and Scanners, in: Phelps, M.E. (Ed.), PET. Springer New York, pp. 1–117.

Cherry, S.R., Huang, S.C., 1995. Effects of scatter on model parameter estimates in 3D PET studies of the human brain. *IEEE Transactions on Nuclear Science* 42, 1174–1179.

Cherry, S.R., Sorenson, J.A., Phelps, M.E., 2003. *Physics in Nuclear Medicine*, 3rd revised edition. ed. Saunders (W.B.) Co Ltd.

Cho, Z.H., Ahn, I., Bohm, C., Huth, G., 1974. Computerized image reconstruction methods with multiple photon/x-ray transmission scanning. *Physics in Medicine and Biology* 19, 511–522.

Conti, M., 2011. Why is TOF PET reconstruction a more robust method in the presence of inconsistent data? *Physics in Medicine and Biology* 56, 155–168.

Conti, M., Bendriem, B., Casey, M., Chen, M., Kehren, F., Michel, C., Panin, V., 2005. First experimental results of time-of-flight reconstruction on an LSO PET scanner. *Physics in medicine and biology* 50, 4507.

Conti, M., Eriksson, L., Westerwoudt, V., 2011. Estimating image quality for future generations of TOF PET scanners. Presented at the 2011 IEEE Nuclear Science Symposium and Medical Imaging Conference (NSS/MIC), pp. 2407 –2414.

Cooke, B.E., Evans, A.C., Fanthome, E.O., Alarie, R., Sendyk, A.M., 1984. Performance figures and images from the Therascan 3128 positron emission tomograph. *IEEE Transactions on Nuclear Science* 31, 640–644.

Couturier, O., Luxen, A., Chatal, J.-F., Vuillez, J.-P., Rigo, P., Hustinx, R., 2004. Fluorinated tracers for imaging cancer with positron emission tomography. *European Journal of Nuclear Medicine and Molecular Imaging* 31, 1182–1206.

Cui, J., Pratx, G., Prevrhal, S., Levin, C.S., 2011. Fully 3D list-mode time-of-flight PET image reconstruction on GPUs using CUDA. *Medical Physics* 38, 6775.

Damiano, C., 2011. Understanding hadronic gamma-ray emission from supernova remnants. *Journal of Cosmology and Astroparticle Physics* 2011, 026.

Defrise, M., Gullberg, G.T., 2006. Image reconstruction. *Physics in Medicine and Biology* 51, R139–R154.

Defrise, M., Kinahan, P.E., Michel, C.J., 2005. Image reconstruction algorithms in PET, in: Bailey, D.L., Townsend, D.W., Valk, P.E., Maisey, M.N. (Eds.), Positron Emission Tomography. Springer-Verlag, London, pp. 63–91.

Defrise, M., Panin, V., Casey, M.E., 2011. New consistency equation for time-of-flight PET. Presented at the 2011 I*EEE Nuclear Science Symposium and Medical Imaging*

Conference (NSS/MIC), pp. 4115 –4120.

Derenzo, S., 1979. measurement of annihilation point spread distribution for medically important positron emitters. Presented at the 5th Int. Conf. of Positron Annihilation, Lake Yamanaka, Japan, pp. 819–23.

Derenzo, S.E., 1986. Mathematical removal of positron range blurring in high resolution tomography. *IEEE Transactions on Nuclear Science* 33, 565–569.

El Fakhri, G., Surti, S., Trott, C.M., Scheuermann, J., Karp, J.S., 2011. Improvement in lesion detection with whole-body oncologic time-of-flight PET. *Journal of Nuclear Medicine* 52, 347–353.

Eriksson, L., Townsend, D., Conti, M., Eriksson, M., Rothfuss, H., Schmand, M., Casey, M.E., Bendriem, B., 2007. An investigation of sensitivity limits in PET scanners. *Nuclear Instruments and Methods in Physics Research Section A*: Accelerators, Spectrometers, Detectors and Associated Equipment 580, 836–842.

Eriksson, L., Townsend, D., Eriksson, M., Casey, M.E., Conti, M., Bendriem, B., Nutt, R., 2004. The NEC dependence of different scintillators for positron emission tomography, in: *Nuclear Science Symposium Conference Record, 2004 IEEE*. pp. 3785–3788.

España, S., 2009. Simulaciones avanzadas aplicadas al diseño de escáneres y mejora de la calidad de imagen en tomografía por emisión de positrones. Doctoral dissertation, Madrid, Universidad Complutense de Madrid.

España, S., Fraile, L.M., Heraiz, J.L., Udías, J.M., Desco, M., Vaquero, J.J., 2010. Performance evaluation of SiPM photodetectors for PET imaging in the presence of magnetic fields. *Nuclear Instruments and Methods in Physics Research Section A*: Accelerators, Spectrometers, Detectors and Associated Equipment 613, 308–316.

España, S., Herraiz, J.L., Vicente, E., Vaquero, J.J., Desco, M., Udias, J.M., 2009. PeneloPET, a Monte Carlo PET simulation tool based on PENELOPE: features and validation. *Physics in Medicine and Biology* 54, 1723–1742.

Fahey, F.H., 2002. Data acquisition in PET imaging. *Jounoral of nuclear medicine Technology* 30, 39–49.

Ferreira, N.C., Trebossen, R., Bendriem, B., 1998. Assessment of 3-D PET quantitation: influence of out of the field of view radioactive sources and of attenuating media. *IEEE Transactions* on *Nuclear Science* 45, 1670–1675.

Ferreira, N.C., Trebossen, R., Lartizien, C., Brulon, V., Merceron, P., Bendriem, B., 2002. A hybrid scatter correction for 3D PET based on an estimation of the distribution of unscattered coincidences: implementation on the ECAT EXACT HR+. *Physics in medicine and biology* 47, 1555.

Frese, T., Rouze, N.C., Bouman, C.A., Sauer, K., Hutchins, G.D., 2003. Quantitative comparison of FBP, EM, and bayesian reconstruction algorithms for the indyPET scanner. *IEEE Transactions on Medical Imaging* 22, 258–276.

Fu, L., Qi, J., 2008. A novel iterative image reconstruction method for high-resolution PET Imaging with a Monte Carlo based positron range model, in: *Nuclear Science Symposium Conference Record*, 2008. NSS'08. IEEE. pp. 3609–3612.

Gaitanis, A., Kontaxakis, G., Spyrou, G., Panayiotakis, G., Tzanakos, G., 2010. PET image reconstruction: A stopping rule for the MLEM algorithm based on properties of the updating coefficients. *Computerized Medical Imaging and Graphics* 34, 131–141.

General-Purpose Computing on Graphics Processing Units repository, 2010. available: www.gpgpu.org.

Goertzen, A.L., Bao, Q., Bergeron, M., Blankemeyer, E., Blinder, S., Cañadas, M., Chatziioannou, A.F., Dinelle, K., Elhami, E., Jans, H.-S., Lage, E., Lecomte, R., Sossi, V., Surti, S., Tai, Y.-C., Vaquero, J.J., Vicente, E., Williams, D.A., Laforest, R., 2012. NEMA NU 4-2008 Comparison of Preclinical PET Imaging Systems. *Journal of*

Nuclear Medicine, 53 (8), pp. 1300–9.

Green, P.J., 1990. Bayesian reconstructions from emission tomography data using a modified EM algorithm. *IEEE Transactions on Medical Imaging* 9, 84–93.

Grootoonk, S., Spinks, T.J., Sashin, D., Spyrou, N.M., Jones, T., 1996. Correction for scatter in 3D brain PET using a dual energy window method. *Physics in Medicine and Biology* 41, 2757.

Guhlke, S., Verbruggen, A.M., Vallabhajosula, S., 2007. Radiochemistry and Radiopharmacy, in: Biersack, H.-J., Freeman, L.M. (Eds.), *Clinical Nuclear Medicine*. Springer Berlin Heidelberg, Berlin, Heidelberg, pp. 34–76.

Harrison, R.L., Dhavala, S., Kumar, P.N., Shao, Y., Manjersshwar, R., Lewellen, T.K., Jansen, F.P., 2002. Acceleration of SimSET photon history generation, in: *Nuclear Science Symposium Conference Record*, 2002 IEEE. pp. 1835–1838.

Harrison, R.L., Gillispie, S.B., Alessio, A.M., Kinahan, P.E., Lewellen, T.K., 2005. The effects of object size, attenuation, scatter, and random coincidences on signal to noise ratio in simulations of time-of-flight positron emission tomography, in: *Nuclear Science Symposium Conference Record*, 2005 IEEE. p. 5–pp.

Harrison, R.L., Vannoy, S.D., Haynor, D.R., Gillispie, S.B., Kaplan, M.S., Lewellen, T.K., 1993. Preliminary experience with the photon history generator module of a public-domain simulation system for emission tomography, in: *Nuclear Science Symposium and Medical Imaging Conference*, 1993., 1993 IEEE Conference Record. pp. 1154–1158.

Hasegawa, T., Michei, C., Kawashima, K., Murayama, H., Nakajima, T., Matsuura, H., Wada, Y., 2000. A study of external end-shields for PET. *IEEE Transactions on Nuclear Science* 47, 1099–1103.

Heinrichs, U., Pietrzyk, U., Ziemons, K., 2003. Design optimization of the PMT-ClearPET prototypes based on simulation studies with GEANT3. *IEEE Transactions on Nuclear Science* 50, 1428–1432.

Henkin, R.E., Bova, D., Dillehay, G.L., Karesh, S.M., 2006. Nuclear Medicine. Elsevier Health Sciences, Philadelphia.

Herraiz, J.L., 2008. Técnicas avanzadas de reconstrucción de imagen nuclear PET, X-CT y SPECT, Master dissertation, Madrid, Universidad Complutense de Madrid.

Herraiz, J.L., España, S., Cal-Gonzálex, J., Vaquero, J.J., Desco, M., Udías, J.M., 2011. Fully 3D GPU PET reconstruction. *Nuclear Instruments and Methods in Physics Research Section A*: Accelerators, Spectrometers, Detectors and Associated Equipment 648, S169–S171.

Herraiz, J.L., España, S., Vaquero, J.., Desco, M., Udias, J.M., 2006. FIRST: Fast Iterative Reconstruction Software for (PET) tomography. *Physics in Medicine and Biology* 51, 4547–4565.

Herraiz, J.L., España, S., Vicente, E., Herranz, E., Desco, M., Vaquero, J.J., Udias, J., 2008. Frequency selective signal extrapolation for compensation of missing data in sinograms, in: *Nuclear Science Symposium Conference Record*, 2008. NSS'08. IEEE. pp. 4299–4302.

Herraiz, J.L., Espana, S., Vicente, E., Herranz, E., Vaquero, J.J., Desco, M., Udias, J.M., 2007. Revised consistency conditions for PET data. Presented at the *IEEE Nuclear Science Symposium Conference Record*, 2007. NSS '07, pp. 3865 –3870.

Herraiz, J.L., Espana, S., Vicente, E., Vaquero, J.J., Desco, M., Udias, J.M., 2006c. Optimal and Robust PET Data sinogram restoration based on the response of the system. Presented at the *IEEE Nuclear Science Symposium Conference Record*, 2006, pp. 3404 –3407.

Herranz, E., 2010. Formacion de modelos dinamicos de distribucion temporal de farmacos en animales de laboratorio y contrastacion con datos adquiridos en PET. Master dissertation, Madrid, Universidad Complutense de Madrid.

Hoffman, E.J., Guerrero, T.M., Germano, G., Digby, W.M., Dahlbom, M., 1989. PET system calibrations and corrections for quantitative and spatially accurate images. *IEEE Transactions on Nuclear Science* 36, 1108–1112.

Hoffman, E.J., Huang, S.C., Phelps, M.E., Kuhl, D.E., 1981. Quantitation in positron emission computed tomography: 4. Effect of accidental coincidences. *Journal of Computer Assisted Tomography* 5, 391–400.

Hong, I.K., Chung, S.T., Kim, H.K., Kim, Y.B., Son, Y.D., Cho, Z.H., 2007. Ultra Fast Symmetry and SIMD-based projection-backprojection (SSP) algorithm for 3-D PET image reconstruction. *IEEE Transactions on Medical Imaging* 26, 789–803.

Huang, S.-C., Hoffman, E., Phelps, M., Kuhl, D., 1979. Quantitation in Positron Emission Computed Tomography: 2. Effects of inaccurate attenuation correction. *Journal of Computer Assisted Tomography* 3.

Hudson, H.M., Larkin, R.S., 1994. Accelerated image reconstruction using ordered subsets of projection data. *IEEE Transactions on Medical Imaging* 13, 601 –609.

Humm, J.L., Rosenfeld, A., Del Guerra, A., 2003. From PET detectors to PET scanners. *European Journal of Nuclear Medicine and Molecular Imaging* 30, 1574–1597.

Jakoby, B.W., Bercier, Y., Conti, M., Casey, M., Gremillion, T., Hayden, C., Bendriem, B., Townsend, D.W., 2008. Performance investigation of a time-of-flight PET/CT scanner, in: *Nuclear Science Symposium Conference Record*, 2008. NSS'08. IEEE. pp. 3738–3743.

Jakoby, B.W., Bercier, Y., Conti, M., Casey, M.E., Bendriem, B., Townsend, D.W., 2011. Physical and clinical performance of the mCT time-of-flight PET/CT scanner. *Physics in Medicine and Biology* 56, 2375–2389.

Jakoby, B.W., Bercier, Y., Watson, C.C., Bendriem, B., Townsend, D.W., 2009. Performance Characteristics of a New LSO PET/CT Scanner With Extended Axial Field-of-View and PSF Reconstruction. *IEEE Transactions on Nuclear Science* 56 633–639.

Jakoby, W.B., Schaefferkoetter, J.D., Conti, M., Spyrou, N.M., Townsend, D.W., 2012. An Assessment of Time of Flight Positron Emission Tomography. Australian Neuroscience Society (ANS) conference, Australia.

Jan, S., Comtat, C., Strul, D., Santin, G., Trebossen, R., 2005. Monte Carlo simulation for the ECAT EXACT HR+ system using GATE. *IEEE Transactions on Nuclear Science* 52, 627–633.

Jan, S., Santin, G., Strul, D., Staelens, S., Assie, K., Autret, D., Avner, S., Barbier, R., Bardies, M., Bloomfield, P.M., others, 2004. GATE: a simulation toolkit for PET and SPECT. *Physics in medicine and biology* 49, 4543.

Johnson, V.E., 1994. A note on stopping rules in EM-ML reconstructions of ECT images. *IEEE Transactions on Medical Imaging* 13, 569–571.

Jones, M.D., Yao, R., 2004. Parallel programming for OSEM reconstruction with MPI, openMP, and hybrid MPI-openMP, in: *Nuclear Science Symposium Conference Record*, 2004 IEEE. pp. 3036–3042.

Joung, J., Miyaoka, R.S., Lewellen, T., K..., 2004. cMiCE:a high resolution animal PET using continuous LSO with a statistics based positioning scheme, in: *Nuclear Science Symposium Conference Record*, 2004 IEEE. pp. 1137–1141.

Kadrmas, D.J., 2004. LOR-OSEM: statistical PET reconstruction from raw line-of-response histograms. *Physics in Medicine and Biology* 49, 4731–4744.

Kadrmas, D.J., Casey, M.E., Conti, M., Jakoby, B.W., Lois, C., Townsend, D.W., 2009. Impact of time-of-flight on PET tumor detection. *Journal of Nuclear Medicine* 50, 1315–1323.

Karp, J.S., Muehllehner, G., Lewitt, R.M., 1988. Constrained Fourier space method for compensation of missing data in emission computed tomography. *IEEE Transactions on Medical Imaging 7,* 21–25.

Karp, J.S., Muehllehner, G., MankofF, D.A., Ordonez, C.E., Ollinger, J.M., Daube-Witherspoon, M.E., Haigh, A.T., Beerbohm, D.J., 1990. Continuous-slice PENN-PET: a positron tomograph with volume imaging capability. *Journal of Nuclear Medicine* 31, 617–627.

Karp, J.S., Surti, S., Daube-Witherspoon, M.E., Muehllehner, G., 2008. Benefit of time-of-flight in PET: experimental and clinical results. *Journal of Nuclear Medicine* 49, 462–470.

Kawrakow, I., Bielajew, A.F., 1998. On the condensed history technique for electron transport. *Nuclear Instruments and Methods in Physics Research Section B*: Beam Interactions with Materials and Atoms 142, 253–280.

Khalil, M.M., 2010. Basic Sciences of Nuclear Medicine. Springer.

Kinahan, P.E., Hasegawa, B.H., Beyer, T., 2003. X-ray-based attenuation correction for positron emission tomography/computed tomography scanners, in: *Seminars in Nuclear Medicine*. pp. 166–179.

Knoll, G.F., 2000. Radiation Detection and Measurement, 3rd ed. Wiley.

Krane, K.S., 1987. Introductory Nuclear Physics, 3rd ed. Wiley, New York.

Kubota, K., 2001. From tumor biology to clinical Pet: a review of positron emission tomography (PET) in oncology. *Annual of Nuclear Medicine* 15, 471–486.

Kuhn, A., Surti, S., Karp, J.S., Raby, P.S., Shah, K.S., Perkins, A.E., Muehllehner, G., 2004. Design of a lanthanum bromide detector for time-of-flight PET. *IEEE Transactions on Nuclear Science* 51, 2550–2557.

Kunze, W.-D., Baehre, M., Richter, E., 2000. PET with a dual-head coincidence camera: spatial resolution, scatter fraction, and sensitivity. *Journal of Nuclear Medicine* 41, 1067–1074.

Larson, S.M., Schwartz, L.H., 2006. ^{18}F-FDG PET as a candidate for “qualified biomarker”: functional assessment of treatment response in oncology. *Journal of Nuclear Medicine* 47, 901–903.

Lartizien, C., Kinahan, P.E., Swensson, R., Comtat, C., Lin, M., Villemagne, V., Trébossen, R., 2003. Evaluating image reconstruction methods for tumor detection in 3-dimensional whole-body PET oncology imaging. *Journal of Nuclear Medicine* 44, 276–290.

Lee, J., Vaquero, J.J., Kriens, M., Barbosa, F.J., Seidel, J., Green, M.V., 2000. High performance phoswich detector module for small animal PET. *Journal of Nuclear Medicine* 41, 19.

Levin, C., 1995. Chap. Basic physics of radionuclide imaging, in: Emission Tomography (the fundamentals of PET and SPECT). Elsevier, USA, pp. 53–88.

Levin, C.S., Foudray, A.M.K., Habte, F., 2006. Impact of high energy resolution detectors on the performance of a PET system dedicated to breast cancer imaging. *Physica Medica* 21 Suppl 1, 28–34.

Levin, C.S., Hoffman, E.J., 1999. Calculation of positron range and its effect on the fundamental limit of positron emission tomography system spatial resolution. *Physics in Medicine and Biology* 44, 781.

Lewellen, T.K., 1998. Time-of-flight PET, in: *Seminars in Nuclear Medicine*. pp. 268–275.

Lewellen, T.K., 2008. Recent developments in PET detector technology. *Physics in Medicine and Biology* 53, R287–R317.

Lewitt, R.M., Muehllehner, G., Karp, J.S., 1994. Three-dimensional image reconstruction for PET by multi-slice rebinning and axial image filtering. *Physics in Medicine and Biology* 39, 321–339.

Liow, J.S., Strother, S.C., 1991. Practical tradeoffs between noise, quantitation, and number of iterations for maximum likelihood-based reconstructions. *IEEE Transactions on Medical Imaging* 10, 563–571.

Ljungberg, M., 1998. Monte Carlo calculations in nuclear medicine: applications in diagnostic imaging, First Edition. CRC Press.

Ljungberg, M., Strand, S.-E., King, M.A., 2012. Monte Carlo calculations in nuclear medicine, Second Edition: Applications in Diagnostic Imaging. CRC Press.

Lois, C., Jakoby, B.W., Long, M.J., Hubner, K.F., Barker, D.W., Casey, M.E., Conti, M., Panin, V.Y., Kadrmas, D.J., Townsend, D.W., 2010. An assessment of the impact of incorporating time-of-flight information into clinical PET/CT imaging. *Journal of Nuclear Medicine* 51, 237–245.

MacDonald, L.R., Schmitz, R.E., Alessio, A.M., Wollenweber, S.D., Stearns, C.W., Ganin, A., Harrison, R.L., Lewellen, T.K., Kinahan, P.E., 2008. Measured count-rate performance of the discovery STE PET/CT scanner in 2D, 3D and partial collimation acquisition modes. *Physics in Medicine and Biology* 53, 3723.

Mair, B.A., Carroll, R.B., Anderson, J.M.M., 1996. Filter banks and the EM algorithm, in: *Nuclear Science Symposium*, 1996. Conference Record, 1996 IEEE. pp. 1747–1751.

Manjeshwar, R.M., Shao, Y., Jansen, F.P., 2005. Image quality improvements with time-of-flight positron emission tomography for molecular imaging, in: Acoustics, Speech, and Signal Processing, 2005. Proceedings.(ICASSP'05). *IEEE International Conference* on. pp. v–853.

Meikle, S.R., Badawi, R.D., 2005. Quantitative techniques in PET, in: Bailey, D.L., Townsend, D.W., Valk, P.E., Maisey, M.N. (Eds.), Positron Emission Tomography. Springer London, pp. 93–126.

Melcher, C.L., 2000. Scintillation crystals for PET. *Journal of Nuclear Medicine*. 41, 1051–1055.

Melcher, C.L., Schweitzer, J.S., 1991. Cerium-doped lutetium oxyorthosilicate: a fast, efficient new scintillator, in: Nuclear Science Symposium and Medical Imaging Conference, 1991., *Conference Record of the 1991 IEEE*. pp. 228–231.

Meyer, M.A., Aliberti, S., Grignani, G., Aglietta, M., Juweid, M.E., Cheson, B.D., 2006. Positron-emission tomography in cancer therapy. *New England Journal of Medicine* 354, 1958–1960.

Mollet, P., Keereman, V., Vandenberghe, S., 2011. Experimental evaluation of simultaneous emission and transmission imaging using TOF information. Presented at the 2011 *IEEE Nuclear Science Symposium and Medical Imaging Conference (NSS/MIC),* pp. 2976 –2980.

Moses, W.W., 2003. Time of flight in pet revisited. *IEEE Transactions on Nuclear Science* 50, 1325–1330.

Moses, W.W., Derenzo, S.E., 1999. Prospects for time-of-flight PET using LSO scintillator. *IEEE Transactions on Nuclear Science* 46, 474–478.

Moses, W.W., Ullisch, M., 2006. Factors influencing timing resolution in a commercial LSO PET camera. *IEEE Transactions on Nuclear Science* 53, 78–85.

Moszynski, M., Kapusta, M., Nassalski, A., Szczesniak, T., Wolski, D., Eriksson, L., Melcher, C.L., 2006. New Prospects for Time-of-Flight PET With LSO Scintillators. *IEEE Transactions on Nuclear Science* 53, 2484–2488.

Mullani, N.A., Ficke, D.C., Hartz, R., Markham, J., Wong, G., 1981. System design of fast PET scanners utilizing time-of-flight. *IEEE Transactions on Nuclear Science* 28, 104–108.

Mumcuoglu, E.Ü., Leahy, R.M., Cherry, S.R., 1996. Bayesian reconstruction of PET images: methodology and performance analysis. *Physics in Medicine and Biology* 41, 1777–1807.

Muzic, R.F., Kolthammer, J.A., 2006. PET Performance of the GEMINI TF: A Time-of-flight PET/CT Scanner in: *Nuclear Science Symposium Conference Record, 2006 IEEE.* pp. 1940–1944.

NEMA, 2007. National Electrical Manufacturers Association. NEMA standards publication NU 2-2007, Rosslyn,VA,.

Nuyts, J., Fessler, J.A., 2002. Comparison between post-smoothed maximum-likelihood and penalized-likelihood for image reconstruction with uniform spatial resolution, in: *Nuclear Science Symposium Conference Record, 2002 IEEE*. pp. 895–899.

NVIDIA CUDA Programming Guide v.2.5.0, n.d. (Online) available http://developer.nvidia.com/object/gpu_programming_guide.html. (September) 2010.

Oliver, J.F., Rafecas, M., 2008. Revisiting the singles rate method for modeling accidental coincidences in PET, in: *Nuclear Science Symposium Conference Record, 2008. NSS'08. IEEE*. pp. 4288–4291.

Oliver, J.F., Rafecas, M., 2010. Improving the singles rate method for modeling accidental coincidences in high-resolution PET. *Physics in Medicine and Biology* 55, 6951–6971.

Ollinger, J.M., 1995. Detector efficiency and compton scatter in fully 3D PET. *IEEE Transactions on Nuclear Science* 42, 1168–1173.

Ollinger, J.M., Fessler, J.A., 1997. Positron-emission tomography. *Signal Processing Magazine, IEEE* 14, 43–55.

Ortuño, J.E., Guerra-Gutiérrez, P., Rubio, J.L., Kontaxakis, G., Santos, A., 2006. 3D-OSEM iterative image reconstruction for high-resolution PET using precalculated system matrix. *Nuclear Instruments and Methods in Physics Research A* 569, 440–444.

Palmer, M.R., Xuping Zhu, Parker, J.A., 2005. Modeling and simulation of positron range effects for high resolution PET imaging. *IEEE Transactions on Nuclear Science* 52, 1391–1395.

Panettieri, V., Wennberg, B., Gagliardi, G., Duch, M.A., Ginjaume, M., Lax, I., 2007. SBRT of lung tumours: Monte Carlo simulation with PENELOPE of dose distributions including respiratory motion and comparison with different treatment planning systems. *Physics in Medicine and Biology* 52, 4265–4281.

Parra, L., Barrett, H.H., 1998. List-mode likelihood: EM algorithm and image quality estimation demonstrated on 2-D PET. *IEEE Transactions on Medical Imaging* 17, 228–235.

Phelps, M.E., 2006. Pet: Physics, Instrumentation, and Scanners. Springer.

Powsner, R.A., Powsner, E.R. (Eds.), 2008. Essential Nuclear Medicine Physics, Second Edition.

Pratx, G., Chinn, G., Olcott, P.D., Levin, C.S., 2009. Fast, accurate and shift-varying line projections for iterative reconstruction using the GPU. *IEEE Transactions on Medical Imaging* 28, 435–445.

Qi, J., Leahy, R.M., Cherry, S.R., Chatziioannou, A., Farquhar, T.H., 1998. High-resolution 3D Bayesian image reconstruction using the microPET small-animal scanner. *Physics in Medicine and Biology* 43, 1001–1013.

Rafecas, M., Mosler, B., Dietz, M., Pogl, M., Stamatakis, A., McElroy, D.P., Ziegler, S.I., 2004. Use of a Monte Carlo-based probability matrix for 3-D iterative reconstruction of MADPET-II data. *IEEE Transactions on Nuclear Science* 51, 2597–2605.

Reader, A.J., Ally, S., Bakatselos, F., Manavaki, R., Walledge, R.J., Jeavons, A.P., Julyan, P.J., Zhao, S., Hastings, D.L., Zweit, J., 2002. One-pass list-mode EM algorithm for high-resolution 3-D PET image reconstruction into large arrays. *IEEE Transactions on Nuclear Science* 49, 693–699.

Riddell, C., Carson, R.E., Carrasquillo, J.A., Libutti, S.K., Danforth, D.N., Whatley, M., Bacharach, S.L., 2001. Noise reduction in oncology FDG PET images by iterative reconstruction: a quantitative assessment. *Journal of Nuclear Medicine*. 42, 1316–1323.

Rogers, D.W.O., 2006. Fifty years of Monte Carlo simulations for medical physics. *Physics in Medicine and Biology* 51, R287–301.

Rose, A., 1973. Vision: human and electronic. Plenum Press.

Saha, G.B., 2010. Basics of PET Imaging: Physics, Chemistry, and Regulations. Springer.

Salvat, F., Fernandez-varea, D., Sempau, J., 2006. PENELOPE-2006: A code system for Monte Carlo simulation of electron and photon transport. Available on line "https://www.oecd-nea.org/science/pubs/2006/nea6222-penelope.pdf".

Salvat, F., Fernandez-varea, D., Sempau, J., 2008. PENELOPE-2008: A code system for Monte Carlo simulation of electron and photon transport. Available on line "http://www.oecd-nea.org/science/pubs/2009/nea6416-penelope.pdf".

Sánchez-Crespo, A., Larsson, S.A., 2006. The influence of photon depth of interaction and non-collinear spread of annihilation photons on PET image spatial resolution. *European Journal of Nuclear Medicine and Molecular Imaging* 33, 940–947.

Sanders, J., Kandrot, E., 2010. CUDA by example: an introduction to general-purpose GPU programming, 1st ed. Addison-Wesley Professional.

Schaart, D.R., Van Dam, H.T., Seifert, S., Vinke, R., Dendooven, P., Löhner, H., Beekman, F.J., 2009. A novel, SiPM-array-based, monolithic scintillator detector for PET. *Physics in Medicine and Biology* 54, 3501–3512.

Schiepers, C., Nuyts, J., Wu, H.M., Verma, R.C., 1997. PET with< sup> 18</sup> F-fluoride: effects of interative versus filtered backprojection reconstruction on kinetic modeling. *IEEE Transactions on Nuclear Science* 44, 1591–1593.

Schmidtlein, C.R., Kirov, A.S., Nehmeh, S.A., Erdi, Y.E., Humm, J.L., Amols, H.I., Bidaut, L.M., Ganin, A., Stearns, C.W., McDaniel, D.L., Hamacher, K.A., 2006. Validation of GATE Monte Carlo simulations of the GE Advance/Discovery LS PET scanners. *Medical Physics* 33, 198.

Segars, W.P., Mahesh, M., Beck, T.J., Frey, E.C., Tsui, B.M.W., 2008. Realistic CT simulation using the 4D XCAT phantom. *Medical Physics* 35, 3800–3808.

Sempau, J., Andreo, P., 2006. Configuration of the electron transport algorithm of PENELOPE to simulate ion chambers. *Physics in Medicine and Biology* 51, 3533.

Shao, L., Freifelder, R., Karp, J.S., 1994. Triple energy window scatter correction technique in PET. *IEEE Transactions on Medical Imaging* 13, 641–648.

Shepp, L.A., Vardi, Y., 1982. Maximum likelihood reconstruction for emission tomography. *IEEE Transactions on Medical Imaging* 1, 113 –122.

Slijpen, E.T.P., Beekman, F.J., 1999. Comparison of post-filtering and filtering between iterations for SPECT reconstruction. *IEEE Transactions on Nuclear Science* 46, 2233–2238.

Snyder, D.L., Miller, M.I., Thomas, L.J., Politte, D.G., 1987. Noise and edge artifacts in maximum-likelihood reconstructions for emission tomography. *IEEE Transactions on Medical Imaging* 6, 228–238.

Snyder, D.L., Thomas, L.J., Ter-Pogossian, M.M., 1981. A matheematical model for Positron-Emission Tomography systems having time-of-flight measurements. *IEEE Transactions on Nuclear Science* 28, 3575–3583.

Sossi, V., Barney, J.S., Harrison, R., Ruth, T.J., 1995. Effect of scatter from radioactivity outside of the field of view in 3D PET. *IEEE Transactions on Nuclear Science* 42, 1157–1161.

Spinks, T.J., Miller, M.P., Bailey, D.L., Bloomfield, P.M., Livieratos, L., Jones, T., 1998. The effect of activity outside the direct field of view in a 3D-only whole-body positron tomograph. *Physics in Medicine and Biology* 43, 895.

Steinbach, C.O., 2011. Development of PET detector module. Doctoral dissertation, Budapest, Budapest University of Technology and Economic.

Stickel, J.R., Cherry, S.R., 2005. High-resolution PET detector design: modelling components of intrinsic spatial resolution. *Physics in Medicine and Biology 50*, 179–195.

Strother, S.C., Casey, M.E., Hoffman, E.J., 1990. Measuring PET scanner sensitivity: relating countrates to image signal-to-noise ratios using noise equivalents counts. *IEEE Transactions on Nuclear Science* 37, 783–788.

Surti, S., Karp, J.S., 2009. Experimental evaluation of a simple lesion detection task with time-of-flight PET. *Physics in Medicine and Biology* 54, 373–384.

Surti, S., Karp, J.S., Muehllehner, G., Raby, P.S., 2003. Investigation of lanthanum scintillators for 3-D PET. *IEEE Transactions on Nuclear Science* 50, 348–354.

Surti, S., Karp, S., Popescu, L.M., Daube-Witherspoon, E., Werner, M., 2006. Investigation of time-of-flight benefit for fully 3-DPET. *IEEE Transactions on Medical Imaging* 25, 529–538.

Surti, S., Kuhn, A., Werner, M.E., Perkins, A.E., Kolthammer, J., Karp, J.S., 2007. Performance of Philips Gemini TF PET/CT scanner with special consideration for its time-of-flight imaging capabilities. J*ournal of Nuclear Medicine* 48, 471–480.

Tarantola, G., Zito, F., Gerundini, P., 2003. PET instrumentation and reconstruction algorithms in whole-body applications. *Journal of Nuclear Medicine* 44, 756–769.

Thompson, C.J., 1988. The effect of collimation on scatter fraction in multi-slice PET. *IEEE Transactions on Nuclear Science* 35, 598 – 602.

Thompson, C.J., Moreno-Cantu, J., Picard, Y., 1992. PETSIM: Monte Carlo simulation of all sensitivity and resolution parameters of cylindrical positron imaging systems. *Physics in medicine and biology* 37, 731.

Tomitani, T., 1981. Image reconstruction and noise evaluation in photon time-of-flight assisted positron emission tomography. *IEEE Transactions on Nuclear Science* 28, 4581–4589.

Tong, S., Alessio, A.M., Kinahan, P.E., 2010. Noise and signal properties in PSF-based fully 3D PET image reconstruction: an experimental evaluation. *Physics in Medicine and Biology* 55, 1453–1473.

Torres-Espallardo, I., Rafecas, M., Spanoudaki, V., McElroy, D.P., Ziegler, S.I., 2008. Effect of inter-crystal scatter on estimation methods for random coincidences and subsequent correction. *Physics in Medicine and Biology* 53, 2391–2411.

Townsend, D.W., 2006. Basic science of PET and PET/CT, in: Valk, P.E., Delbeke, D., Bailey, D.L., Townsend, D.W., Maisey, M.N. (Eds.), Positron Emission Tomography. Springer London, pp. 1–16.

Tuna, U., Peltonen, S., Ruotsalainen, U., 2010. Gap-filling for the high-resolution PET sinograms with a dedicated DCT-domain filter. *IEEE Transactions on Medical Imaging* 3, 830–839.

Vaquero, J.J., Pascau, J., Molins, A., Arco, J., Desco, M., 2004. Performance characteristics of the ARGUS-drT small animal PET scanner: preliminary results. Presented at the IEEE NSS-MIC Confrence, Rome, Italy, p. (Book of Abstracts)148.

Vicente, E., 2012. Caracterización, mejora y diseño de escáneres PET preclínicos. Doctoral dissertation, Madrid, Universidad Complutense de Madrid.

Vicente, E., Herraiz, J.L., Espana, S., Herranz, E., Desco, M., Vaquero, J.J., Udias, J.M., 2011. Dead time and pile-up correction method based on the singles to coincidences ratio for PET, in: *Nuclear Science Symposium and Medical Imaging Conference (NSS/MIC)*, 2011 IEEE. pp. 2933–2935.

Vicente, E., Herraiz, J.L., España, S., Herranz, E., Desco, M., Vaquero, J.J., Udías, J.M., 2012a. Improved effective dead-time correction for PET scanners: Application to small-animal PET. *Physics in Medicine and Biology*, Submitted for publication.

Vicente, E., Herraiz,, J.L., Seidel,, j., Green, M.V., Desco, M., Vaquero, J.J., Udias, J.M., 2012b. Regularization of 3D iterative reconstruction for a limited-angle PET tomograph. presented at the Nuclear Science Symposium Conference Record, 2012 IEEE.

Vilches, M., Garcia-Pareja, S., Guerrero, R., Anguiano, M., Lallena, A.M., 2006. Monte Carlo simulation of the electron transport through thin slabs: A comparative study of PENELOPE, GEANT3, GEANT4, EGSnrc and MCNPX. arXiv:physics/0612044.

Von Schulthess, G.K., Steinert, H.C., Hany, T.F., 2006. Integrated PET/CT: Current Applications and Future Directions1. *Radiology* 238, 405–422.

Vunckx, K., Lin Zhou, Matej, S., Defrise, M., Nuyts, J., 2010. Fisher information-based evaluation of image quality for time-of-flight PET. *IEEE Transactions on Medical Imaging* 29, 311–321.

Watson, C.C., Image noise variance in 3D OSEM reconstruction of clinical time-of-flight PET in: *Nuclear Science Symposium Conference Record, 2006 IEEE*. pp. 1736–1739.

Watson, C.C., Casey, M.E., Beyer, T., Bruckbauer, T., Townsend, D.W., Brasse, D., 2003. Evaluation of clinical PET count rate performance. I*EEE Transactions on Nuclear Science* 50, 1379–1385.

Watson, C.C., Casey, M.E., Michel, C., Bendriem, B., 2004. Advances in scatter correction for 3D PET/CT, in: *Nuclear Science Symposium Conference Record, 2004 IEEE*. pp. 3008–3012.

Wernick, M.N., Aarsvold, J.N., 2004. Emission Tomography: the fundamentals of PET and SPECT. Academic Press.

Wirth, V., 1989. Effective energy resolution and scatter rejection in nuclear medicine. *Physics in Medicine and Biology* 34, 85.

Worstell, W., Kudrolli, H., Nevin, J., Rohatgi, R., Romanov, L., 2004. Diversity combining signal processing and NEC in list-mode PET, in: *Nuclear Science Symposium Conference Record, 2004 IEEE*. pp. 3814–3818.

Yamaya, T., Hagiwara, N., Obi, T., Yamaguchi, M., Kita, K., Ohyama, N., Kitamura, K., Hasegawa, T., Haneishi, H., Murayama, H., 2003. DOI-PET image reconstruction with accurate system modeling that reduces redundancy of the imaging system. *IEEE Transactions on Nuclear Science* 50, 1404–1409.

Zaidi, H., 1999. Relevance of accurate Monte Carlo modeling in nuclear medical imaging. *Medical Physics* 26, 574.

Zaidi, H., 2000. Comparative evaluation of photon cross-section libraries for materials of interest in PET Monte Carlo simulations. *IEEE Transactions on Nuclear Science* 47, 2722 –2735.

Zaidi, H., 2006. Monte Carlo modeling in nuclear medicine imaging, in: Zaidi, H. (Ed.), Quantitative Analysis in Nuclear Medicine Imaging. Kluwer Academic Publishers, Boston, pp. 358–390.

Zaidi, H., Herrmann Scheurer, A., Morel, C., 1999. An object-oriented Monte Carlo simulator for 3D cylindrical positron tomographs. *Computer Methods and Programs in Biomedicine* 58, 133–145.

Zaidi, H., Koral, K.F., 2006. Scatter correction strategies in emission tomography, in: Zaidi, H. (Ed.), Quantitative analysis in nuclear medicine imaging. Springer US, pp. 205–235.

Zaidi, H., Labbé, C., Morel, C., 1998. Implementation of an environment for Monte Carlo simulation of fully 3-D positron tomography on a high-performance parallel platform. *Parallel Computing* 24, 1523–1536.

Zaidi, H., Ojha, N., Morich, M., Griesmer, J., Hu, Z., Maniawski, P., Ratib, O., Izquierdo-Garcia, D., Fayad, Z.A., Shao, L., 2011. Design and performance evaluation of a whole-body Ingenuity TF PET–MRI system. *Physics in Medicine and Biology* 56, 3091–3106.

Zanzonico, P., 2004. Positron emission tomography: a review of basic principles, scanner design and performance, and current systems. *Seminars in Nuclear Medicine* 34, 87–111.

Zanzonico, P., Heller, S., 2007. Physics, instrumentation, and radiation protection, in: Biersack, H.-J., Freeman, L.M. (Eds.), Clinical Nuclear Medicine. Springer Berlin Heidelberg, Berlin, Heidelberg, pp. 1–33.

Zeng, G.L., Gullberg, G.T., 2000. Unmatched projector/backprojector pairs in an iterative reconstruction algorithm. *IEEE Transactions on Medical Imaging* 19, 548–555.

Resumen en castellano

Introducción y Objetivos

La tomografía por emisión de positrones (PET) es una de las técnicas de imagen molecular con mayor sensibilidad. Su mayor ventaja consiste en que permite medir la distribución de moléculas de interés en el cuerpo humano, suministradas en cantidades suficientemente pequeñas como para no afectar los procesos fisiológicos normales que se busca estudiar. Se basa en el uso de radioisótopos emisores de positrones para marcar la molécula en estudio (trazador) que se inyecta en una pequeña cantidad al paciente o animal para realizar exámenes clínicos y de investigación en vivo. El trazador suministrado se distribuye en el cuerpo siguiendo sus determinadas vías fisiológicas, y se usa el escáner PET para obtener una imagen de esta distribución mediante la medición y localización de los dos rayos gamma que se originan a partir de la aniquilación del positrón emitido por cada radioisótopo.

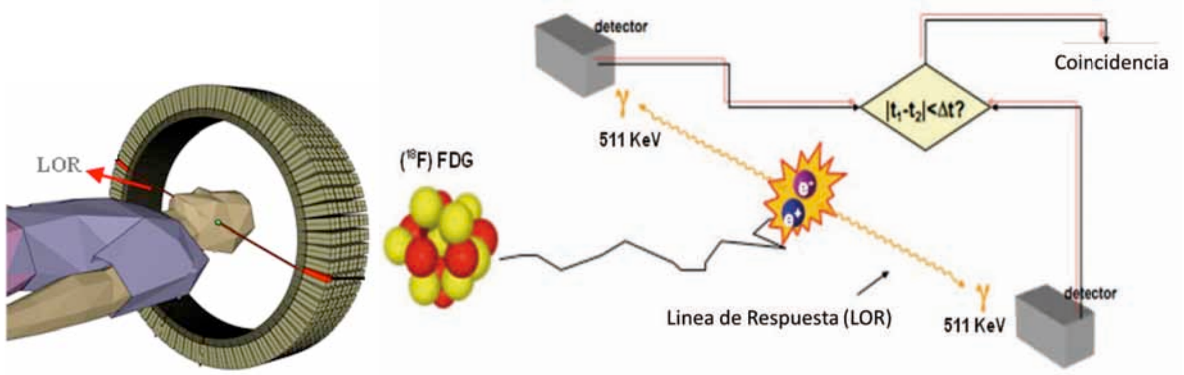

Figura R.1. Esquema básico de la técnica PET, en el que un paciente, tras haberle sido suministrado un radiotrazador, se coloca en el escáner para obtener una imagen de la biodistribucion del trazador a partir de la radiación medida. Los positrones emitidos terminan generado un par de rayos gamma antiparalelos. La detección de dos rayos gamma en detectores opuestos en un corto periodo de tiempo (coincidencia), permite estimar que en algún punto de la línea que une ambos detectores (LOR) existe un radiotrazador que se ha desintegrado. A partir del conjunto de todas las medidas recogidas por el escáner se obtiene la imagen final mediante un proceso conocido como reconstrucción de imagen.

Aunque la técnica PET se utilizó originalmente como una herramienta de investigación para el estudio de la biodistribución de diferentes radiotrazadores, en los últimos años, se ha convertido en una técnica cada vez más importante en la práctica clínica, especialmente en oncología. La mayoría de los estudios clínicos actuales usan ^{18}FDG como radiotrazador, ya que permite estudiar el metabolismo de la glucosa, que es significativamente alto en la mayoría de los tumores. La combinación de las imágenes de PET con la información anatómica proporcionada por un escáner CT, en máquinas de doble modalidad (PET/CT) ha sido un paso muy importante hacia su uso más habitual en clínica. Asimismo, la reciente introducción de una nueva generación de escáneres PET/CT con centelladores rápidos y con alta sensibilidad para detectar fotones de 511 keV, ha sido otra importante mejora en la técnica. Estos escáneres pueden utilizar la diferencia entre los tiempos de llegada de la pareja de fotones procedentes de la aniquilación de positrones (Información de Tiempo de Vuelo –TOF-) para mejorar la calidad de las imágenes reconstruidas. La técnica PET-TOF puede en principio mejorar significativamente la relación señal ruido de las imágenes y por lo tanto, la mejora en la detección de lesiones.

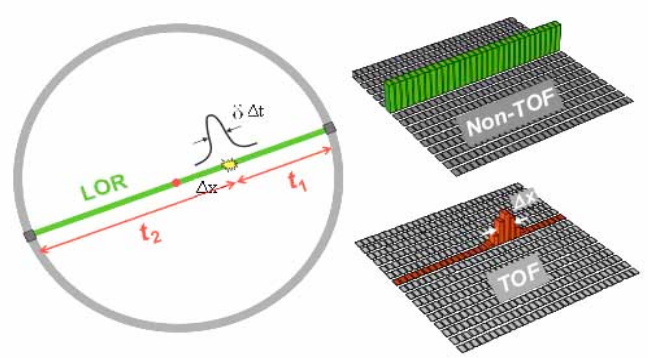

Figura R.2 Uso de la información de tiempo de vuelo para mejorar la localización a lo largo del LOR del lugar donde se ha producido la desintegración. La medida de las diferencias de los tiempos de llegada t_1 y t_2 a los detectores con suficiente precisión, permite saber si la desintegración se ha producido más o menos cerca de cada detector.

No obstante, existen todavía algunos factores que limitan un uso más amplio de la técnica PET. Por un lado, para realizer un estudio PET se necesitan isótopos no estables que se desintegren emitiendo un positrón, y por lo tanto, para los isótopos como el ^{18}F, esto requiere un ciclotrón que pueda producir estos isótopos. Este problema está siendo solucionado mediante la construcción de más ciclotrones que pueden aportar los isótopos necesarios para la mayoría de los grandes hospitales. Otro problema de PET es su relativa baja resolución (aproximadamente 5 mm), en comparación con otras técnicas de imagen como la tomografía computarizada o la resonancia magnética. Se están diseñando nuevos escáneres con el fin de mejorar la resolución. Y finalmente, hay una necesidad de reducir la cantidad de radiación que se inyecta en los pacientes para realizar un escáner PET, con el fin de minimizar los posibles efectos secundarios de la radiación. Esto se resuelve mediante el uso de nuevos diseños de escáneres con una mayor sensibilidad y una mejor localización de los eventos detectados (con la técnica del TOF), que permiten obtener imágenes de calidad pero con dosis más bajas para el paciente. Esta tesis se centra en el estudio de algunos de estos nuevos diseños con simulaciones y la evaluación de la mejora obtenida mediante los escáneres TOF-PET/CT en diferentes situaciones.

Los métodos de simulación Monte Carlo (MC) permiten estudiar las propiedades de un escáner que no puedan ser obtenidas experimentalmente, desarrollar y evaluar distintas correcciones y métodos de reconstrucción, así como también conocer el impacto en el rendimiento de los escáneres PET de determinadas modificaciones en su diseño y configuración, sin tener que construir múltiples prototipos. PeneloPET es un código MC basado en PENELOPE, para simulaciones PET que permite tener en cuenta la geometría del detector, la electrónica de adquisición y materiales y definiciones de las fuentes radiactivas. Esta herramienta se utiliza para la simulación de transporte de electrones, positrones y fotones con energías de hasta 1 GeV. PeneloPET es un código adaptado especialmente para simulaciones PET e incluye componentes básicos de la geometría del detector, la electrónica de adquisición y material y definiciones de las fuentes radiactivas.

Esta tesis se basa en simulaciones de PeneloPET de varias adquisiciones correspondientes a escáneres TOF-PET/CT de última generación. Uno de los principales objetivos de esta tesis es validar PeneloPET, que ya ha sido validado con escáneres preclínicos, para escáneres PET clínicos. Por lo tanto, simularon los escáneres PET/CT TruePoint Biograph (B-TP), Biograph TruePoint con TrueV (B-TPTV) y Biograph mCT. Estos escáneres tienen una configuración de tres (B-TP) y cuatro (B-TPTV y MCT) anillos de 48 bloques detectores. Cada bloque consta una matriz de 13 × 13 cristales de 4 × 4 × 20 mm3 de oxyorthosilicato de lutecio (LSO). Las simulaciones se ajustaron para reproducir algunos resultados experimentales de estos escáneres para posteriormente comparar resultados simulados con otra serie de con datos experimentales adicionales. Entre los parámetros estimados, se encuentra la fracción de sensibilidad, la resolución espacial, la tasa de cuentas efectiva (NEC) y la fracción de dispersión (SF). Las simulaciones se emplearon también para evaluar los valores óptimos de algunos parámetros del sistema, tales como la ventana de energía y de tiempo de coincidencia y para evaluar el efecto de algunas modificaciones del sistema (como el número de anillos) en el rendimiento. Además se comprobó la capacidad del código PeneloPET para incorporar la información de TOF en la simulación.

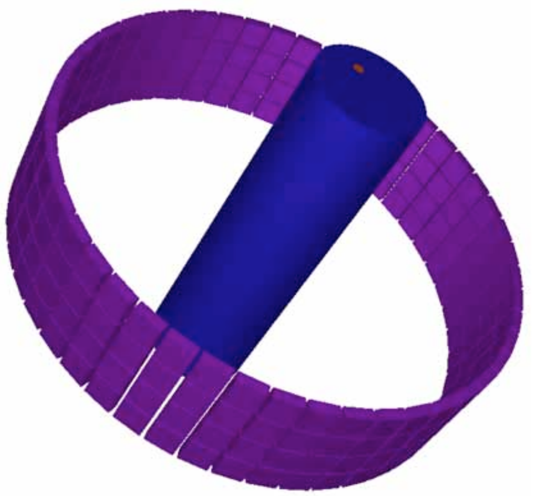

Figura R.3. Geometría del escáner Biograph-TPTV simulado con PeneloPET, donde se observan los cuatro anillos detectores y en el centro, el maniquí NEMA usado como estándar para caracterizar escáneres clínicos.

La razón de elegir los escáneres Biograph de Siemens viene fundamentada porque han sido uno de los primeros en tener capacidad de tiempo de vuelo y porque el rendimiento, de las múltiples versiones del Biograph que han ido apareciendo en el mercado ha sido medido y publicado con detalle y precisión. Se ha tenido además la suerte de contar con la colaboración de Bjoern Jakoby, científico encargado en Siemens de las pruebas de rendimiento del Biograph.

En esta tesis también se ha estudiado el impacto del uso de la información de TOF en las imágenes reconstruidas. Las imágenes PET muestran un mapa del radiotrazador que emite los fotones dentro del paciente. Esta imagen se obtiene a partir de los pares de rayos gamma detectados, a través de un proceso de reconstrucción de imagen que implementa un modelo de la emisión y la detección de la radiación. Este modelo puede ser muy simple, como el usado en los métodos de reconstrucción analíticos, o mucho más realista como el empleado en los métodos iterativos. En esta tesis hemos utilizado nuestro código de reconstrucción 3D iterativo GFIRST que implementa el algoritmo 3D-OSEM. Las imágenes se han reconstruido con y sin usar la información de tiempo de vuelo, con el fin de investigar la ganancia en calidad de imagen que se puede llegar a obtener en diferentes casos con distintos niveles de ruido. Para ello se ha estudiado la relación señal-ruido, el contraste y el ruido en las imágenes correspondientes a un maniquí NEMA empleado habitualmente para la caracterización de estas máquinas.

En general esta tesis busca obtener un mejor conocimiento de las características de los escáneres clínicos PET de última generación, mediante herramientas de simulación y de reconstrucción de imagen que permitan investigar y encontrar posibles mejoras en sus diseños.

Podemos singularizar el objetivo principal de la tesis como el de lograr la traslación del conocimiento y experiencia adquiridos por el Grupo de Física Nuclear (GFN) durante casi 8 años de investigación en imagen PET preclínica, al campo de la imagen clínica. Los dos objetivos principales conducentes al objetivo principal son:

1) Validar la herramienta de simulación del GFN, PeneloPET en el entorno preclínico, simulando y comparando con los resultados de la familia de escáneres PET/CT Biograph de Siemens, en particular con la incorporación de la información de Tiempo de Vuelo (TOF).
2) Extender las herramientas de reconstrucción de imagen PET desarrolladas en el grupo, en particular GFIRST, al campo clínico y evaluar la contribución de la información TOF a la calidad de la imagen reconstruida.

Simulaciones Monte Carlo de Escáneres PET clínicos

En este capítulo se evaluó la capacidad del código de simulación Monte Carlo PeneloPET de simular escáneres PET/CT clínicos. Para este propósito, se simularon distintas medidas de rendimiento de las máquinas B-TP, B-TPTV y mCT PET/CT (Siemens Medical Solutions EE.UU., Inc.) y los resultados se compararon con los datos experimentales presentes en la literatura.

Uno de los principales problemas a la hora de reproducir mediante simulaciones el comportamiento de un escáner comercial, consiste en que existen una serie de parámetros internos de la máquina que no se encuentran disponibles en las publicaciones. En esta tesis, se ha demostrado que PeneloPET es lo suficientemente flexible como para adaptarse fácilmente a diferentes ingredientes de como el tiempo muerto de la electrónica, que han sido ajustados para que las curvas experimentales de la tasa de cuentas efectivas (NEC) para uno de los escáneres (el B-TPTV) pudieran ser reproducidas.

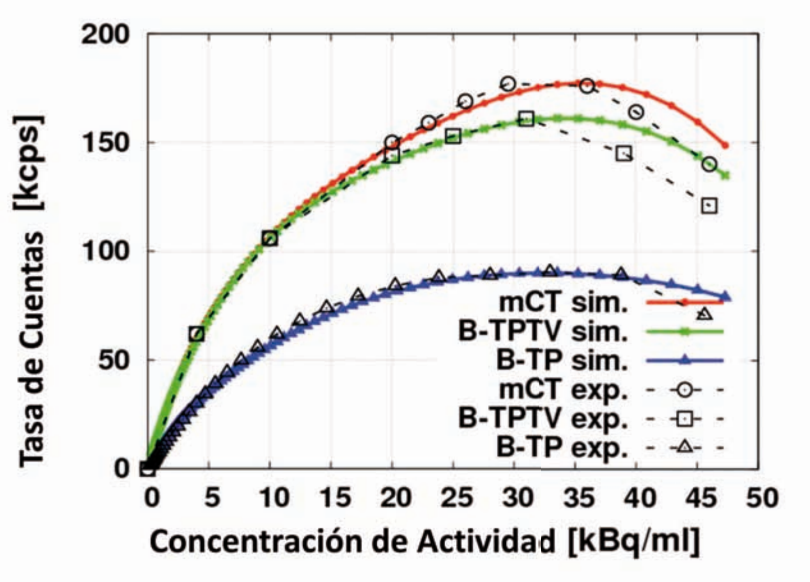

Figura R.4 Comparativa de la tasa de cuentas efectivas NEC en función de la concentración de actividad, con los datos simulados y los datos experimentales. Las curvas se han obtenido con el tiempo de coincidencia y la ventana de energía de (Jakoby et al., 2009, 2011).

Una vez que la simulación se ha ajustado para reproducir la sensibilidad del escáner B-TPTV, las predicciones para la fracción de dispersión (Tabla R.1) y la tasa de cuentas efectivas NEC obtenidas de la simulación (Tabla R.1 y Figura R.4), están de acuerdo dentro del 5 % con los valores medidos para los tres escáneres bajo investigación. Asimismo, los resultados simulados y experimentales de la resolución espacial también son similares (Tabla R.2), estando las diferencias dentro de la incertidumbre experimental.

Table R.1. Resumen del valor máximo de la tasa de cuentas efectivas NEC (Noise equivalent counts), y la Fracción de Dispersión (SF) para varias configuraciones de escáneres. Todos los resultados se obtuvieron con las ventanas de coincidencia temporal y de energía igual a la usada en los experimentos (Jakoby et al., 2011, 2009).

Número de anillos	*Maximo de la curva NEC (Kcps) @(kBq/ml)*			*Fracción de Dispersión (%)*		
	Simulado (esta tesis)	*Simulado (Eriksson et al., 2007)*	*Experimental*	*Simulado (esta tesis)*	*Simulado (Eriksson et al., 2007)*	*Experimental*
B-TP	*90 @ 33*	*100@34*	*93@34*	*34.3*	*33*	*32.0*
B-TPTV	*161@32.5*	*177@34*	*161@31.5*	*31.3*	*35*	*32.5*
mCT	*177@34*	*-*	*180.3@29*	*34.8*	*-*	*33.5*
5-rings	*259@39*	*-*	*-*	*30.8*	*-*	*-*
8-rings	*489@35*	*-*	*-*	*32.0*	*-*	*-*
10-rings	*787@30*	*800@31*	*-*	*33.1*	*35*	*-*

Tabla R.2. Resolución espacial simulada y experimental del escaner B-TPTV. Los resultados experimentales tienen una incertidumbre de ± 0.3 mm (Jakoby et al., 2009)

	FWHM (mm)		*FWTM (mm)*	
	Simulado	*Experimental*	*Simulado*	*Experimental*
		1 cm del centro		
Transversal	*4.6*	*4.2*	*8.5*	*8.1*
Axial	*4.2*	*4.5*	*8.4*	*9.2*
Resolución Media	*4.4*	*4.4*		
		10 cm del centro		
Transversal(radial)	*5.5*	*4.6*	*9.0*	*9.4*
Transversal (tangen.)	*5.6*	*5.0*	*10.2*	*9.4*
Axial	*4.4*	*5.5*	*7.5*	*10.5*
Resolución Media	*5.3*	*5.0*		

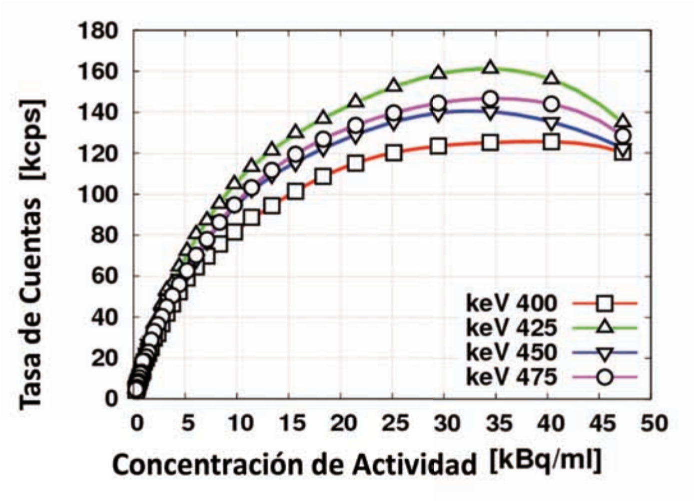

Figura R.5 Tasa de cuentas efectivas NEC en función de la concentración de actividad, para distintos valores de la ventana inferior de energía usada para elegir los eventos verdaderos.

Estos resultados validan el uso de PeneloPET para simular los escáneres clínicos. Con una herramienta de simulación validada, podemos realizar simulaciones para investigar el efecto de la variación de varios parámetros del escáner básicos en el rendimiento del sistema B-TPTV. Por ejemplo, se midió el impacto de la ventana de energía en la los valores del máximo de la curva NEC. Las simulaciones permiten la determinación de los valores óptimos de este tipo de parámetros. Para el B-TPTV, las simulaciones confirmaron que los valores predeterminados de fábrica, una ventana de energía 425 a 650 keV son las mejores opciones (Figura R.5).

La sensibilidad del sistema PET se puede aumentar mediante la colocación de más anillos de detectores, y también mediante el aumento de la máxima diferencia entre anillos para los pares de eventos de coincidencias aceptados. La buena concordancia de las simulaciones con las medidas en los escáneres existentes, permiten hacer predicciones fiables para escáneres con un mayor número de anillos o mayor diferencia de anillo. La diferencia entre anillos aumentada del escáner PET mCT conduce a un aumento del 19% en la sensibilidad, en comparación con el escáner con diferencia entre anillos normal, el B-TPTV. Esta mayor diferencia entre anillos en las cuentas que se aceptan en el mCT también conduce a un aumento del 10% del pico de la NEC pico, en comparación con el B-TPTV (tabla R.2). Estos resultados están de acuerdo con la simulación previa hecha con GATE (Eriksson et al., 2007) o con SimSET (MacDonald et al., 2008).

Reconstrucción de Imagen PET con información de Tiempo de Vuelo

En este capítulo se muestran los pasos realizados para la reconstrucción de imágenes a partir de sinogramas obtenidos de las simulaciones de los escáneres clínicos. Por un lado se creó un código en de reconstrucción analítica de imagen, usado normalmente en las comparaciones de rendimiento de escáneres, y por el otro se adaptó el código de reconstrucción iterativa GFIRST a escáneres clínicos. También se describen las correcciones de normalización, rellenado de huecos (gaps) y atenuación, fundamentales para obtener imágenes de calidad (ver figuras R.6 y R.7)

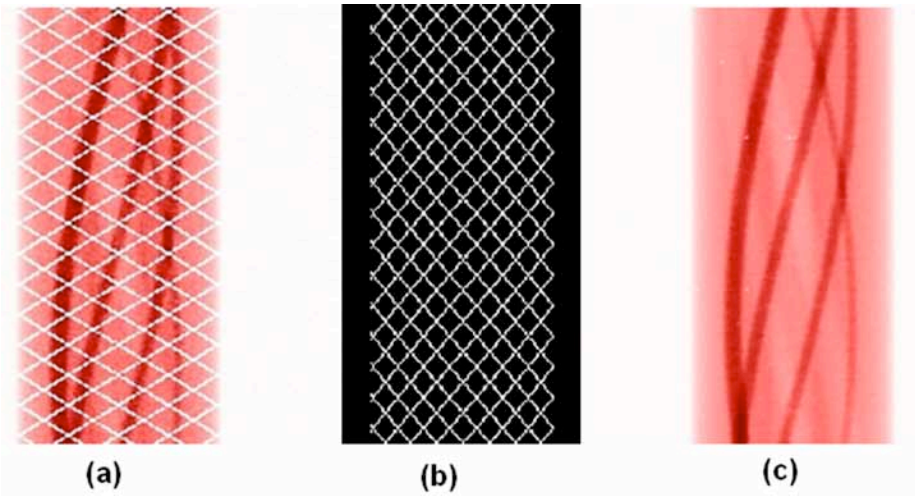

Figura R.6. Ejemplo de sinograma con huecos en a) para los escáneres Biograph, máscara usada para corregirlos en b), y sinograma corregido en c).

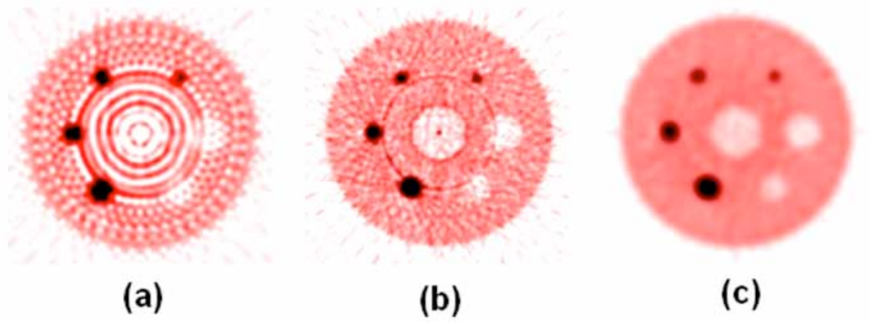

Figure R.7. Reconstrucción analítica FBP del maniquí de calidad de imagen: sin normalización (a), con normalización (b) y con normalización y rellenado de huecos (c).

Una vez establecida la herramienta para la reconstrucción en escáneres clínicos y las correcciones necesarias, se puede proceder a evaluar el impacto del uso de la información del TOF en la calidad de las imágenes reconstruidas. Tal como se puede observar en las imágenes de la figura R.8 y R.9, el usar TOF permite una convergencia más rápida y una mejor calidad de imagen.

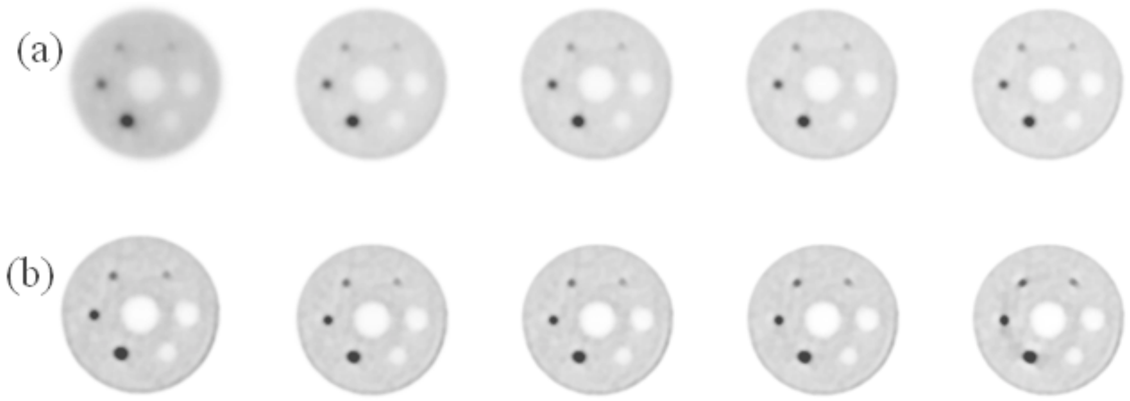

Figura R.8. Imágenes reconstruidas del maniquí de calidad de imagen de NEMA con una relación de actividad de 8 a 1 en las regiones calientes (esferas) respecto al fondo. Sin usar la información de TOF (a) y usando TOF (b). Los resultados, de izquierda a derecha corresponden a las imágenes de 1 a 5 iteraciones.

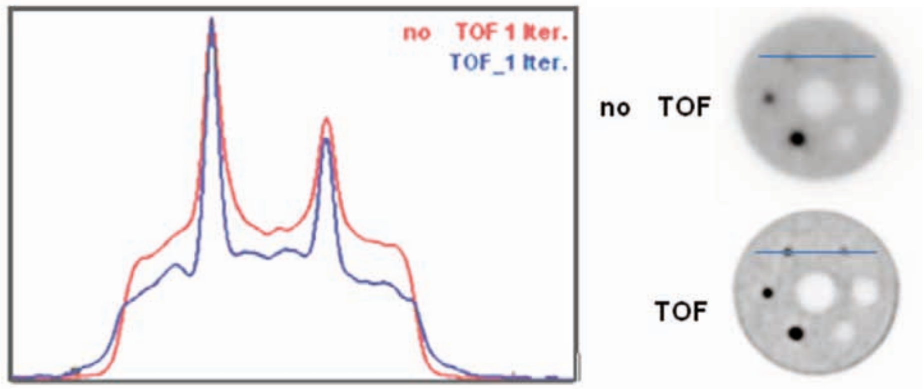

Figura R.9: Perfil de las imágenes reconstruidas con y sin información de TOF a lo largo de las esferas de 10 y 13 mm tras 1 iteración.

Para realizar un análisis cuantitativo de las imágenes reconstruidas con y sin usar la información de tiempo de vuelo, se usaron diversas métricas que analizan características de la imagen como el nivel de ruido de las zonas uniformes, el contraste (medido como la relación entre las regiones de mayor actividad frente al fondo) y la relación señal-ruido que da una idea de la posibilidad de detectar una lesión en una imagen PET de este tipo.

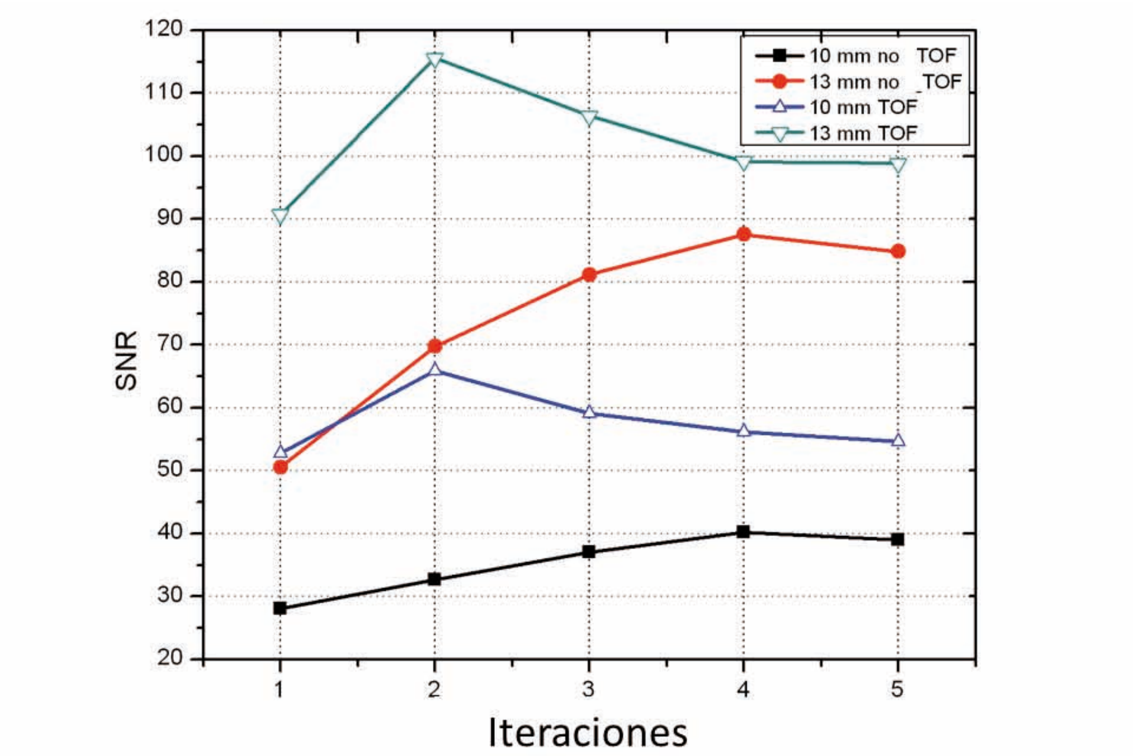

Figura R.10 Relación señal-ruido frente al número de iteraciones para las esferas de 10 y 13 mm con y sin usar TOF. Cada punto corresponde a una iteración con 10 subsets.

Finalmente, se estudió la variación del impacto del uso de la información de TOF en la reconstrucción en función del número de cuentas adquiridas. Uno de los principales resultados obtenidos en esta sección es que se ha determinado que a mayor número de cuentas en la imagen, la mejora en el contraste y el ruido que se obtiene con TOF es mayor, tal como se puede ver en la Tabla 4.3.

Tabla R.3 Contraste y ruido de fondo para las esferas de 10 mm en las imágenes del maniquí de calidad, reconstruidas sin TOF y con la información TOF, para 3 estudios diferentes con 12, 112 y 970 millones de cuentas. Para cada caso, los valores mostrados corresponden al número óptimo de iteraciones de acuerdo a la relación señal-ruido (SNR) tanto con TOF como sin TOF.

	Contraste			**Ruido %**		
Cuentas (Mcts)	**970**	**112**	**12**	**970**	**112**	**12**
Sin-TOF	**2.9**	**2.7**	**2.6**	**4.5**	**5.4**	**11.7**
TOF	**3.1**	**2.8**	**2.8**	**3.6**	**5.0**	**10.7**

Resumen y Conclusiones

En esta tesis se ha mostrado que el código de simulación Monte Carlo PeneloPET, desarrollado en el Grupo de Física Nuclear de la Universidad Complutense de Madrid, es lo suficientemente flexible como para incorporar las principales características de distintos escáneres PET, incluyendo escáneres clínicos, logrando reproducir las medidas experimentales obtenidas con estas máquinas.

Una de los principales problemas de simular escáneres comerciales consiste en el hecho de que generalmente algunas de sus características (como la electrónica y el proceso de formación de coincidencias) no son conocidas. En ese caso es necesario ajustar una serie de parámetros de manera que se reproduzcan los datos experimentales publicados. En esta tesis se ha mostrado que una vez realizado ese ajuste, se pueden reproducir otra serie de datos experimentales adicionales, así como otros escáneres de la misma familia (que comparten muchas características comunes).

En concreto, una vez que la simulación se ha afinado para reproducir la sensibilidad del escáner B-TPTV, las predicciones para la fracción de dispersión están de acuerdo dentro de un 5% con los valores medidos para los tres escáneres bajo investigación. Asimismo, la sensibilidad, la resolución y la tasa de cuentas efectivas NEC de los escáneres B-TP, B-TPTV y mCT se lograron reproducir dentro de las incertidumbres experimentales.

Una vez que se tienen todos los parámetros del escáner, se ha podido estudiar cómo afecta el variar alguno de estos parámetros en las principales características de su rendimiento (como la sensibilidad o la tasa de cuentas efectiva NEC). Tal como era de esperar, muchos de los parámetros óptimos estimados (como la ventana de energía usada para elegir las coincidencias) coinciden con los empleados en los escáneres comerciales. En otros casos, se ha podido estimar lo que se puede llegar a ganar en sensibilidad con escáneres con un mayor número de detectores.

En estas simulaciones, se ha incorporado al información de TOF en los ficheros de salida, de manera similar a como se hace en los escáneres clínicos, demostrando que PeneloPET es capaz de incorporar fácilmente esta información.

En esta tesis se ha demostrado también la mejora en la imagen que se obtiene mediante el uso de la información TOF obtenida en los escáneres PET. Se encontró que la información TOF, en las reconstrucciones realizadas con el código GFIRST permite obtener un mejor contraste de imagen y menor ruido, y también mayor SNR que sin TOF. Se ha demostrado cuantitativamente que la ganancia SNR debido a TOF tiene el mayor efecto en las adquisiciones con un gran número de eventos.

Como conclusión, esta tesis muestra que PeneloPET es una potente herramienta para la simulación y diseño de escáneres PET clínicos. Además, el código de la reconstrucción, GFIRST ha mostrado suficiente flexibilidad como para incorporar información TOF y estudiar su impacto en la calidad de imagen. La combinación de estos instrumentos presentados en esta memoria se pueden utilizar para generar nuevos escáneres clínicos que puedan proporcionar imágenes con mejor resolución, mejor detectabilidad de lesiones y que requieran dosis más baja de radiación para los pacientes.